

Georg Lindefjeld Berg

## **Drone based calibration of MAMIMO**

Anechoic Chamber to Field: Challenges and Solutions  
for MAMIMO Calibration

Master's thesis in Electronic Systems Design  
Supervisor: Torbjörn Ekman  
June 2025

Norwegian University of Science and Technology  
Faculty of Information Technology and Electrical Engineering  
Department of Electronic Systems





# ABSTRACT

## summary

Massive Multiple Input Multiple Output (MAMIMO) systems are critical for modern wireless communication due to their enhanced data rates and reliability. However, their performance depends on precise calibration, which is traditionally conducted in controlled environments like anechoic chambers. This approach becomes impractical once systems are deployed in real-world settings, where environmental factors and hardware drifts degrade calibration accuracy.

This thesis investigates a flexible, in-situ calibration method for MAMIMO antenna arrays, using a Software Defined Radio (SDR)-based system with GNSS positioning. The experimental setup employs a custom-built  $3 \times 1$  LPDA receiver array. Although the original goal was to develop a drone-mounted calibration payload, time and hardware constraints limited the implementation to a portable, man-carried transmitter platform.

The calibration process leverages Universal Software Radio Peripherals (US-RPs) for signal transmission and reception, synchronized via Global Navigation Satellite System (GNSS) timestamps and preamble-based algorithms. Channel estimation methods, including Least Squares (LS) and analysis of Channel Impulse Response (CIR), were implemented to isolate Line-of-Sight (LoS) components and compute relative differences. Experiments were conducted in both an anechoic chamber and outdoor environments. Results demonstrated consistent and reproducible phase offsets between channels in the controlled environment, with deviations at higher frequencies (6 GHz) explained by path-length differences and positional uncertainties. Outdoor measurements highlighted the challenges of GNSS accuracy and multipath, but showed that calibration is feasible with better position corrections and careful site selection.

This work confirms the feasibility of portable, in-situ calibration for MAMIMO systems using SDR, offering a flexible and cost-effective solution for maintaining performance in operational environments. Future work should focus on developing a lightweight drone payload and further improving precision and automated positional compensation.

## Sammendrag

Massive Multiple Input Multiple Output (MAMIMO)-systemer er avgjørende for moderne trådløs kommunikasjon på grunn av økt datakapasitet og pålitelighet. Imidlertid avhenger ytelsen deres av presis kalibrering, som tradisjonelt utføres i kontrollerte miljøer som ekkofrie kamre. Denne tilnærmingen blir upraktisk etter utrulling i virkelige omgivelser, hvor miljøfaktorer og hardwareavvik reduserer kalibreringsnøyaktigheten.

Denne masteroppgaven undersøker en fleksibel, *in-situ* kalibreringsmetode for MAMIMO-antennearrayer, basert på et SDR-system med GNSS-posisjonering. Eksperimentene benytter et spesialbygd  $3 \times 1$  LPDA mottakerarray. Selv om målet var å utvikle en dronebasert kalibreringsplattform, ble dette ikke realisert på grunn av tids- og hardwarebegrensninger. I stedet ble en bærbar, manuelt flyttet senderplattform benyttet.

Kalibreringsprosessen benytter Universal Software Radio Peripherals (USRP) for sending og mottak, synkronisert via GNSS-tidsstempler og preamblebaserte algoritmer. Kanalestimeringsmetoder, inkludert Least Squares (LS) og analyse av Channel Impulse Response (CIR), ble implementert for å isolere direkte signalbaner (LoS) og beregne relative avvik. Eksperimenter ble utført både i ekkofritt kammer og utendørs. Resultatene viste konsistente og reproducerbare faseforskjeller mellom kanaler i kontrollerte omgivelser, med avvik ved høyere frekvenser (6 GHz) forklart av banelengdeforskjeller og posisjonsusikkerhet. Utendørsmålingene fremhevet utfordringer knyttet til GNSS-nøyaktighet og multibane, men viste at kalibrering er mulig med RTK-korreksjoner og nøyne valg av måleområde.

Arbeidet bekrefter at fleksibel, portabel *in-situ* kalibrering av MAMIMO-systemer med SDR og GNSS er gjennomførbart, og gir en kostnadseffektiv løsning for å opprettholde ytelse i operative miljøer. Fremtidig arbeid bør fokusere på utvikling av en lett droneplattform og videre forbedring av presisjon ved høye frekvenser og automatisert posisjonskompensasjon.

## PREFACE

This thesis concludes my master's studies in Electronic Systems Design at the Norwegian University of Science and Technology (NTNU). The work was conducted during the spring semester of 2025 under the supervision of Professor Torbjörn Ekman at the Department of Electronic Systems (IES). It builds upon my specialization project from 2024, which laid the theoretical groundwork for drone-based calibration of antenna arrays [1].

The motivation for this research stems from the growing need for reliable wireless communication in autonomous systems, particularly within maritime applications like the SFI AutoShip project. Calibrating Massive MIMO systems in their operational environments poses significant challenges, and this thesis explores an innovative solution to address them. The journey has been both intellectually demanding and rewarding, combining theoretical analysis, software development, and practical experimentation. From debugging Matlab to manually rotating antennas in NTNU's anechoic chamber, every challenge deepened my understanding of wireless systems design.

I would like to express my sincere gratitude to my supervisor, Professor Torbjörn Ekman, for his steadfast support, insightful guidance, and constructive feedback throughout this project. His expertise in radio systems and pragmatic approach to problem-solving have been invaluable to both the direction and quality of this work. I am also grateful to the technical staff at the IES mechanical workshop for their precision and dedication in fabricating the antenna array prototype, and to Senior Engineer Terje Mathisen for his assistance in acquiring the necessary hardware and tools.

I would also like to thank the team at the UAV Lab, especially Torleiv Håland Bryne, for their valuable assistance with GNSS-related aspects of this project. Finally, I am grateful to my family and friends for their encouragement and support during late-night coding sessions and countless revisions.

This work would not have been possible without the resources and collaborative spirit of NTNU. I hope it contributes to the field of wireless communication and inspires innovation in *in-situ* calibration methods.

Georg Lindefield Berg,  
Trondheim, June 2025

# CONTENTS

<b>Abstract</b>	<b>i</b>
<b>Preface</b>	<b>iii</b>
<b>Contents</b>	<b>vi</b>
<b>List of Figures</b>	<b>vi</b>
<b>List of Tables</b>	<b>viii</b>
<b>Abbreviations</b>	<b>x</b>
<b>1 Introduction</b>	<b>1</b>
1.1 Introduction . . . . .	1
1.2 Motivation . . . . .	1
1.3 Project Description . . . . .	1
1.3.1 Stakeholders . . . . .	2
1.3.2 Sustainability Relevance . . . . .	3
<b>2 Theory</b>	<b>5</b>
2.1 Introduction . . . . .	5
2.2 The Concept of Calibration . . . . .	5
2.3 The Antenna . . . . .	7
2.3.1 MIMO . . . . .	8
2.3.2 LPDA antenna . . . . .	8
2.4 The Channel . . . . .	11
2.4.1 Channel Estimation . . . . .	15
2.4.2 The forward-and-backward APES . . . . .	16
2.4.3 Finding the constant offset . . . . .	16
2.4.4 Fading . . . . .	18
2.5 UAV . . . . .	20
2.6 Anechoic Chamber . . . . .	20
2.7 GNSS Positioning . . . . .	21
2.7.1 Real-Time Kinematic (RTK) GNSS . . . . .	21
2.8 Software-Defined Radio . . . . .	22
2.8.1 Carrier Frequency Offset . . . . .	22
2.9 Packet-Based Communication . . . . .	23

2.9.1	Zadoff-Chu Sequence . . . . .	23
2.9.2	QPSK Modulation . . . . .	24
2.10	Calibration Trade-offs and Practical Considerations . . . . .	24
2.10.1	Bandwidth . . . . .	24
2.10.2	Resolution . . . . .	25
2.10.3	Distance . . . . .	26
2.10.4	Measurement Environments . . . . .	26
2.10.5	Positioning . . . . .	28
2.11	Summary . . . . .	28
<b>3</b>	<b>Methods</b>	<b>29</b>
3.1	Introduction . . . . .	29
3.2	System Overview . . . . .	29
3.2.1	Hardware Overview . . . . .	29
3.2.2	Software Overview . . . . .	30
3.3	Signal Processing Pipeline . . . . .	31
3.3.1	Transmitted Signal Design . . . . .	32
3.3.2	Receiver Processing . . . . .	32
3.4	Measurement Setups . . . . .	33
3.4.1	Anechoic Chamber Setup . . . . .	34
3.4.2	Outdoor Measurement Setup . . . . .	36
3.5	Calibration and Data Analysis . . . . .	37
3.5.1	Calibration Procedure . . . . .	37
3.5.2	Data Post-Processing . . . . .	39
3.6	Summary of Parameters . . . . .	39
3.7	Summary . . . . .	42
<b>4</b>	<b>Results</b>	<b>43</b>
4.1	Introduction . . . . .	43
4.2	Anechoic Chamber Results . . . . .	43
4.2.1	Anechoic Chamber Measurements at 1.3 GHz . . . . .	43
4.2.2	Anechoic Chamber Measurements at 3 GHz . . . . .	45
4.2.3	Anechoic Chamber Measurements at 6 GHz . . . . .	46
4.2.4	Summary of Anechoic Chamber Results . . . . .	48
4.3	Outdoor Results . . . . .	48
4.3.1	Calibration Results at 1.3 GHz . . . . .	48
4.3.2	GNSS Data and RTK Correction Results . . . . .	49
4.3.3	Summary of Outdoor Results . . . . .	53
4.4	Comparison and Key Findings . . . . .	53
4.5	Additional Results . . . . .	53
4.6	Summary . . . . .	53
<b>5</b>	<b>Discussion</b>	<b>55</b>
5.1	Introduction . . . . .	55
5.2	Interpretation of Key Results . . . . .	55
5.2.1	Anechoic Chamber Results . . . . .	56
5.2.2	Outdoor Results . . . . .	57
5.3	Comparison with Theory and Previous Work . . . . .	58
5.4	Analysis by Scenario . . . . .	59

5.5	Limitations and Sources of Error . . . . .	59
5.6	Recommendations and Future Work . . . . .	60
5.6.1	1. Positioning Accuracy and Validation . . . . .	60
5.6.2	2. Drone Payload and System Miniaturization . . . . .	61
5.6.3	3. Real-Time Processing, Speed and Automation . . . . .	61
5.6.4	4. Antenna Characterization . . . . .	61
5.6.5	5. Advanced Data Processing and Validation . . . . .	62
5.7	Summary . . . . .	62
<b>6</b>	<b>Conclusions</b>	<b>63</b>
	<b>References</b>	<b>65</b>
<b>7</b>	<b>Appendices</b>	<b>67</b>
	<b>Appendices:</b>	<b>67</b>
A	GitHub repository . . . . .	67
B	Extra results . . . . .	67
B1	Anechoic chamber extra results . . . . .	67
B2	Outdoor extra results . . . . .	71
C	SDR configuration . . . . .	72
C1	Indoor SDR configuration . . . . .	72
C2	Outdoor SDR configuration . . . . .	73
D	GNSS configuration . . . . .	73
D1	Rx Positioning . . . . .	73
D2	Tx Positioning . . . . .	73
D3	RTK correction . . . . .	74
E	Turttable configuration . . . . .	75
F	SDR System Design . . . . .	75
F1	SDR Tx . . . . .	75
F2	SDR Rx . . . . .	76
G	Rx Array Design . . . . .	81

## LIST OF FIGURES

1.3.1 Calibration Setup Illustration . . . . .	4
2.2.1 Linear Time-Invariant (LTI) system . . . . .	6
2.2.2 FIR filter representation of the channel . . . . .	6
2.3.1 NTNU MAMIMO Testbed System . . . . .	8
2.3.2 One LPDA element . . . . .	9
2.3.3 Simulated LPDA pattern E-plane, 1.45 GHz . . . . .	9
2.3.4 Simulated LPDA pattern E-plane, 2.6 GHz . . . . .	9
2.3.5 Simulated LPDA pattern E-plane, 3.8 GHz . . . . .	9
2.3.6 Simulated LPDA pattern E-plane, 5.9 GHz . . . . .	9
2.3.7 Simulated LPDA pattern H-plane, 1.45 GHz . . . . .	10
2.3.8 Simulated LPDA pattern H-plane, 2.6 GHz . . . . .	10
2.3.9 Simulated LPDA pattern H-plane, 3.8 GHz . . . . .	10
2.3.10 Simulated LPDA pattern H-plane, 5.9 GHz . . . . .	10
2.3.11 LPDA phase center vs. frequency . . . . .	11
2.4.1 Illustration of multipath propagation . . . . .	12
2.4.2 Example of a CIR . . . . .	13
2.4.3 Multipath fading geometry . . . . .	19
2.4.4 Attenuation difference between LoS and multipath . . . . .	19
2.4.5 Elevation-based fading mitigation . . . . .	20
2.7.1 Phase error from GNSS position uncertainty . . . . .	21
2.10.1 Direction of Arrival Variation Across Array . . . . .	27
3.3.1 Signal Processing Pipeline . . . . .	31
3.3.2 The packet . . . . .	32
3.4.1 The anechoic chamber system drawing . . . . .	34
3.4.2 Anechoic chamber antenna array . . . . .	35
3.4.3 Anechoic chamber measurement setup . . . . .	35
3.4.4 Outdoor system setup . . . . .	36
3.4.5 Movement of the outdoor system measurement . . . . .	37
3.5.1 Compas to view orientation . . . . .	40
4.2.1 LoS tap phase and amplitude (1.3 GHz) . . . . .	44
4.2.2 Offset LoS tap phase and amplitude (1.3 GHz) . . . . .	44
4.2.3 LoS tap phase and amplitude (3 GHz) . . . . .	45
4.2.4 Offset LoS tap phase and amplitude (3 GHz) . . . . .	46
4.2.5 LoS tap phase and amplitude (6 GHz) . . . . .	47

4.2.6 Offset LoS tap phase and amplitude (6 GHz) . . . . .	47
4.3.1 LoS tap phase and amplitude outdoor (1.3 GHz) . . . . .	48
4.3.2 Offset LoS tap phase and amplitude outdoor (1.3 GHz) . . . . .	49
4.3.3 Raw GNSS data outdoor . . . . .	50
4.3.4 RTK GNSS data outdoor . . . . .	50
4.3.5 Good GNSS data . . . . .	51
4.3.6 Phase and amplitude offset with good GNSS data . . . . .	52
4.3.7 Number of satellites used for GNSS . . . . .	52
B.1 LoS tap phase and amplitude (1.3GHz) . . . . .	68
B.2 Offset LoS tap phase and amplitude (1.3GHz) . . . . .	68
B.3 LoS tap phase and amplitude (3GHz) . . . . .	69
B.4 Offset LoS tap phase and amplitude (3GHz) . . . . .	69
B.5 LoS tap phase and amplitude (6GHz) . . . . .	70
B.6 Offset LoS tap phase and amplitude (6GHz) . . . . .	70
B.7 LoS tap phase and amplitude (1.3GHz) outdoor . . . . .	71
B.8 Offset LoS tap phase and amplitude (1.3GHz) outdoor . . . . .	71
F.1 Frame Synchronization Cross-Correlation . . . . .	77

## LIST OF TABLES

2.3.1 LPDA element specifications . . . . .	9
2.8.1 USRP B210 specifications . . . . .	22
3.6.1 Anechoic Chamber System Parameters (Grouped by Subsystem) . .	41
3.6.2 Outdoor System Parameters (Grouped by Subsystem) . . . . .	41
C.1 SDR Transmitter (Tx) Configuration . . . . .	72
C.2 SDR Receiver (Rx) Configuration . . . . .	72
C.3 Outdoor SDR Rx configuration . . . . .	73

## ABBREVIATIONS

List of all abbreviations in alphabetic order:

- **APES** Amplitude and Phase Estimation
- **BPSK** Binary Phase Shift Keying
- **CFO** Carrier Frequency Offset
- **CFR** Channel Frequency Response
- **CIR** Channel Impulse Response
- **CP** Cyclic Prefix
- **DC** Direct Current
- **DoA** Direction of Arrival
- **DoD** Direction of Departure
- **FFT** Fast Fourier Transform
- **FPGA** Field Programmable Gate Array
- **FSPL** Free Space Path Loss
- **GNSS** Global Navigation Satellite System
- **GRC** GNU Radio Companion
- **IES** Department of Electronic Systems (NTNU)
- **IFFT** Inverse Fast Fourier Transform
- **IMU** Inertial Measurement Unit
- **in-situ** In the original place or position
- **LoS** Line of Sight
- **LOWESS** Locally Weighted Scatterplot Smoothing
- **LPDA** Log-Periodic Dipole Array

- **LS** Least Squares
- **LTE** 4G Long-Term Evolution
- **LTI** Linear Time Invariant
- **MAMIMO** Massive Multiple Input Multiple Output
- **MIMO** Multiple Input Multiple Output
- **MLE** Maximum Likelihood Estimation
- **MSELSYS** Electronic Systems Design Master's Programme, 2 years
- **NTNU** Norwegian University of Science and Technology
- **OFDM** Orthogonal Frequency Division Multiplexing
- **QPSK** Quadrature Phase Shift Keying
- **RPi** Raspberry Pi
- **RTK** Real Time Kinematic
- **Rx** Receiver
- **SDR** Software Defined Radio
- **SNR** Signal-to-Noise Ratio
- **TFE4590** Electronic Systems Design, Specialization Project
- **TFE4930** Electronic Systems Design, Master Theses
- **Tx** Transmitter
- **UAV** Unmanned Aerial Vehicle
- **USRP** Universal Software Radio Peripheral



---

CHAPTER  
**ONE**

---

## INTRODUCTION

### 1.1 Introduction

This chapter outlines the context, objectives, and significance of the thesis. It begins by establishing the motivation for drone-based calibration of a MAMIMO systems, followed by a description of the project scope and methodology. The chapter also discusses stakeholder relevance and concludes with an analysis of the sustainability implications aligned with the United Nations Sustainable Development Goals (SDGs).

### 1.2 Motivation

Massive Multiple Input Multiple Output systems are pivotal in advancing wireless communication, offering enhanced data rates, spectral efficiency, and reliability [2]. However, their performance hinges on precise calibration to account for phase and amplitude offsets between antenna elements. Traditional calibration methods, conducted in controlled environments like anechoic chambers, fail to address real-world operational challenges such as environmental degradation, hardware drifts, and multipath interference. These limitations become critical in applications like autonomous maritime systems (e.g., the SFI AutoShip project), where antennas are deployed in dynamic, harsh environments. Existing *in-situ* calibration approaches are often labor-intensive, costly, or impractical for large arrays. This thesis addresses these gaps by proposing a drone-assisted calibration method that enables rapid, cost-effective adjustments directly in the operational environment.

### 1.3 Project Description

The project focuses on developing and validating a flexible calibration framework for MIMO antenna arrays, with the long-term goal of enabling drone-based, *in-situ* calibration. The core concept is to use a Software Defined Radio (SDR)-equipped platform, ideally mounted on a UAV (drone), but in this work implemented as a portable, man-carried transmitter, to transmit known signals from a range of positions and angles relative to the receiver array. Illustrated in Figure 1.3.1, the transmitter is moved systematically around the receiver array.

During calibration, the transmitter is systematically moved along predefined paths and at varying heights and azimuth angles around the receiver array. This spatial diversity allows the system to probe the array response from multiple directions. The relative positions and orientations of the transmitter and each antenna element are continuously tracked using high-precision GNSS receivers, enabling accurate calculation of both the distance and the angle of arrival (DoA) for each measurement.

Channel estimation techniques, including Least Squares and analysis of the Channel Impulse Response, are employed to isolate the LoS components and compute the relative phase and amplitude offset between antennas. By combining the measured channel data with precise position and orientation information, the calibration process can compensate for deterministic effects due to geometry and propagation distance, ensuring that the extracted offsets reflect only the intrinsic differences between antenna elements.

Key components of the system include:

- Universal Software Radio Peripheral (USRP) devices for signal transmission and reception.
- High-precision GNSS receivers for real-time tracking of both transmitter and receiver positions, enabling centimeter-level accuracy in distance and angle calculations.
- MATLAB-based algorithms for frame detection, frequency correction, channel estimation, and mapping of antenna response as a function of transmitter position and angle.

Experiments were conducted in both controlled (anechoic chamber) and real-world (outdoor) environments. In each scenario, the transmitter was moved to various positions and orientations relative to the receiver array, and the corresponding distances and angles to each antenna element were recorded. This approach enabled a comprehensive analysis of the calibration method's reproducibility and robustness across a range of spatial configurations.

The experimental results confirm that integrating precise position and orientation data enables the proposed calibration framework to reliably estimate and correct phase and amplitude offsets between antenna elements. This validates the method's effectiveness for both controlled laboratory and real-world field environments. While the approach demonstrates strong potential for scalable, in-situ calibration, further research is required to optimize automation, address multipath effects, and extend applicability to larger and more complex array configurations.

### 1.3.1 Stakeholders

This project involves and benefits a diverse set of stakeholders:

- **NTNU and the SFI AutoShip initiative:** The research directly supports NTNU's strategic focus on autonomous maritime systems, with SFI AutoShip serving as a key application area for robust, field-deployable wireless communication solutions. The outcomes contribute to NTNU's leadership in next-generation maritime technology and digital infrastructure.

- **Industrial partners:** Companies and organizations developing or deploying MAMIMO technology in telecommunications, autonomous vehicles, and maritime systems stand to benefit from more efficient, scalable, and cost-effective calibration methods. The ability to perform in-situ calibration reduces operational downtime and infrastructure costs, making advanced wireless systems more accessible and reliable in demanding environments.
- **Research community:** The project advances the art of in-situ calibration methodologies, providing validated frameworks, open-source tools, and experimental data. This supports further research in wireless system calibration, channel sounding, and UAV-based measurement campaigns, and encourages reproducibility and collaboration.
- **UAV and GNSS technology developers:** The integration of high-precision GNSS and UAV platforms for calibration creates new opportunities for technology providers to address emerging needs in wireless infrastructure maintenance, testing, and deployment.
- **Public sector and regulatory bodies:** Improved calibration methods for wireless systems can enhance the reliability and safety of critical communication infrastructure, supporting public services, transportation, and emergency response in both urban and remote areas.

By addressing the needs of these stakeholders, the project not only advances academic knowledge but also delivers practical value to industry, technology developers, and society at large.

### 1.3.2 Sustainability Relevance

This thesis aligns with several United Nations Sustainable Development Goals (SDGs) by promoting efficient, scalable, and environmentally conscious approaches to wireless system calibration:

- **SDG 9 (Industry, Innovation, and Infrastructure):** The proposed drone-based and portable calibration methods reduce dependence on resource-intensive infrastructure such as anechoic chambers. This enables more scalable, flexible, and energy-efficient calibration processes, supporting the development of robust digital infrastructure for future wireless networks and autonomous systems.
- **SDG 13 (Climate Action):** By improving the reliability and efficiency of MAMIMO systems, the methodology supports the deployment of energy-efficient wireless networks. Enhanced calibration accuracy can lead to reduced transmission power, lower operational energy consumption, and a smaller carbon footprint for communication infrastructure. The ability to perform calibration in the field also reduces the need for transportation of equipment and personnel, further minimizing environmental impact.
- **SDG 17 (Partnerships for the Goals):** The project exemplifies collaboration between academia, industry, and research initiatives such as SFI

AutoShip. By sharing open-source tools, experimental data, and validated frameworks, the work fosters knowledge exchange and accelerates the adoption of sustainable technologies in wireless communications.

- **Resource Optimization and Circular Economy:** The flexible, field-deployable calibration approach extends the operational lifetime of wireless infrastructure by enabling ongoing maintenance and recalibration, reducing the need for premature hardware replacement and supporting a more circular approach to technology use.
- **Digital Inclusion and Societal Impact:** Improved calibration methods contribute to more reliable and accessible wireless networks, supporting digital inclusion and connectivity in both urban and remote areas (on the seas). This has positive implications for education, healthcare, and emergency response, aligning with broader sustainability and societal goals.

Overall, this work demonstrates how innovative engineering solutions can contribute to sustainable development by balancing technical performance, operational flexibility, and environmental responsibility in next-generation wireless systems.

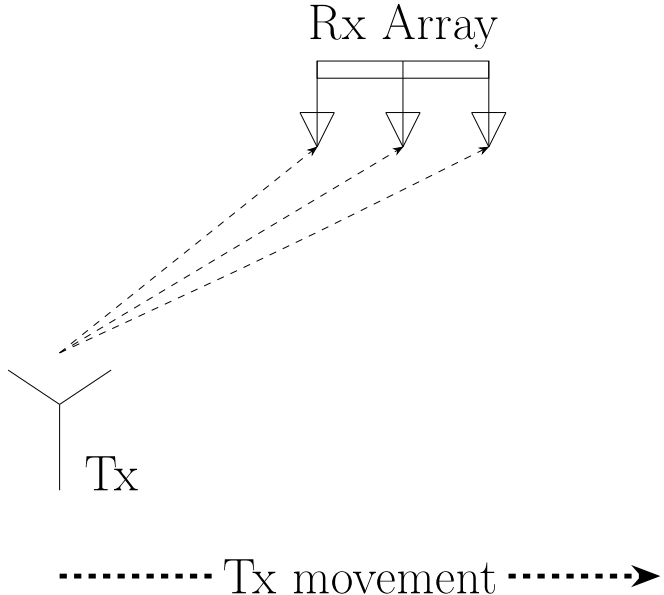


**Figure 1.3.1:** Illustration of the calibration setup. The transmitter (Tx), which can be a drone or another movable platform, is positioned at various locations relative to the receiver MIMO array (Rx Array) to enable in-situ calibration.

---

CHAPTER  
**TWO**

---

**THEORY**

## 2.1 Introduction

This chapter provides the theoretical foundation necessary for understanding the calibration of MIMO systems. It introduces key concepts including antenna array fundamentals, channel modeling, and channel estimation techniques, with a focus on the practical challenges encountered in real-world calibration. The chapter also discusses the characteristics of the LPDA antenna, the impact of fading, and the critical role of precise positioning and synchronization. Together, these topics establish the context and requirements for effective MIMO system calibration.

## 2.2 The Concept of Calibration

Calibration in MIMO systems is the process of identifying and compensating for systematic differences in phase and amplitude between antenna elements and their associated hardware chains. Correcting phase differences is particularly important, as unaddressed phase misalignments can cause destructive interference and significantly degrade beamforming performance. These differences arise from manufacturing tolerances, variations in cable lengths, connectors, RF front-ends, and other hardware imperfections. If left uncorrected, such discrepancies can significantly degrade the performance of beamforming, direction finding, spatial multiplexing, and overall system capacity.

The fundamental principle of calibration is to transmit a known signal from a reference source (such as a dedicated transmitter or a UAV-mounted transmitter) and measure the received response at each antenna element. The propagation medium (the channel) is modeled as a linear time-invariant (LTI) system, as illustrated in Figure 2.2.1. In this model, the channel acts as a finite impulse response (FIR) filter (see Figure 2.2.2), where the input signal  $x(t)$  is transformed into the output signal  $y(t)$  via the channel impulse response  $h(t)$ . The filter taps, with weights  $\alpha_n$  and delays  $z^{-1}$ , correspond to the physical propagation paths (line-of-sight and multipath reflections). The first tap, typically the strongest, represents the direct line-of-sight (LoS) path and is weighted by  $\alpha_1$ . This weight comprises a deterministic component (due to path loss and phase rotation from propagation

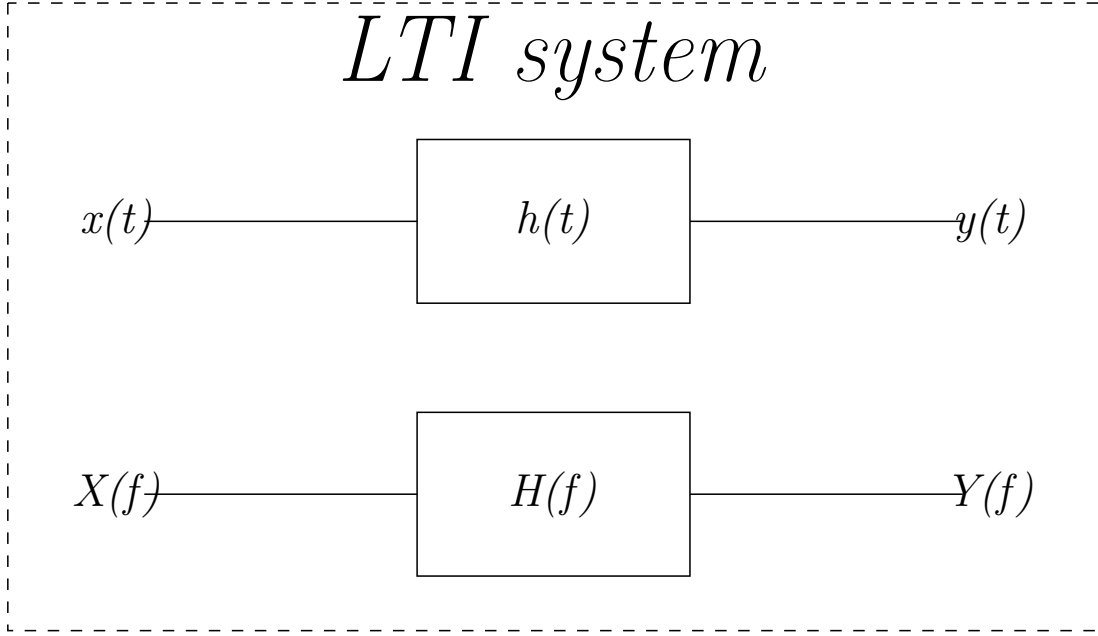


**Figure 2.2.1:** Illustration of a linear time-invariant (LTI) system, where the input signal  $x(t)$  is transformed into the output signal  $y(t)$  through the channel impulse response  $h(t)$ . The system can be represented in the frequency domain as  $H(f)$ , which relates the Fourier transforms of the input and output signals,  $X(f)$  and  $Y(f)$ , respectively.

distance) and an unknown, element-specific complex offset (denoted  $\epsilon$ ), which encapsulates hardware and antenna-specific effects.

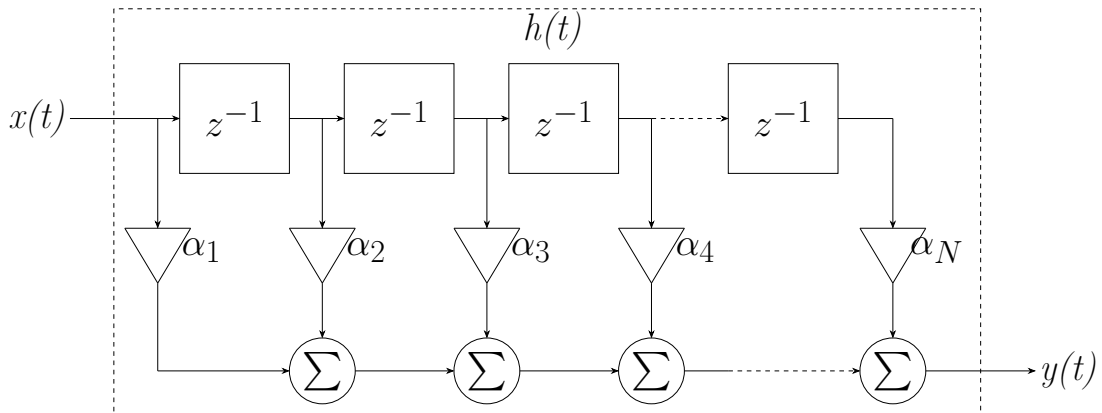


**Figure 2.2.2:** FIR filter representation of the channel, where each tap corresponds to a specific path in the channel. The weights  $\alpha_n$  represent the amplitude and phase response of each path, and the delays  $z^{-1}$  account for the propagation time. The first tap, typically the strongest, represents the direct line-of-sight (LoS) path. The output signal  $y(t)$  is a weighted sum of the input signal  $x(t)$  across all taps.

Calibration aims to estimate this unknown offset for each antenna element by first estimating  $\alpha_1$  through channel estimation, then compensating for the

deterministic propagation effects using precise knowledge of the transmitter and receiver positions. The residual, after compensation, is attributed to the hardware and antenna-specific offset  $\epsilon$ , which is assumed to be constant for each element over time and frequency (within the calibration bandwidth).

The calibration procedure involves the following steps:

1. **Transmission of a Known Signal:** A well-defined signal with favorable autocorrelation properties (such as a Zadoff-Chu sequence) is transmitted from a precisely known position.
2. **Channel Estimation:** The received signals at each antenna are processed to estimate the channel frequency response (CFR) and, via inverse Fourier transform or high-resolution methods, the channel impulse response (CIR), focusing on the LoS component.
3. **Distance and Path Compensation:** The geometric distance between the transmitter and each antenna is used to compute and remove the deterministic phase and amplitude effects due to free-space path loss and propagation delay.
4. **Relative Offset Identification:** After compensating for distance and path effects, the residual complex number is attributed to hardware and antenna-specific constants. The offsets are determined by comparing (complex division) the constant values of each antenna element to that of a selected reference element.
5. **Application of Calibration:** The extracted offsets are stored and subsequently applied to future measurements or transmissions, aligning the phase and amplitude across the array for coherent operation.

By systematically applying these steps, calibration ensures that the array operates as a coherent system (relative to the selected reference antenna), enabling accurate spatial processing, optimal beamforming, and reliable measurements. Accurate calibration is essential for realizing the theoretical gains of MIMO and MAMIMO systems in practical deployments.

## 2.3 The Antenna

An antenna is a device that converts electrical signals into electromagnetic waves and vice versa. It is a crucial component in wireless communication systems, as it enables the transmission and reception of signals over the air. The performance of an antenna is characterized by its radiation pattern  $G(r)$ , gain, polarization, and impedance ( $Z$ ) [2, 3, 4].

No two antennas are identical, even if they are manufactured to the same specifications. Antennas of the same type and design can exhibit different electrical characteristics due to manufacturing tolerances, environmental factors, or variations in the connection interfaces. For instance, when connecting a coaxial cable to an antenna, the impedance at the junction may deviate from the nominal value by an unknown amount. This mismatch can introduce variations in key parameters such as phase ( $\varphi$ ) and gain ( $\alpha$ ).

In MIMO systems, antennas are typically arranged in arrays to exploit spatial diversity and enhance communication performance through techniques like beamforming and spatial multiplexing [2]. However, if individual antenna elements within the array exhibit significant and uncharacterized discrepancies, particularly in phase response, beamforming accuracy can be severely compromised. Therefore, precise calibration of the antenna array is essential to ensure coherent operation, maximize array gain, and achieve the desired system performance. Section 2.3.2 provides a detailed description of the LPDA antenna used in NTNU MAMIMO testbed, which is the focus of this project.

### 2.3.1 MIMO

MIMO is a technology that uses multiple antennas elements for transmitting and receiving. Using multiple antennas can increase the capacity of the channel, increase the data rate, and improve the reliability of the communication by increasing the diversety [2]. Multipale antennas unlocks the possibility of beamforming, allowing the comunication system to direct the signal in a specific direction.

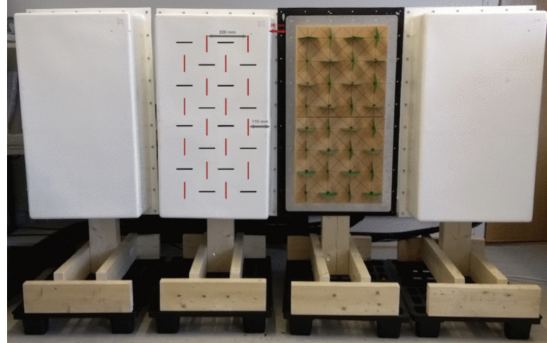


**Figure 2.3.1:** Photograph of the NTNU MAMIMO testbed, comprising four subarrays. Each subarray contains  $8 \times 4$  LPDA elements, enabling greater capasety [5].

### 2.3.2 LPDA antenna

The LPDA is a directional antenna that is used for wideband applications. The specific LPDA used in the MAMIMO testbed and this project is developed internally at NTNU [6]. It is designed to operate from 1.3 GHz to 6 GHz, offering a half-power beamwidth of approximately  $110^\circ$  in the H-plane and  $70^\circ$  in the E-plane [5]. It consist of eleven dipole elements seen in Figure 2.3.2. In Figure 2.3.3 to Figure 2.3.10, the simulated radiation patterns at different frequencies demonstrate the directional characteristics of the antenna [6].



**Figure 2.3.2:** The LPDA antenna element used in the NTNU MAMIMO testbed.

LPDA Specification	Value
Frequency Range	1.3 GHz – 6 GHz
Number of Elements	11 dipoles
Half-Power Beamwidth (H-plane)	~110-150°
Half-Power Beamwidth (E-plane)	~70-80°
Typical Gain	6–7 dBi
Input Impedance	50 Ω
Connector Type	QMA
Dimensions	~11 cm × 9.5 cm
Return loss	< 10 dB

**Table 2.3.1:** Technical specifications of the LPDA antenna element used in the NTNU MAMIMO testbed [6].

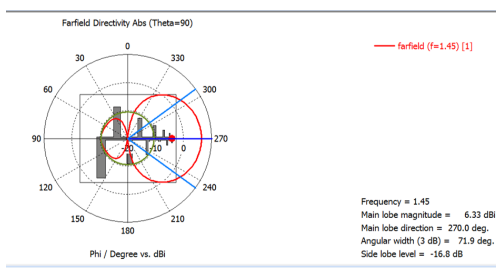


**Figure 2.3.3:** E-plane, 1.45 GHz [6]

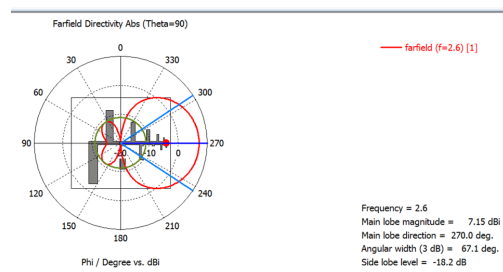


**Figure 2.3.4:** E-plane, 2.6 GHz [6]

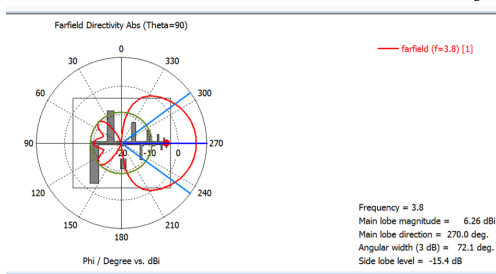


**Figure 2.3.5:** E-plane, 3.8 GHz [6]

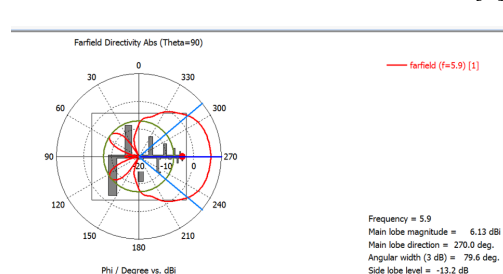


**Figure 2.3.6:** E-plane, 5.9 GHz [6]

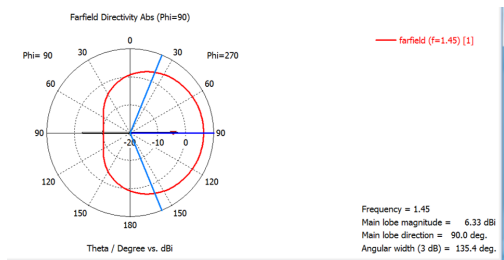


**Figure 2.3.7:** H-plane, 1.45 GHz [6]

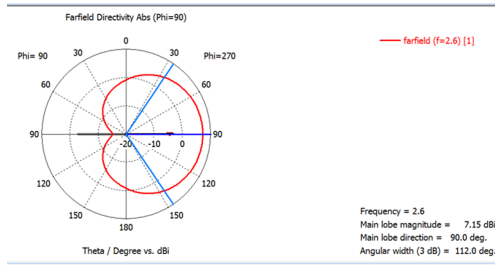


**Figure 2.3.8:** H-plane, 2.6 GHz [6]

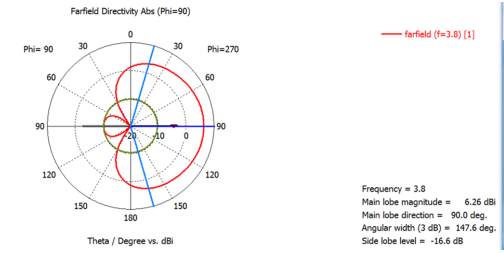


**Figure 2.3.9:** H-plane, 3.8 GHz [6]

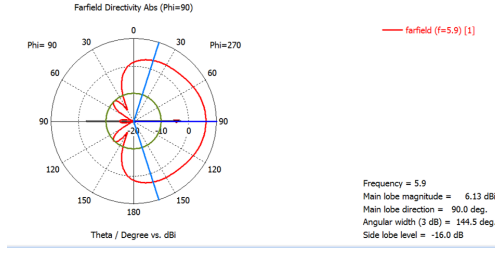


**Figure 2.3.10:** H-plane, 5.9 GHz [6]

The gain and phase response of an antenna's radiation pattern are inherently functions of the direction of arrival (DoA) or direction of departure (DoD) of the electromagnetic wave. These characteristics become embedded within the overall channel response, as discussed in section 2.4. For antenna arrays, the spatial variation in DoA across different elements, due to their physical separation, introduces element-specific amplitude and phase responses. This spatial dependency is a critical consideration in the calibration of multi-antenna systems, as unaccounted variations can degrade the calibration quality.

In idealized scenarios, the incident wavefront is assumed to be planar, which is a valid approximation when the transmitter is located at a distance much greater than the array aperture (far-field condition). Under this assumption, the DoA is approximately identical for all array elements, simplifying the calibration process. However, in practical measurement campaigns, such as the one described in this project, this far-field condition is not satisfied, and the incoming wavefront exhibits curvature (near-field effects). Consequently, the gain and phase response must be characterized as explicit functions of the DoA for each antenna element.

Mathematically, the complex gain of the antenna as a function of direction is given by Equation 2.1, where  $G(\phi, \theta)$  denotes the complex radiation pattern,  $\alpha(\phi, \theta)$  is the direction-dependent amplitude response, and  $\varphi(\phi, \theta)$  is the corresponding phase response. Here,  $(\phi, \theta)$  are the spherical coordinates specifying the DoA (or DoD) of the incident (or departing) wave. Accurate modeling and calibration of these parameters are essential for precise channel characterization and for mitigating systematic errors in the calibration. For simplicity, the spherical coordinates are reduced to a single variable  $r$ , which represents the DoA in a simplified manner, as shown in Equation 2.1.

The mathematical expression in Equation 2.1 serves as the fundamental model for describing the complex gain of the antenna as a function of direction. This model captures both the amplitude and phase response of the antenna for any given direction of arrival or departure, and is essential for accurate characterization and calibration of the antenna in the system.

$$G(\phi, \theta) = \alpha(\phi, \theta) \cdot e^{j\varphi(\phi, \theta)} = G(r) = \alpha(r) \cdot e^{j\varphi(r)} \quad (2.1)$$

The phase center of the LPDA antenna is a critical parameter in calibration and channel modeling. It represents the effective point from which the antenna appears to radiate or receive electromagnetic waves, and serves as the reference for position and distance calculations. For the LPDA used in this project, the phase center is frequency-dependent and was characterized using vector network analyzer (VNA) measurements, as detailed in [1].

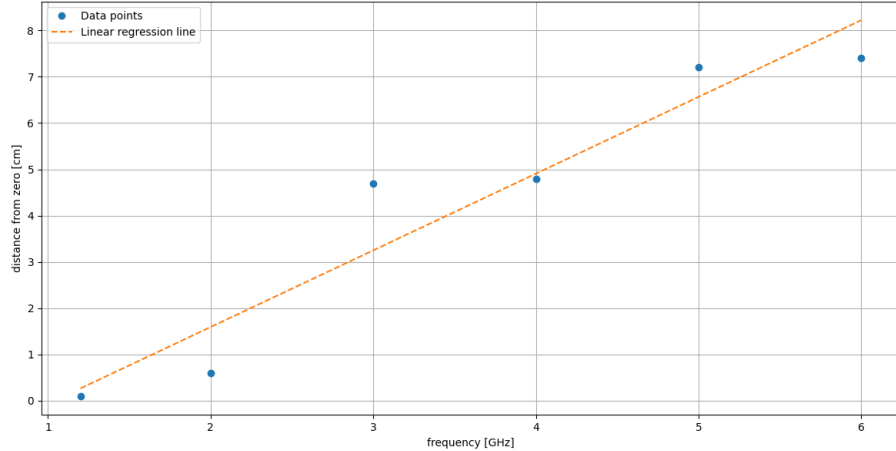


**Figure 2.3.11:** Measured phase center position of the LPDA antenna as a function of frequency. The phase center shifts with frequency, introducing uncertainty in distance and phase calculations if not properly accounted for. Linear regression is used to estimate the trend, but measurement uncertainty remains significant [1].

## 2.4 The Channel

When transmitting a signal, it propagates from the transmitter to the receiver through a medium, which can be over the air or a cable. The term "channel" refers to this medium through which the signal travels [2]. In wireless communication, the channel primarily consists of the air, but also includes antennas, cables, and other components that affect the signal before it is sampled and digitized by the receiver. Understanding the channel is crucial for calibrating the MIMO system, as the channel affects the signal in various ways, such as attenuation, phase shift, and multipath fading.

The channel is often viewed as a filter with an impulse response  $h(t)$  and a frequency response  $H(f)$  [2]. Mathematically the CIR can be modeled as a delta train with complex weights  $\alpha_n$  and time delays  $\tau_n$ , as given by Equation 2.2. Every  $n$ -th delta function represents a path (often referred to as a tap) from the transmitter to the receiver where the first delta function represents the shortest path (usually the LoS). The subsequent delta functions represent paths with reflections. Figure 2.4.1 and Figure 2.4.2 show an example of a multipath propagation environment and a corresponding CIR.

$$h(t) = \sum_{n=1}^N \alpha_n \delta(t - \tau_n) \quad (2.2)$$

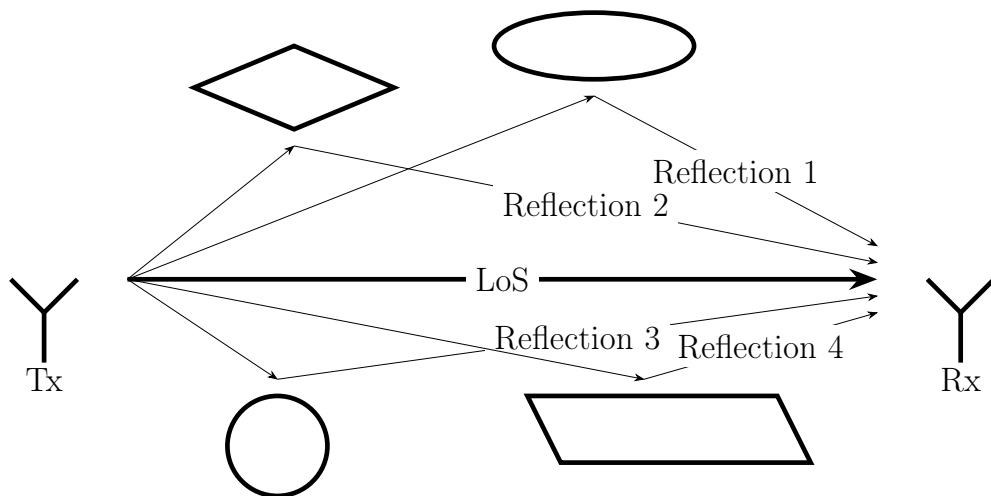


**Figure 2.4.1:** Illustration of a multipath propagation environment. The direct path (LoS) is typically the shortest and strongest, while additional reflected paths arise from objects at various locations and distances relative to the receiver. Each propagation path corresponds to a distinct tap in the CIR, as exemplified in Figure 2.4.2.

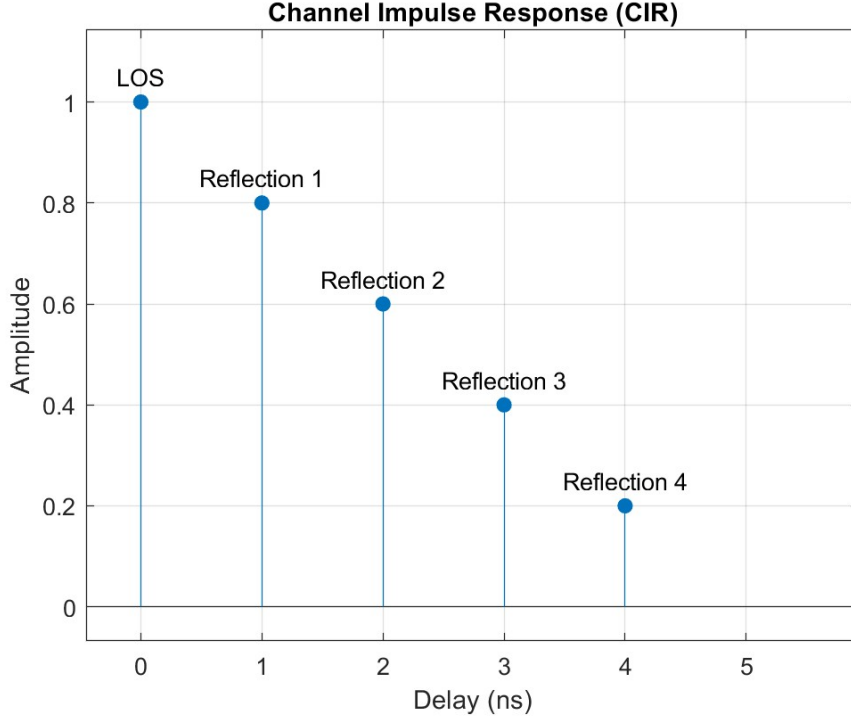


**Figure 2.4.2:** Example of a CIR exhibiting five distinct taps. The first and strongest tap corresponds to the direct LoS path, while the subsequent taps represent multipath components arising from reflections off various objects at different distances and delays. This CIR is based on the multipath environment illustrated in Figure 2.4.1.

$\alpha_n$  in Equation 2.2 is complex and represent the attenuation and phase shift of the path experienced by the signal.  $\tau_n$  represent the time light uses from the Tx to the Rx and is proposional to the path distance ( $d_n$ ) shown in Equation 2.3.

$$\tau_n = \frac{d_n}{c} \quad (2.3)$$

The free-space path loss (FSPL), denoted as  $L$ , quantifies the reduction in signal power as an electromagnetic wave propagates through free space from a transmitting to a receiving antenna, as defined in Equation 2.4a [2]. FSPL is a fundamental parameter in wireless system calibration, as it directly impacts the received signal strength and is governed by both the separation distance  $d$  and the signal wavelength  $\lambda$ . While the FSPL equation assumes ideal isotropic antennas, practical antennas exhibit direction-dependent gain, necessitating the inclusion of the antenna gain pattern  $G(r)$  (see Equation 2.1) to accurately model the total path loss.

In the context of calibration, the complex amplitude  $\alpha$  for each multipath component incorporates not only the effects of FSPL and antenna gain, but also an unknown, element-specific complex offset  $\epsilon$  (encompassing both amplitude and phase, and is also different for every antenna element). This offset arises from hardware imperfections and variations between antenna elements, and its accurate estimation and compensation are central objectives of the calibration process. The resulting model for the complex amplitude of each channel tap is summarized

in Equation 2.4d, which forms the basis for subsequent calibration and channel estimation procedures.

$$L = FSPL = \left( \frac{4\pi d}{\lambda} \right)^2 \quad (2.4a)$$

$$|\alpha| = \sqrt{\frac{1}{L}} \times |G(r)| \times |\epsilon| \quad (2.4b)$$

$$\angle \alpha = \phi = -2\pi f_c \tau + \angle G(r) + \angle \epsilon \quad (2.4c)$$

$$\alpha = \sqrt{\frac{1}{L}} \times |G(r)| \times |\epsilon| \cdot e^{(-j2\pi f_c \tau + \angle G(r) + \angle \epsilon)} \quad (2.4d)$$

The phase shift  $\phi$  ( $\angle \alpha$ ) experienced by a propagating signal is fundamentally determined by the propagation distance and the carrier frequency, as described in Equation 2.4c. Specifically, the phase shift accumulates linearly with distance, such that longer propagation paths result in greater phase rotation.

$$\phi = -2\pi f \tau = \frac{-2\pi d}{\lambda} = -2\pi f \frac{d}{c} = \angle \mathcal{F}\{\delta(t - \tau)\} \quad (2.5)$$

The phase shift described in Equation 2.5 is a fundamental component in modeling the channel frequency response. The CFR, which is the Fourier transform of the CIR (see Equation 2.6), is detailed in Equation 2.7. In this context,  $A_n$  represents the complex amplitude of the  $n$ -th multipath component in the frequency domain, encapsulating the effects of path attenuation, phase shift due to propagation delay, antenna gain, and the element-specific complex offset. The carrier frequency  $f_c$  and the baseband frequency  $f$  together determine the total frequency at which the phase rotation occurs.

$$\alpha_n \delta(t - \tau_n) = \mathcal{F}^{-1}\{A_n e^{\phi_n}\} \quad (2.6)$$

$$h(t) = \sum_{n=1}^N \alpha_n \delta(t - \tau_n) = \sum_{n=1}^N |\alpha_n| e^{(-j2\pi f_c \tau_n + \angle G_n(r) + \angle \epsilon)} \cdot \delta(t - \tau_n) \quad (2.7a)$$

$$H(f) = \sum_{n=1}^N A_n e^{j\phi_n} = \sum_{n=1}^N A_n e^{-j2\pi f \tau_n} = \sum_{n=1}^N |A_n| e^{(-j2\pi \tau_n (f_c + f) + \angle G_n(r) + \angle \epsilon)} \quad (2.7b)$$

It is important to recognize that each  $k$ -th antenna element in a MIMO array experiences a distinct channel response. This uniqueness arises from two primary factors: (1) the element-specific complex offset  $\epsilon_k$ , which encapsulates hardware imperfections and manufacturing tolerances (see Equation 2.8a), and (2) the spatial position of each antenna element, which leads to different propagation delays  $\tau_{n,k}$  for each multipath component (see Equation 2.8b). As a result, the CIR for each antenna element exhibits unique amplitude and phase characteristics for each tap. Also in multipath environments, additional phase shifts to the taps may be

introduced by reflections, which can impart a phase change of  $\pi$  radians ( $180^\circ$ ), depending on the reflection geometry and the properties of the reflecting surface [3].

$$G(r)_k = G(r) \times \epsilon_k \quad (2.8a)$$

$$h_k(t) = \sum_{n=1}^N \alpha_{n,k} \delta(t - \tau_{n,k}) \quad (2.8b)$$

The channel is modeled as a LTI filter, where the transmitted signal  $x(t)$  is convolved with the CIR  $h(t)$  to produce the received signal  $y(t)$ , with additive noise  $n(t)$  [2]. This relationship is fundamental in communication systems and forms the basis for channel estimation techniques. Convolution in the time domain corresponds to multiplication in the frequency domain, which greatly simplifies analysis and processing. This duality is central to the channel estimation approach used in this project, as discussed in subsection 2.4.1. The mathematical relationships are shown in Equation 2.9a and Equation 2.9b.

$$y(t) = x(t) * h(t) + n(t) \quad (2.9a)$$

$$Y(f) = X(f)H(f) + \mathcal{N}(f) \quad (2.9b)$$

In practical digital communication systems, signals are sampled at a finite rate  $f_s$ , resulting in a limited observation bandwidth. This is mathematically equivalent to applying a rectangular window to the  $H(f)$ . Due to the Fourier transform properties, multiplication by a rectangular window in the frequency domain corresponds to convolution with a sinc function in the time domain. As a result, the estimated  $h(t)$  is not the true impulse response, but rather a windowed version where each tap is smeared by the sinc function. This effect, known as spectral leakage or the Gibbs phenomenon, causes the energy of each tap to spread, potentially obscuring closely spaced multipath components and introducing ringing artifacts. Understanding this limitation is crucial for accurate interpretation of measured CIRs and for designing effective channel estimation algorithms [2].

$$h_{\text{windowed}}(t) = h(t) * \text{sinc}(t) \quad (2.10a)$$

$$H_{\text{windowed}}(f) = H(f) \cdot \text{rect}(f/f_s) \quad (2.10b)$$

### 2.4.1 Channel Estimation

Channel estimation is a fundamental step in the MIMO system calibration, as it enables the characterization of the propagation environment between each transmit and receive antenna pair. One of the most widely used techniques for channel estimation is the Least Squares (LS) estimator, which provides a simple and computationally efficient means of estimating the CFR when the transmitted signal is known.

The LS estimator operates in the frequency domain and is defined in Equation 2.11. Given the received signal  $Y(f)$  and the known transmitted signal  $X(f)$ , the CFR estimate  $\hat{H}_{\text{LS}}(f)$  is obtained by dividing the received spectrum by the

transmitted spectrum. This method assumes that  $X(f)$  is nonzero across the bandwidth of interest and that the system is linear and time-invariant over the observation interval.

$$\hat{H}_{LS}(f) = \frac{Y(f)}{X(f)} \quad (2.11a)$$

$$\hat{H}_{LS}(f) = H(f) + \frac{\mathcal{N}(f)}{X(f)} \quad (2.11b)$$

Here,  $\mathcal{N}(f)$  denotes the additive noise in the frequency domain. The accuracy of the LS estimator depends on the signal-to-noise ratio (SNR) and the spectral properties of  $X(f)$ . If  $X(f)$  has low magnitude at certain frequencies, the noise term is amplified, leading to unreliable estimates in those regions. Therefore, it is essential to design  $X(f)$  to have a flat spectrum over the system bandwidth. In this project, a pseudorandom QPSK sequence is used as the data payload to ensure spectral flatness, while a known preamble (such as a Zadoff-Chu sequence) is employed for synchronization and timing acquisition.

While the LS estimator is attractive due to its simplicity and low computational complexity, it is sensitive to noise and may yield suboptimal performance in low SNR scenarios. In such cases, more advanced estimators, such as minimum mean square error (MMSE) or high-resolution spectral estimation methods (e.g., APES, see subsection 2.4.2), may be employed to improve estimation accuracy [7].

### 2.4.2 The forward-and-backward APES

The forward-and-backward APES (Amplitude and Phase Estimation) algorithm is a high-resolution spectral estimation method that utilizes both forward and backward data to estimate the complex spectrum of an observed signal. High-resolution spectral estimation methods aim to provide improved frequency resolution compared to conventional Fourier techniques [8, 9]. The matlab implementation used can be found in appendix F2.4 and is based on [10] and is in this project used to estimate the CIR.

### 2.4.3 Finding the constant offset

After successfully estimating the CFR, the CIR can be computed using either the IFFT (inverse fourier transform) or high-resolution methods such as APES. The next step is to identify the LoS tap, which typically exhibits the largest magnitude due to its minimal path loss, but can also be found when knowing the delay from Tx to Rx. As described in section 2.4, the phase and magnitude of the LoS taps are partly deterministic by the propagation distance, while antenna gain and a constant complex offset arising from hardware imperfections are unknown.

If the positions of the Tx and Rx are accurately known, the distance-dependent phase and magnitude can be compensated for, isolating the antenna-specific offset. This compensation is formalized in Equation 2.12b, where the expected free-space response  $\beta$  is computed in Equation 2.12a.

$$\beta = \sqrt{\frac{1}{L}} \cdot e^{-j2\pi f_c \tau} \quad (2.12a)$$

$$G(r)_k \cdot \epsilon_k = \frac{\alpha_{LoS,k}}{\beta_k} \quad (2.12b)$$

Here,  $L$  is the FSPL,  $f_c$  is the carrier frequency, and  $\tau$  is the propagation delay corresponding to the LoS distance. Dividing the measured LoS tap  $\alpha_{LoS}$  by  $\beta$  removes the deterministic effects of distance and frequency, leaving only the combined antenna gain  $G(r)_k$  and the element-specific offset  $\epsilon_k$ .

In practice, the primary parameter of interest is the relative offset or ratio  $\Delta\epsilon_k$  between antenna elements. The antenna gain  $G(r)_k$  can be neglected only if all antennas are nearly identical and the DoA is approximately the same for each element (a conditions that is met when the Tx is located far from the Rx array). However, increasing the Tx-Rx distance also increases the risk of multipath fading, as the power difference between the LoS and reflected paths diminishes (see subsection 2.4.4).

When the Tx is positioned closer to the array, the DoA varies across elements, making the antenna gain  $G(r)_n$  direction-dependent and non-negligible. In this scenario, it is necessary to characterize the antenna pattern as a function of direction. This can be achieved by recording the distance-compensated LoS tap for each element, along with precise timestamps and corresponding Tx positions. For each measurement, the azimuth and elevation angles are computed, enabling the construction of a 2D or 3D map of the antenna pattern over the measured DoAs. Interpolating these measurements yields a continuous estimate of the antenna gain pattern, which can then be used to accurately extract the constant offset  $\epsilon$  for each antenna element.

Accurate synchronization between the channel measurements and the Tx position data is essential for this process. This approach enables both the calibration of the relative offsets and the empirical characterization of the antenna patterns, improving the overall accuracy of the MIMO system calibration.

Since the primary objective is to determine the relative differences between the  $\epsilon_k$  offsets for the array elements, it is customary to select one element (e.g.,  $k = 1$ ) as a reference. The relative offset or ratio  $\Delta\epsilon_k$  between the  $k$ -th element and the reference is then defined as the ratio of their respective offsets, as shown in Equation 2.13a. This ratio is a complex number that, when multiplied with the measured response of the  $k$ -th element, aligns its amplitude and phase with those of the reference. Specifically, the amplitude of  $\Delta\epsilon_k$  represents the relative gain, while its angle represents the relative phase shift. The choice of reference is arbitrary; the reference element will always have  $\Delta\epsilon_k = 1$ , corresponding to zero phase difference and unit amplitude.

$$\Delta\epsilon_k = \frac{\epsilon_k}{\epsilon_1} \quad (2.13a)$$

$$\epsilon_1 = \Delta\epsilon_k \cdot \epsilon_k \quad (2.13b)$$

This approach is based on the assumption that if all antenna elements exhibit identical gain and phase responses (or, equivalently, identical systematic errors), the array can be considered fully calibrated for practical purposes. In this ideal scenario, any residual differences between elements are negligible and do not impact the performance of beamforming.

### 2.4.4 Fading

Fading refers to random fluctuations in the received signal power, resulting from the constructive and destructive interference of multiple propagation paths between the transmitter and receiver. These fluctuations are caused by a combination of effects, including multipath propagation (reflections, diffraction, and scattering), shadowing by obstacles, and the inherent variability of the propagation environment [2, 1]. Fading is typically categorized into two main types: large-scale fading and small-scale fading.

Large-scale fading describes the gradual variation in the average received signal power over distances of several wavelengths, primarily due to path loss and shadowing from large objects such as buildings or terrain. This type of fading is often modeled as a log-normal random process superimposed on the deterministic path loss curve. In contrast, small-scale fading refers to rapid fluctuations in signal amplitude and phase over short distances or time intervals, typically on the order of a wavelength. Small-scale fading is primarily caused by the interference of multiple signal components arriving at the receiver with different delays, phases, and amplitudes.

In the context of the *in-situ* MIMO system calibration, fading poses a significant challenge, as it can obscure the true channel response and introduce uncertainty in the estimation of antenna-specific offsets. To mitigate the impact of fading during calibration, it is essential to maximize the power of the LoS component relative to reflected and scattered paths. This can be achieved by positioning the system in environments with minimal reflective surfaces, such as elevated locations (e.g., rooftops or hills), or by ensuring that the transmitter is located sufficiently far from potential reflectors. For airborne measurements, flying the transmitter (e.g., using a drone) in close proximity to the elevated receiver array and ensuring an unobstructed LoS can significantly reduce multipath effects.

However, increasing the distance between the transmitter and receiver also reduces the attenuation difference between the LoS and reflected paths, as described by the FSPL in Equation 2.4a. As the distance increases, the LoS and reflected paths become more parallel, making their path lengths and received powers increasingly similar. This increases the likelihood of deep fades due to destructive interference, potentially resulting in severe signal attenuation or even complete signal cancellation. This phenomenon is illustrated in Figure 2.4.3 and quantified in Figure 2.4.4, which show how the attenuation difference diminishes with increasing distance.

To avoid severe fading, it is generally recommended to keep the transmitter within 10 to 20 meters of the receiver array during calibration, as supported by simulations in [1]. This distance strikes a balance between minimizing multipath effects and maintaining a sufficiently strong LoS component. Alternatively, placing the receiver array on a steep elevation, such as a cliff or tall building, can effectively block ground reflections and other multipath components, as illustrated in Figure 2.4.5. While this approach simplifies the measurement setup and reduces the need for airborne platforms, it requires access to suitable locations with minimal surrounding reflectors.

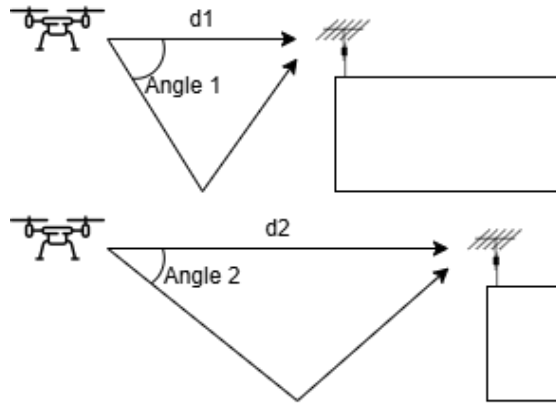


**Figure 2.4.3:** As the distance between the transmitter and receiver increases, the angle between the LoS and reflected paths decreases, causing the received power from reflections to approach that of the LoS. This increases the risk of deep fades due to destructive interference.

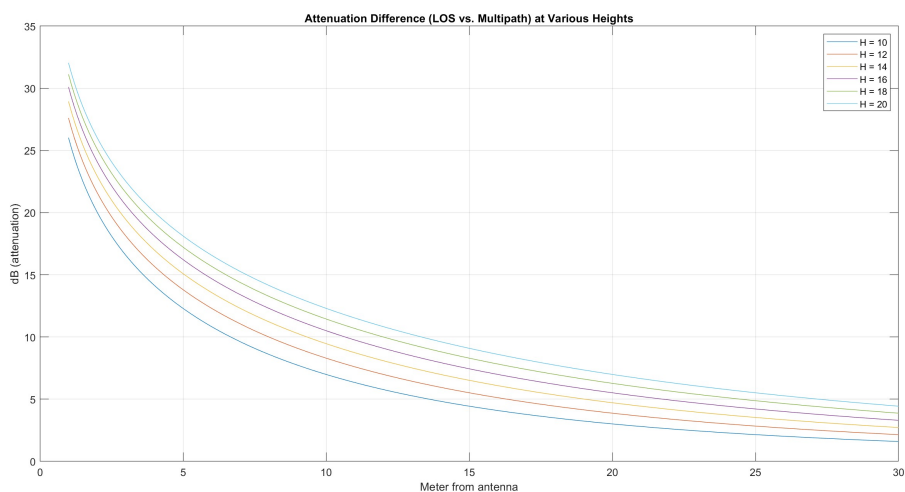


**Figure 2.4.4:** Attenuation difference between the LoS and a single multipath component as a function of the distance between Tx and Rx. The plot demonstrates that as the distance increases, the attenuation difference decreases, thereby increasing the likelihood of fading. (Assumes no additional attenuation from the reflecting surface) [1].

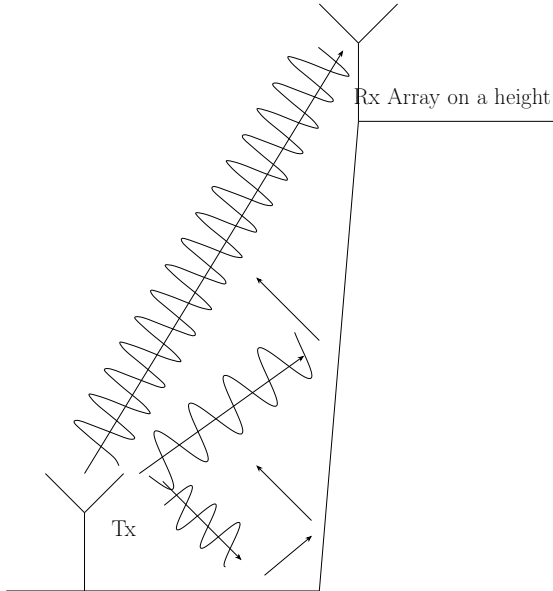


**Figure 2.4.5:** Placing the receiver array on top of a steep elevation (e.g., cliff, hill, or building) can block many multipath reflections, allowing the LoS path to dominate. This approach reduces fading and simplifies the calibration equipment, but requires access to suitable locations.

## 2.5 UAV

An Unmanned Aerial Vehicle (UAV), commonly known as a drone, is an aircraft that operates without a human pilot onboard. UAVs are controlled either autonomously by onboard computers or remotely by a human operator. They are widely used in various applications, including aerial photography, surveying, environmental monitoring, and wireless communications research. In the context of this project, a UAV is proposed to carry the transmitter, enabling flexible positioning and precise control over the transmitter's location and altitude. This mobility is particularly advantageous for calibration measurements, as it allows for the collection of data at various positions and angles relative to the receiver array, facilitating accurate characterization of the antenna patterns and channel responses.

## 2.6 Anechoic Chamber

An anechoic chamber is a room designed to completely absorb reflections of sound or electromagnetic waves. Anechoic chambers are used for testing and calibrating antennas, as they provide a controlled environment with minimal external interference. The walls, floor, and ceiling of the chamber are lined with electromagnetic-absorbing materials, which help to eliminate echoes and reflections. This allows for accurate measurements of the antenna's radiation pattern, gain, and other performance characteristics.

## 2.7 GNSS Positioning

Accurate knowledge of the Tx position is essential for precise MIMO system calibration. Even small errors in position can introduce significant phase errors, as demonstrated by simulations in [1] (see Figure 2.7.1). Global Navigation Satellite System (GNSS) technology provides position estimates by triangulating signals from multiple satellites. Standard GNSS typically achieves an accuracy of 1–5 meters under open-sky conditions [11], which is insufficient for high-precision calibration tasks where centimeter-level accuracy is required.

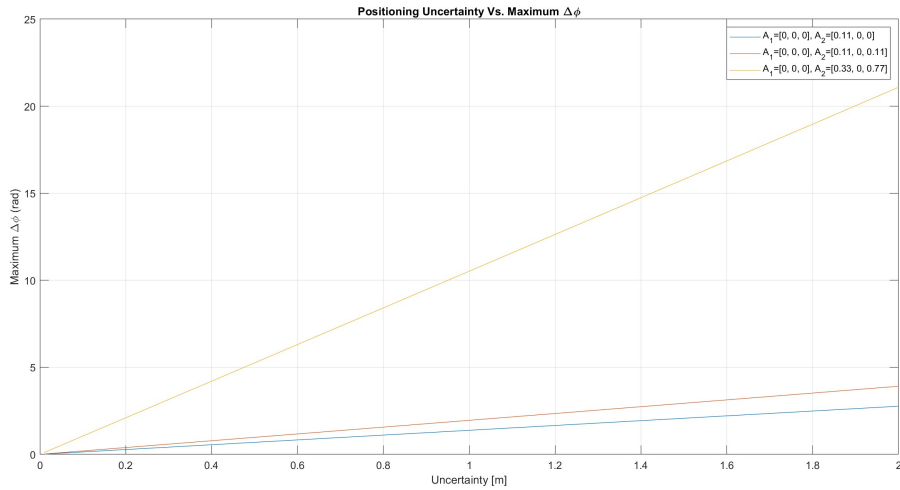


**Figure 2.7.1:** Simulated maximum phase error caused by GNSS position uncertainty, plotted as a function of the uncertainty radius (for 6 GHz). The uncertainty region is modeled as a sphere of radius  $r$  centered at the true receiver position, representing the possible range of measured positions. The transmitter is fixed at Cartesian coordinates (0, 10, 0). The curves show the phase difference error  $\Delta\theta$  between two example antenna positions ( $A_1$  and  $A_2$ ), demonstrating that even centimeter-scale position errors can introduce substantial phase errors between array elements. This underscores the necessity of centimeter-level GNSS accuracy for reliable MIMO calibration [1].

### 2.7.1 Real-Time Kinematic (RTK) GNSS

To overcome the accuracy limitation, Real-Time Kinematic (RTK) GNSS is employed. RTK enhances standard GNSS by using carrier-phase measurements and differential corrections from a fixed reference station at a known location. The reference station transmits correction data to the mobile receiver (e.g., on the drone), enabling it to resolve ambiguities and achieve position accuracies on the order of 1–2 centimeters [12]. This level of precision is critical for accurately compensating for distance-dependent phase shifts and for mapping the direction of arrival DoA during calibration.

## 2.8 Software-Defined Radio

A Software-Defined Radio (SDR) is a flexible radio communication system in which traditional hardware components, such as mixers, filters, amplifiers, modulators/demodulators, and detectors, are instead implemented in software on a general-purpose computer or embedded processor [13]. This architecture enables rapid reconfiguration of key parameters such as modulation scheme, frequency, bandwidth, and coding, simply by updating the software. As a result, SDR technology supports a wide range of applications, including wireless communications, spectrum monitoring, military systems, and scientific research [13].

In this project, two Universal Software Radio Peripheral (USRP) devices from Ettus Research (B210) are employed as the SDR platform. The USRP series is widely used in academia and industry due to its versatility, open-source support, and compatibility with multiple software frameworks, including GNU Radio, LabVIEW, MATLAB, and Simulink [14, 15].

Specification	Value
RF Coverage	70 MHz – 6 GHz
MIMO Configuration	2 TX & 2 RX (Half/Full Duplex)
FPGA	Xilinx Spartan 6 XC6SLX150
Instantaneous Bandwidth	Up to 56 MHz (1x1 Mode) Up to 30.72 MHz (2x2 Mode)
ADC Sample Rate (Max)	61.44 MS/s
ADC Resolution	12 bits
DAC Sample Rate (Max)	61.44 MS/s
DAC Resolution	12 bits
Host Sample Rate (16-bit)	61.44 MS/s
Connectivity	USB 3.0 SuperSpeed (Backward-compatible with USB 2.0)
Power Supply	External DC Power (6V)
GPIO Capability	Supported
Frequency Accuracy	$\pm 2.0$ ppm
Dimensions	9.7 × 15.5 × 1.5 cm
Weight	350 g

**Table 2.8.1:** Technical specifications of the USRP B210 [15].

### 2.8.1 Carrier Frequency Offset

Carrier Frequency Offset (CFO) arises from small frequency mismatches between the local oscillators of the transmitter and receiver. Even with high-quality oscillators, such as those in the USRP devices used in this project, small offsets typically remain due to manufacturing tolerances, temperature variations, and aging effects. CFO manifests as a frequency shift in the received signal, result-

ing in a time-varying phase rotation that, if uncorrected, can degrade channel estimation and demodulation accuracy.

Mathematically, if the transmitted baseband signal is  $x(t)$ , the received signal affected by a CFO of  $\Delta f$  can be modeled as shown in Equation 2.14 [2, 13], where  $y(t)$  is the received signal. The channel is assumed to be ideal for simplicity.

$$y(t) = x(t) \cdot e^{j2\pi\Delta ft} \quad (2.14)$$

This exponential term introduces a linear phase rotation over time. In the frequency domain, the effect of CFO is a shift of the spectrum shown in Equation 2.15.

$$Y(f) = X(f - \Delta f) \quad (2.15)$$

For a discrete-time system with sampling interval  $T_s$ , the phase rotation per sample is given by Equation 2.16, where  $n$  is the sample index.

$$\theta[n] = 2\pi\Delta f n T_s \quad (2.16)$$

This phase rotation causes the estimated channel frequency response  $\hat{H}_{LS}(f)$  to be distorted, leading to errors in the channel estimation.

CFO can be estimated and compensated using a known preamble sequence that is repeated (e.g., two identical halves), enabling robust frequency synchronization. One widely used approach is the Moose algorithm [16], which exploits the phase difference between repeated preamble segments to estimate the frequency offset. Once the CFO is estimated, it can be compensated by multiplying the received signal by a complex exponential with the opposite frequency offset, effectively rotating the phase back to its original state.

## 2.9 Packet-Based Communication

Packet-based communication refers to the transmission of data in discrete packets or frames, as opposed to a continuous stream. In this project, the transmitter repeatedly sends identical packets, each consisting of a known preamble followed by a data payload. This structure facilitates synchronization, channel estimation, and detection in the presence of noise.

The preamble is designed to enable accurate timing synchronization and frequency offset estimation, while the payload employs a pseudorandom QPSK sequence to ensure spectral flatness and reliable channel estimation across the entire system bandwidth (see subsection 2.9.1 and subsection 2.9.2).

### 2.9.1 Zadoff-Chu Sequence

The Zadoff-Chu (ZC) sequence is a complex-valued, constant-amplitude sequence with ideal periodic autocorrelation properties, making it highly suitable for synchronization and channel estimation tasks [17]. ZC sequences are extensively used in standards such as LTE for random access and synchronization. In this project, the ZC sequence serves as the preamble, enabling precise frame detection and timing synchronization, and providing robustness against frequency offsets due to its

favorable correlation characteristics. The ZC sequence of length  $N$  is defined in Equation 2.17, where  $R$  is the root index (relatively prime to  $N$ ),  $n$  is the sample.

$$x_u(n) = \exp\left(-j\frac{\pi Rn(n+1)}{N}\right), \quad 0 \leq n < N \quad (2.17)$$

### 2.9.2 QPSK Modulation

Quadrature Phase Shift Keying (QPSK) is a spectrally efficient modulation scheme that encodes two bits per symbol by modulating the phase of the carrier among four distinct values. In this project, a pseudorandom QPSK sequence is used as the data payload following the preamble. The sequence is designed to occupy the full system bandwidth, ensuring uniform spectral content and enabling accurate LS channel estimation.

## 2.10 Calibration Trade-offs and Practical Considerations

The calibration of a MIMO system involves several fundamental trade-offs that must be carefully balanced to achieve reliable and accurate results. Key considerations include bandwidth, resolution, measurement environment, positioning accuracy, and system complexity. Increasing bandwidth improves temporal resolution and the ability to distinguish closely spaced multipath components, but also increases data rates, processing requirements, and the risk of hardware limitations such as buffer overflows or data loss. The choice of measurement environment, such as using a UAV for flexible transmitter placement versus a fixed elevated site, affects the ability to isolate the LoS component and minimize multipath fading. Positioning accuracy, typically achieved via RTK GNSS or total station systems, directly impacts phase calibration and the reliability of distance compensation; centimeter-level accuracy is often required to avoid significant phase errors. Finally, practical constraints such as SDR memory, computational resources, and measurement duration must be considered to ensure robust and repeatable calibration. These trade-offs are summarized and discussed in the following subsections.

### 2.10.1 Bandwidth

The bandwidth of the system is a fundamental parameter that directly impacts the temporal resolution and accuracy of the calibration process. A wider bandwidth increases the system's ability to resolve closely spaced multipath components in the CIR, as the temporal resolution is inversely proportional to the bandwidth (Resolution =  $c/f_s$ , see Equation 2.18). This is particularly important in multipath-rich environments, where distinguishing the LoS tap from reflections is essential for accurate calibration.

However, increasing the bandwidth also leads to higher data rates and greater computational and storage demands. In the context of SDR-based measurements, this can result in practical limitations such as buffer overflows, data loss, or discontinuities in the sampled data, especially if the host computer cannot process

or store the incoming data stream in real time. Such discontinuities can corrupt measurements and reduce the reliability of the calibration.

To address these challenges, two main strategies can be considered: (1) reducing the bandwidth to lower the data rate, which unfortunately degrades temporal resolution and may hinder the separation of multipath components; or (2) offloading more processing to post-processing stages, where raw data is stored for later analysis. The latter approach preserves measurement fidelity but is limited by the available memory and storage capacity of the host system. Recording several minutes of high-bandwidth data can quickly exhaust system resources, necessitating careful planning of measurement duration and data management. Alternatively, reducing the data type (e.g., from 16-bit to 8-bit) can decrease storage and processing requirements, but this comes at the cost of loss of dynamic range and sample resolution.

In summary, the choice of bandwidth involves a trade-off between temporal resolution and practical system constraints. Optimal calibration requires selecting a bandwidth that is wide enough to resolve relevant channel features, while ensuring that the SDR and host system can reliably acquire and process the data without interruption.

### 2.10.2 Resolution

The temporal resolution of a channel measurement system determines the minimum path length difference that can be resolved between two multipath components. This resolution is fundamentally limited by the system's sampling rate or, equivalently, its bandwidth. As shown in Equation 2.18, the resolution in meters is given by the ratio of the speed of light  $c$  to the system bandwidth  $f_s$ .

$$\text{Resolution} = \frac{c}{f_s} \quad (2.18)$$

This means that two multipath components must be separated by at least this distance to appear as distinct taps in the CIR. In practice, the finite bandwidth imposes a sinc-shaped impulse response for each tap, causing energy from closely spaced paths to overlap, a phenomenon known as "sidelobe leakage" or "bleeding," which further limits the ability to distinguish between taps (see section 2.4). This effect can be mitigated by high-resolution spectral estimation methods such as APES, which offer improved resolution over conventional Fourier techniques. However, these methods require precise knowledge of the location of the LoS taps, typically obtained from the positioning system.

High resolution is particularly important for accurately identifying the LoS component in environments with significant multipath. For example, using a drone to position the transmitter allows for flexible placement and ensures that the LoS path is sufficiently separated from reflections, provided the excess path length of the reflected components exceeds the system resolution. This capability is critical for reliable calibration, as it enables unambiguous identification and compensation of the LoS tap, minimizing errors due to multipath overlap.

### 2.10.3 Distance

The distance between the transmitter and the receiver array plays a crucial role in the trade-off between fading and the uniformity of the DoA across array elements. When the transmitter is positioned far from the array, the incoming wavefront approximates a plane wave, resulting in nearly identical DoA for all antenna elements. This simplifies calibration, as the antenna gain pattern can be considered constant across the array. However, increasing the distance also reduces the attenuation difference between the LoS and reflected paths, making their received power levels more similar. This increases the likelihood of deep fades due to destructive interference, as even small changes in the environment or position can cause significant fluctuations in the received signal strength.

Conversely, placing the transmitter closer to the array increases the angular spread of the incoming wavefront, causing the DoA to vary more significantly between elements. While this reduces the risk of deep fades, since the LoS path remains dominant over reflections, it complicates calibration, as the direction-dependent antenna gain must be accurately characterized for each element. Therefore, the optimal distance must balance the need for a uniform DoA (favoring larger distances) against the desire to minimize fading (favoring shorter distances), depending on the specific calibration requirements and measurement environment. See Figure 2.10.1 for an illustration of the DoA variation across an array as a function of distance.

### 2.10.4 Measurement Environments

The choice of measurement environment has a significant impact on the quality and reliability of MIMO system calibration. Two primary approaches are commonly considered: using a UAV (drone) to position the transmitter, or leveraging natural or man-made elevations (such as hills, rooftops, or towers) to achieve favorable propagation conditions.

Employing a UAV provides maximum flexibility in transmitter placement, enabling precise control over position, altitude, and orientation. This mobility allows for comprehensive sampling of the antenna array's spatial response, facilitates the mapping of direction-dependent gain and phase patterns, and enables measurements at various distances and angles. UAVs are particularly advantageous for outdoor environments where access to elevated structures is limited or where a wide range of measurement geometries is required. However, UAV-based measurements require careful consideration of flight regulations, battery limitations, payload capacity, and the integration of high-precision positioning systems (such as RTK GNSS) to ensure accurate synchronization between position and channel data.

Alternatively, placing the receiver array on a natural or artificial elevation—such as a hill, cliff, or tall building—can mitigate multipath effects by reducing ground and surrounding reflections. In such scenarios, the transmitter can be positioned at ground level or at a fixed location, with the elevation providing a clear line-of-sight (LoS) path and minimizing the influence of nearby reflectors. This approach is particularly useful when UAV operation is impractical or when regulatory constraints limit aerial measurements. However, the lack of transmitter mobility

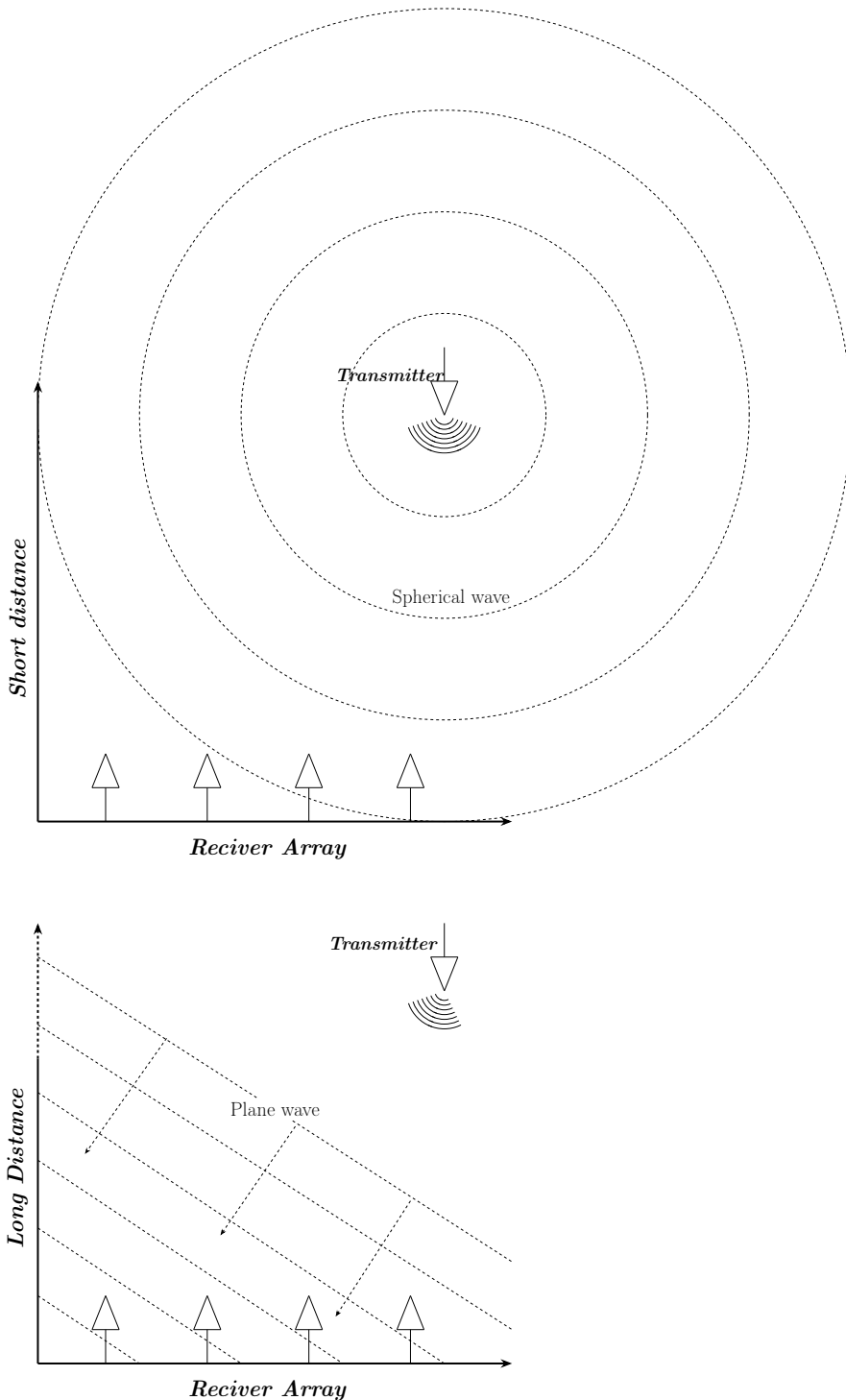


**Figure 2.10.1:** Illustration of how the direction of arrival of the incoming signal varies for each antenna element when the transmitter is positioned close to the receiver array. In this near-field scenario, each element observes a different DoA due to the curvature of the wavefront, resulting in element-specific gain  $G(r)$ . As the transmitter is moved farther away, the wavefront approaches planar, resulting in nearly identical DoA for all elements and simplifying the calibration process, since the antenna gain can be treated as uniform across the array.

restricts the range of measurement geometries and may limit the ability to fully

characterize the antenna array's spatial response.

### 2.10.5 Positioning

Accurate positioning of the transmitter is critical for reliable MIMO system calibration, as even small errors can introduce significant phase and amplitude uncertainties (see Figure 2.7.1). Two primary high-precision positioning technologies are commonly considered: RTK GNSS and total station systems. Both positioning methods have been effectively utilized in UAV-based radio measurement scenarios [18, 19].

**RTK GNSS** provides real-time, centimeter-level accuracy (typically 1–2 cm) by using carrier-phase measurements and differential corrections from a fixed reference station. RTK is highly portable, can be integrated with UAVs for flexible measurement campaigns, and enables continuous position tracking during dynamic measurements. However, its accuracy can degrade in environments with poor satellite visibility (e.g., urban canyons, dense foliage), and it is susceptible to multipath effects and atmospheric disturbances.

**Total station** systems, which use laser or optical measurements to determine positions relative to a fixed reference point, can achieve sub-centimeter or even millimeter-level accuracy (down to 1 mm under optimal conditions). This makes them ideal for applications requiring the highest possible precision. However, total stations are less portable, require line-of-sight between the instrument and the target, and involve more complex and time-consuming setup procedures. They are generally better suited for static, controlled environments rather than dynamic or large-scale outdoor measurements.

In summary, RTK GNSS offers a practical balance between accuracy, portability, and ease of integration, especially for UAV-based or mobile measurements—while total stations provide superior accuracy at the expense of flexibility and setup time. The choice between these systems depends on the specific calibration requirements, measurement environment, logistical constraints of the experiment and the availability of equipment.

## 2.11 Summary

This chapter has established the theoretical foundation for MIMO system calibration. It introduced the principles of calibration, emphasizing the need to compensate for hardware-induced phase and amplitude offsets in antenna arrays. The chapter described the LPDA antenna and its direction-dependent gain, the modeling of the wireless channel as a linear time-invariant system, and the impact of multipath fading. Channel estimation techniques, including least squares and high-resolution methods, were presented as essential tools for extracting the channel impulse response and identifying the line-of-sight component. The importance of precise transmitter positioning, achievable with RTK GNSS, was highlighted for accurate phase compensation. Practical considerations and trade-offs—such as bandwidth, resolution, measurement environment, and positioning accuracy, were discussed to guide effective calibration in real-world scenarios.

---

CHAPTER  
**THREE**

---

METHODS

### 3.1 Introduction

This chapter presents the methodology developed for calibration of a MIMO antenna array, addressing both controlled (anechoic chamber) and real-world (outdoor) measurement scenarios. The methods focus on precise estimation and compensation of phase and amplitude differences between antenna elements, leveraging a combination of hardware and software components.

The approach integrates Software Defined Radios (SDRs), GNSS-based positioning, and signal processing algorithms to enable channel estimation and calibration. Key aspects covered include transmitted signal design, receiver processing, measurement setups, calibration procedures, and data analysis. Due to practical constraints, a drone-based platform was not implemented. Instead, a portable, man-carried system was developed for outdoor measurements.

By systematically addressing each stage of the calibration process, this methodology aims to deliver reproducible and high-precision results. Further technical implementation details can be found in the appendix.

### 3.2 System Overview

This section provides a high-level overview of the complete calibration system, highlighting the integration of hardware and software components. The system is designed for flexibility, supporting both controlled laboratory (anechoic chamber) and real-world (outdoor) measurement scenarios. Key subsystems include SDR-based transceivers, custom antenna arrays, high-precision GNSS positioning, and a modular software framework for signal generation, acquisition, and processing. The following subsections detail the hardware and software architectures that enable accurate and reproducible MIMO array calibration.

#### 3.2.1 Hardware Overview

The hardware platform for the calibration system is designed to support both controlled (anechoic chamber) and real-world (outdoor) measurement environments,

as motivated by the theoretical requirements outlined in chapter 2. The main hardware components are:

- **Software Defined Radios (SDRs):** Universal Software Radio Peripheral (USRP) B210 devices are used for both transmission and reception. These SDRs provide flexible, high-bandwidth RF front-ends and allow for rapid reconfiguration of system parameters such as frequency, bandwidth, and modulation scheme (see section 2.8). The USRP B210 supports MIMO operation (2 outputs and inputs) and is controlled via USB 3.0 by a host computer.
- **Antenna Arrays:** The receiver employs a custom  $3 \times 1$  LPDA array, while the transmitter uses a single LPDA antenna (outdoor). The LPDA design offers wideband operation and stable directional characteristics, as described in subsection 2.3.2. For outdoor measurements, the array is modified to include a GNSS antenna for precise position tracking.
- **GNSS Positioning System:** High-precision positioning is achieved using u-blox ZED-F9P GNSS receivers, which support RTK corrections for centimeter-level accuracy (subsection 2.7.1). Accurate position information is essential for compensating distance-dependent phase shifts and for mapping the direction of arrival during calibration.
- **Host Computers:** In the anechoic chamber, both Tx and Rx USRPs are controlled by a windows PC running MATLAB. For outdoor measurements, a Raspberry Pi 4B is used as the portable host for the Tx USRP, while the Rx USRP remains connected to a laptop for real-time data acquisition.
- **Power Supply:** The outdoor system is powered by a portable EcoFlow River EF4 battery, providing sufficient capacity for extended field measurements and standard AC power (230 V).
- **Mechanical Turntable and Motor:** For anechoic chamber experiments, a Newport XPS-Q motorized turntable is used to precisely rotate the Rx antenna array, enabling controlled variation of the angle of arrival.

This hardware configuration ensures the flexibility and precision required for MIMO calibration. The selection of SDRs, antennas, and high-accuracy GNSS positioning directly addresses the theoretical challenges of phase and amplitude calibration, antenna pattern characterization, and synchronization discussed in chapter 2. The system design also represents a compromise between ideal theoretical requirements and the constraints imposed by available hardware, balancing measurement accuracy, portability, and practical deployment.

### 3.2.2 Software Overview

The software framework for the calibration system is designed to provide flexible control, real-time and post processing , and robust data analysis across both laboratory and field environments. The main software components are:

- **MATLAB:** Used extensively for controlling the USRP SDRs, signal generation, data acquisition, and post-processing. MATLAB scripts implement the signal processing algorithms for frame detection, synchronization, channel estimation, and calibration. In the anechoic chamber, MATLAB also interfaces with the motorized turntable for automated angle control.
- **GNU Radio:** Deployed on the Raspberry Pi 4B for outdoor measurements, GNU Radio provides a flexible, open-source platform for real-time SDR control and signal transmission. Custom GNU Radio flowgraphs are used to transmit the calibration signals from the USRP B210.
- **u-center:** Used for configuring and monitoring the u-blox ZED-F9P GNSS receivers. On the Tx side, u-center is primarily used for initial setup. On the Rx side, it is also used for real-time position monitoring and logging during measurements.
- **RTKLIB:** This open-source software suite is used for processing GNSS data and applying RTK corrections to achieve centimeter-level positioning accuracy.
- **Custom Scripts:** Additional Python and shell scripts are used for automating data collection, timestamping, and managing communication between the GNSS receivers and host computers. These scripts ensure that all measurement data can accurately be synchronized and logged for subsequent analysis.

This integrated software environment enables control of the measurement process, supports the signal processing techniques, and ensures that all hardware components operate in a coordinated and reproducible manner.

### 3.3 Signal Processing Pipeline

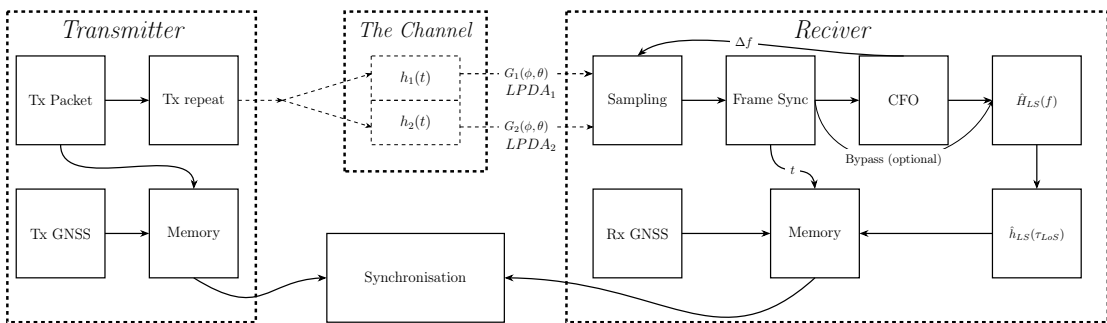


**Figure 3.3.1:** The signal processing pipeline for the MIMO calibration system. The Tx SDR continuously transmits a packet consisting of a preamble and a QPSK sequence, which is sampled by the Rx SDR. The received signal undergoes frame synchronization, CFO estimation, and channel estimation to extract the LoS tap. The LoS tap is then timestamped and stored for further analysis. The GNSS receivers provide position data for both Tx and Rx, enabling accurate distance compensation and calibration.

### 3.3.1 Transmitted Signal Design

The design of the transmitted signal is critical for enabling accurate synchronization, channel estimation, and calibration of the MIMO system. In this work, each transmitted packet consists of two main components: a preamble and a data payload.

Preamble (Zadoff-Chu)	QPSK
-----------------------	------

**Figure 3.3.2:** The transmitted packet consist of a preamble (Zadoff-Chu sequence repeated twice  $139 \cdot 2$  symbols) and a pseudo-random QPSK sequence (1000 symbols). Only one sample per symbol is used in the transmission, resulting in a fully utilized bandwidth.

The preamble is constructed using a ZC sequence, chosen for its ideal autocorrelation properties and robustness to frequency offset, as discussed in subsection 2.9.1. This sequence enables reliable frame detection and precise timing synchronization at the receiver. The ZC preamble is repeated twice, primarily to enable CFO estimation.

Following the preamble, the data payload consists of a pseudo-random QPSK sequence. This sequence is designed to fully occupy the available bandwidth, ensuring a flat spectral profile and enabling (LS) channel estimation, as described in subsection 2.9.2 and subsection 2.4.1. The use of a pseudo-random sequence minimizes spectral peaks and reduces the risk of bias in the channel estimation process.

Each packet is transmitted continuously and at a fixed rate, allowing the receiver to capture multiple packets for improved reliability. Only one sample per symbol is used in the transmission, maximizing bandwidth utilization and temporal resolution. The overall packet structure is illustrated in Figure 3.3.2.

This signal design ensures that the system can achieve synchronization, channel estimation and directly addresses the theoretical requirements outlined in chapter 2.

### 3.3.2 Receiver Processing

The receiver processing pipeline is designed to extract channel information from the received signal, enabling the calibration of the MIMO system. This process involves several key steps: frame detection, synchronization, channel estimation, and timestamping, each of which addresses specific theoretical requirements discussed in chapter 2.

**Frame Detection and Synchronization:** Upon reception, the sampled signal is first processed to detect the start of each transmitted packet. This is achieved by correlating the received signal with the known ZC preamble, leveraging its ideal autocorrelation properties for robust frame detection even in the presence of noise and frequency offsets (see subsection 2.9.1). Once the preamble is detected, the receiver extracts the corresponding packet and aligns it in time, facilitating synchronization for subsequent processing. The technical implementation is shown in appendix F2.1.

**Carrier Frequency Offset Estimation:** CFO arises from small frequency mismatches between the transmitter and receiver oscillators, resulting in a time-varying phase rotation of the received signal (see subsection 2.8.1). To address this, the repeated ZC preamble in each packet is used to estimate the CFO. The estimated offset is then compensated by digitally re-rotating the received samples, preventing distortion in the subsequent channel estimation.

In practice, CFO estimation and correction is disabled during measurements to reduce computational load and enable higher sampling rates. This is feasible because the SDRs exhibit very low frequency offset (2 ppm, see Table 2.8.1) and share the same oscillators for both RF inputs (equal phase drift), making CFO correction unnecessary in most cases. Nevertheless, the CFO estimation and compensation algorithm remains implemented in the processing chain to ensure robustness against any unexpected frequency drift if needed in the future. The algorithm used is described in [16].

**Channel Estimation:** After a packet is found, the receiver performs channel estimation to characterize the propagation environment. The LS estimator is applied in the frequency domain by dividing the received spectrum by the known transmitted spectrum, yielding the  $\hat{H}_{LS}(f)$  as described in subsection 2.4.1. The CFR is then transformed to the time domain using an IFFT or APES with ten times increased resolution, resulting in the  $\hat{h}_{LS}(t)$ . The LoS tap is identified, typically as the strongest and earliest tap, and isolated for calibration (found by computing the peak of the estimated CIR).

**Timestamping and Data Logging:** Each detected packet and its corresponding channel estimate are timestamped using the host computer’s system clock and the SDR’s internal timestamp. These timestamps are crucial for synchronizing the channel measurements with the GNSS-based position data from both the transmitter and receiver. Accurate synchronization enables precise compensation for distance-dependent phase and amplitude variations, as well as mapping of the DoA for each measurement.

**Summary:** This receiver processing chain ensures that the extracted channel data is both temporally and spatially aligned, providing a reliable basis for subsequent calibration and data analysis. By systematically addressing synchronization, frequency offset, and channel estimation, the methodology directly supports the theoretical requirements. The processing chain does have minor practical differences between the anechoic chamber and outdoor setups, which are detailed in section 3.4.

## 3.4 Measurement Setups

This section describes the practical implementation of the measurement setups used for both the anechoic chamber and outdoor experiments. It outlines the specific hardware arrangements, procedures, and adaptations required for each environment, ensuring that the calibration methodology can be accurately and reproducibly applied in both controlled and real-world scenarios.

### 3.4.1 Anechoic Chamber Setup

The anechoic chamber setup provides a controlled environment for validating the calibration methodology and theoretical models without the influence of external interference or multipath reflections. The chamber is lined with radio-frequency absorbing materials, ensuring that only the direct LoS path between the transmitter and receiver is present, as discussed in section 2.6.

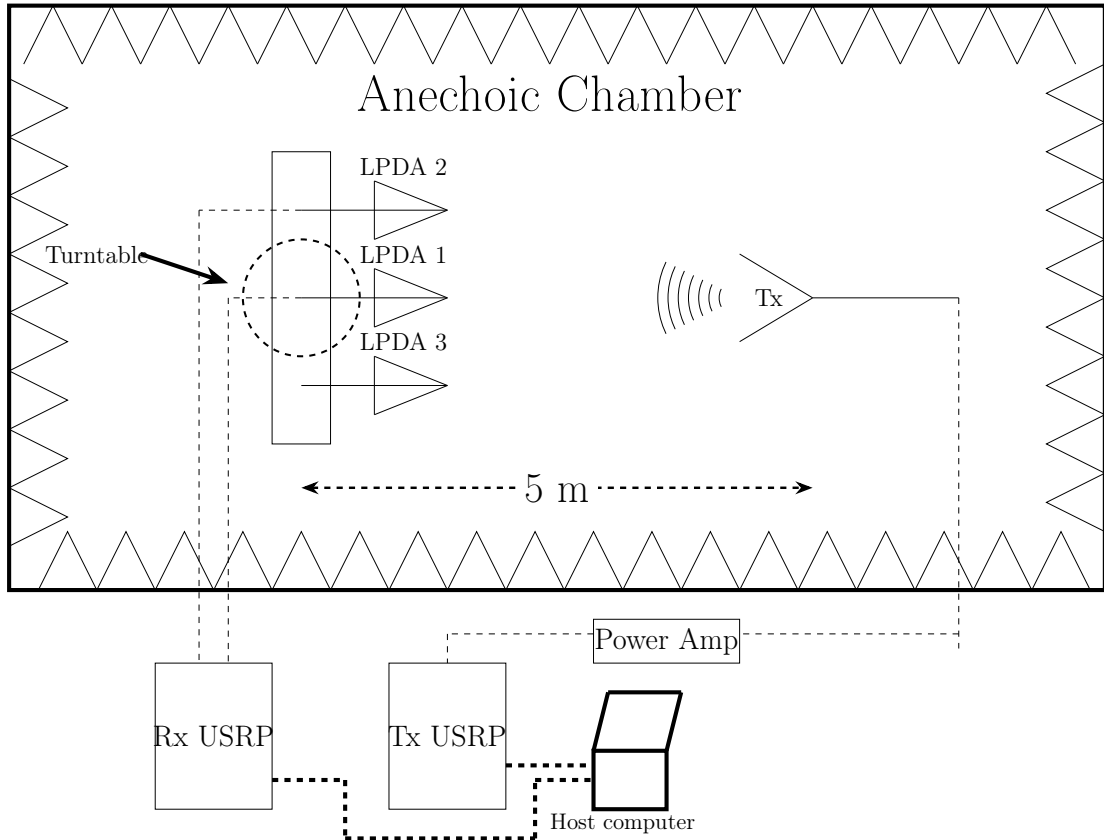


**Figure 3.4.1:** The anechoic chamber system. The system consists of two USRP B210s, a power amplifier, and a custom  $3 \times 1$  LPDA antenna array, where only LPDA 1 and LPDA 2 are used for measurements. The system is controlled by a PC running MATLAB, which manages the USRPs and the motor of the turntable.

The measurement system consists of two USRP B210 SDRs, one acting as the transmitter and the other as the receiver, connected to a host computer running MATLAB for real-time control and data acquisition (sample rate of 1 MHz). The receiver employs a custom  $3 \times 1$  LPDA antenna array (see Figure 3.4.2), while the transmitter uses a single antenna. The Rx array is mounted on a Newport XPS-Q motorized turntable, which is controlled via MATLAB to enable precise and automated rotation over a range of angles. This allows for systematic measurement of the phase and amplitude response as a function of the DoA.



**Figure 3.4.2:** Antenna array setup in the anechoic chamber. The custom  $3 \times 1$  LPDA array is mounted on a motorized turntable, enabling precise and automated rotation for systematic measurement of phase and amplitude response as a function of angle of arrival.

During each measurement, the Tx continuously transmits the calibration packet, while the Rx samples the incoming signal and processes it to compute the  $\hat{h}_{LS}(t)$  and isolate  $\hat{h}_{LS}(\tau_{LoS})$  in realtime. The turntable is continuously rotated at a fixed speed ( $-90^\circ$  to  $90^\circ$ ), and records the relevant channel data. In post-processing, the sampled LoS taps are synchronized with the turntable position. The correction for phase and amplitude is applied based on the known distance between the Tx and Rx antennas, as described in subsection 2.4.3. This procedure enables detailed mapping of the array response and facilitates the extraction of phase and amplitude offsets between antenna elements.

The anechoic chamber setup is essential for establishing a baseline calibration and for characterizing the intrinsic properties of the antenna array and measurement system, free from environmental uncertainties. The results obtained in this environment serve as a reference for subsequent outdoor measurements and can be seen in section 4.2.

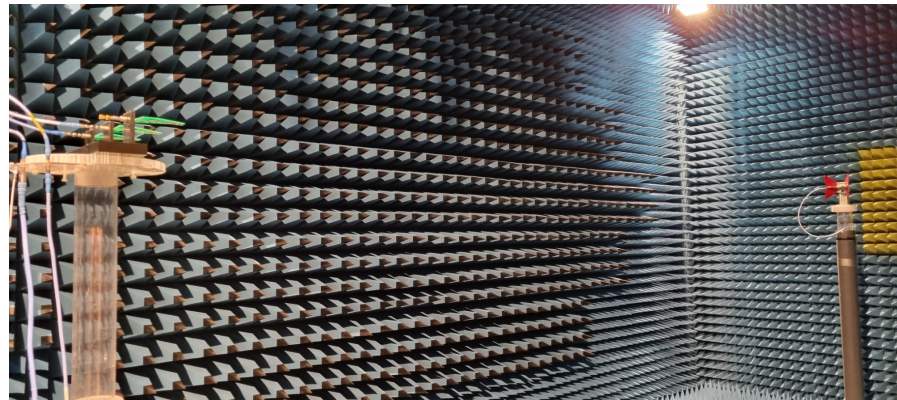


**Figure 3.4.3:** Anechoic chamber measurement setup. The Rx antenna array is mounted on a motorized turntable for precise angular control, while the Tx antenna remains fixed at a known distance. This configuration enables systematic measurement of phase and amplitude variations as a function of the angle of arrival, providing a controlled environment for calibration and array characterization.

### 3.4.2 Outdoor Measurement Setup

The outdoor measurement setup extends the calibration methodology to real-world environments, introducing additional challenges such as multipath propagation, environmental variability, and the need for precise positioning. To address these, the system is adapted from the anechoic chamber configuration with several key modifications to ensure portability, robustness, and high-precision data collection.

The core hardware remains the same, utilizing USRP B210 SDRs for both transmission and reception. However, for outdoor use, the transmitter is made portable by mounting the USRP and its host computer, a Raspberry Pi 4B, on a lightweight platform, powered by a portable EcoFlow River EF4 battery. The receiver array, consisting of a custom  $3 \times 1$  LPDA antenna array (same as anechoic chamber with modification), is positioned at an elevated location (such as a hilltop, see Figure 3.4.4a) to maximize the LoS conditions and minimize ground reflections, as motivated by the theoretical considerations in subsection 2.4.4.



**Figure 3.4.4:** Outdoor system setup. (a) The Rx array is mounted on a height with a GNSS receiver antenna. (b) The Tx is mounted on a plate with a GNSS receiver antenna and a Raspberry Pi for portability.

A critical addition to the outdoor setup is the integration of high-precision GNSS positioning using u-blox ZED-F9P receivers with RTK corrections. Both the Tx and Rx are equipped with GNSS antennas, enabling theoretical centimeter-level accuracy in position tracking (with RTK). This is essential for compensating distance-dependent phase shifts and for mapping the DoA during calibration. The GNSS data is synchronized with the SDR measurements using timestamps, ensuring accurate alignment between spatial and channel information.

During measurements, the Tx is moved along a semi-predefined path (in a snake-like pattern) around the static Rx array, as illustrated in Figure 3.4.5. The movement and positions are continuously recorded by the GNSS system. The receiver samples the incoming signal and performs real-time frame detection and synchronization. Subsequently, the raw packet data and corresponding timestamps are logged for post-processing. This approach allows for flexible sampling of the spatial response of the antenna array and supports detailed mapping of phase and amplitude offsets under realistic propagation conditions. Post-processing enables an increased effective bandwidth of 4 GHz, which in turn provides higher resolution (approximately 75 m). This comes at the cost of increased computational time and significant memory consumption.

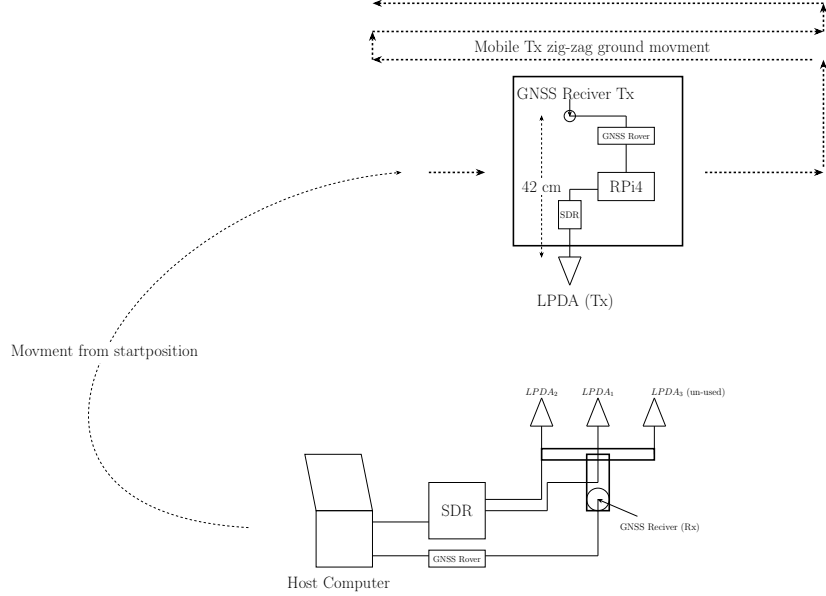


**Figure 3.4.5:** An illustration of the measurement setup and approximately snake-like movement of the Tx antenna.

Power considerations are addressed by using a high-capacity battery for the Tx system, enabling several hours of continuous operation in the field. The overall design emphasizes portability, ease of deployment, and resilience to environmental factors, making it suitable for a wide range of outdoor calibration scenarios, but it is not suitable as a UAV-mounted system due to the weight of battery and formfactor of the system.

In summary, the outdoor measurement setup integrates portable SDR hardware, high-precision GNSS positioning with RTK corrections, and data acquisition to enable calibration and characterization of MIMO antenna arrays in realistic environments. This configuration allows for flexible spatial sampling and compensation of distance-dependent effects, addressing key challenges such as multipath propagation and synchronization. While the system successfully worked, the results indicate that further improvements are needed to enhance measurement accuracy and robustness, particularly position alignment. Results are presented in section 4.3.

## 3.5 Calibration and Data Analysis

This section describes the overall calibration and data analysis workflow. It outlines how the measured data is processed to extract phase and amplitude offsets, apply distance compensation, and synchronize with position information. The goal is to ensure that all antenna elements are accurately calibrated for subsequent measurements and analysis.

### 3.5.1 Calibration Procedure

The calibration procedure is designed to accurately determine and compensate for the phase and amplitude offsets between the elements of the MIMO antenna array.

The procedure consists of several key steps, each addressing specific theoretical and practical challenges discussed in chapter 2.

**1. Channel Estimation and LoS Tap Extraction:** After receiving and synchronizing the transmitted packets, the CFR is estimated using the LS method. The CFR is then transformed to the time domain to obtain the CIR. Zero-padding is applied in the frequency domain to the CFR, increasing its resolution in the time domain. The LoS tap, typically the strongest and earliest tap in the CIR and is found as the peak in the impulse response. The LoS tap can also be identified by its known delay, which is determined by the distance between the Tx and Rx antennas, but this is not done in this work.

**2. Distance Compensation:** The phase and amplitude of the LoS tap are influenced by the propagation distance between the transmitter and each receiver element. Using the GNSS-based position data outdoor and turntable information indoor, the geometric distance is calculated for each measurement. Interpolation is used to match GNSS positions with the LoS tap timestamps. The expected free-space response  $\beta$  is then computed and used to compensate the measured LoS tap, removing the deterministic effects of distance and frequency (see Equation 2.12a and Equation 2.12b in subsection 2.4.3).

**3. Offset Extraction:** After distance compensation, the remaining complex value of the LoS tap for each antenna element, denoted as  $G_k(r)\epsilon_k$ , reflects both the antenna's gain pattern  $G(r)_k$  and any hardware-specific phase and amplitude differences  $\epsilon_k$  (see Equation 2.4d and Equation 2.8a). To isolate the relative offsets, one antenna element is selected as a reference (typically the center element). The compensated LoS tap from the other elements is divided by the reference element's value, yielding the relative phase and amplitude offset (see Equation 2.13a):

$$\Delta\epsilon_k = \frac{\epsilon_k}{\epsilon_1}$$

where  $\Delta\epsilon_k$  is the complex ratio between the  $k$ -th element and the reference. The magnitude of  $\Delta\epsilon_k$  gives the amplitude offset, and its angle gives the phase offset. This approach assumes that all antenna elements receive the signal from nearly the same direction at each measurement point, a reasonable approximation in the far-field (see Figure 2.10.1). While this is not perfectly true in practice, especially in near-field or indoor scenarios, it greatly simplifies the calibration process and is shown to be sufficiently accurate for this work (see section 4.2).

**4. Application of Calibration:** The calculated offsets  $\Delta\epsilon_k$  are saved and used to correct all future measurements or system operations. By applying these corrections, the system ensures that all antenna elements are aligned in phase and amplitude, which is essential for accurate beamforming and spatial signal processing. In practice, this means multiplying each received or transmitted signal by the corresponding complex offset, so that differences between antenna elements are compensated in the signal processing chain.

**5. Summary:** This systematic calibration procedure is applied consistently across both the anechoic chamber and outdoor measurement setups, with minor adaptations to account for environmental differences and testing facilities.

### 3.5.2 Data Post-Processing

Data post-processing plays a crucial role in removing path-specific deterministic amplitude and phase offsets from the raw measurements. By compensating for the known effects of propagation distance and geometry, using precise position data from GNSS or turntable information, post-processing isolates and corrects the deterministic phase and amplitude variations that arise from the specific measurement path. This ensures that the extracted offsets reflect only the intrinsic differences between antenna elements.

**GNSS Correction:** Raw GNSS data is affected by errors from atmospheric effects, satellite geometry, and multipath propagation (see subsection 2.10.5). To achieve the centimeter-level accuracy required for reliable phase calibration (see Figure 2.7.1), RTK corrections are applied using the RTKLIB software and correction data from a "Kartverket" basesattion. This process significantly reduces position uncertainty, which is crucial for distance compensation and phase correction (see Equation 2.12a and Equation 2.12b). The corrected GNSS coordinates are then converted to local Cartesian coordinates (using MATLAB's `latlon2local` function [20]). The relative position of the Rx antenna elements to the Rx GNSS antenna is determined using a compass to measure the array's orientation relative to North (see Figure 3.5.1). The Tx antenna position is approximated by a fixed offset from the Tx GNSS antenna, assuming the Tx always points toward the Rx array. While this introduces some uncertainty, it is theoreticaly precise as long as the orientation is maintained (see discussion in subsection 5.2.2).

**Synchronization:** Accurate synchronization between the channel measurements and the corresponding GNSS position data is critical, especially for outdoor experiments where the transmitter is moving. Each channel estimate is timestamped, while the GNSS receivers independently log position data with their own timestamps. In post-processing, interpolation is used to align the GNSS positions with the channel measurement timestamps, ensuring that each LoS tap is associated with the correct spatial coordinates. This step is crucial for distance compensation, as described in subsection 2.4.3. For indoor measurements, synchronization is achieved using the turntable's fixed speed and programmed start time, which are controlled by the same script as the SDRs, ensuring deterministic alignment.

**Summary:** By applying these post-processing steps, the calibration procedure achieves accuracy and reliability, ensuring that the extracted phase and amplitude corrections are valid for subsequent system operation. This approach directly addresses the theoretical requirements for synchronization, positioning accuracy, and error mitigation outlined in chapter 2. For greter details, see apnedix.

## 3.6 Summary of Parameters

This section summarizes the key parameters and configurations used in both the anechoic chamber and outdoor measurement setups. These tables provide an overview of the most important system specifications, measurement conditions, and hardware/software configurations, allowing for easy comparison and reproducibility of the experiments.

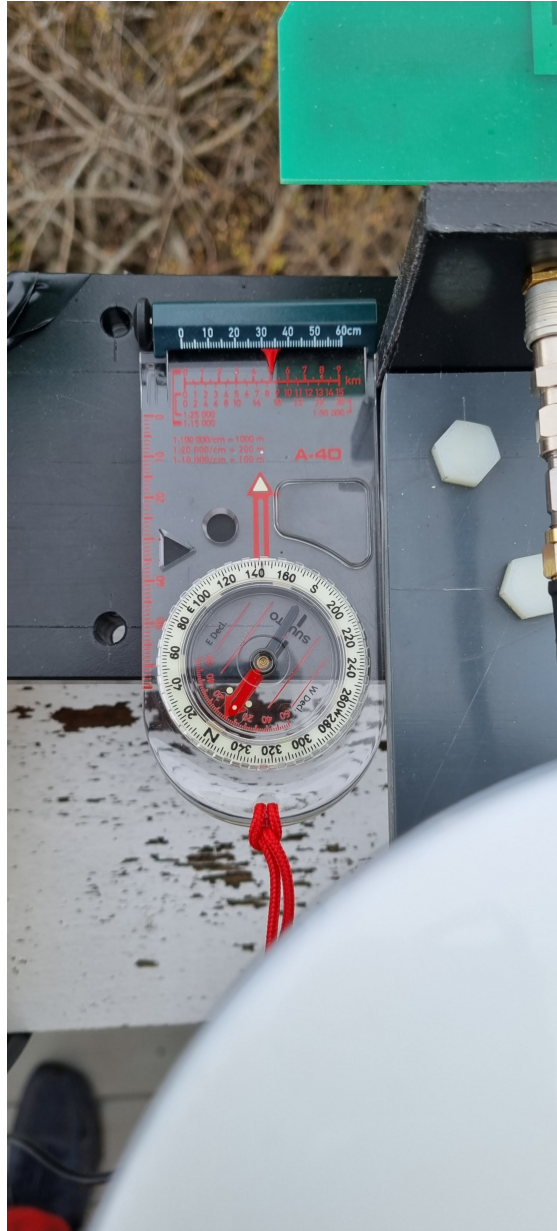


**Figure 3.5.1:** Using a compass to determine the orientation of the Rx antenna array relative to North. This information is crucial for accurately mapping the LPDA elements positions relative to the GNSS, but is not ideal in term of precision.

**Table 3.6.1:** Anechoic Chamber System Parameters (Grouped by Subsystem)

SDR/Hardware Parameters	
SDR Model	USRP B210
Sampling Frequency ( $f_s$ )	1 MHz
Carrier Frequency ( $f_c$ )	1.3, 3, 6 GHz
Tx Antenna	Anechoic Chamber standard antenna
Rx Antenna	3 × 1 LPDA (2 used)
Power Supply	AC Mains
Host Computer	PC (Windows)
Environment/Measurement Parameters	
Measurement Environment	NTNU Anechoic Chamber
Turntable	Newport XPS-Q
Measurement Time	≈ 30 second
Tx–Turntable Distance	≈ 5 m
Software/Control Parameters	
Software Framework	MATLAB
Turntable Control	MATLAB Script
Real-time Signal Processing	Frame Sync, Channel Estimation (FFT)
Post-Processing	Path compensation, DoA mapping
Data Logging	MATLAB, CSV

**Table 3.6.2:** Outdoor System Parameters (Grouped by Subsystem)

SDR/Hardware Parameters	
SDR Model	USRP B210
Sampling Frequency ( $f_s$ )	4 MHz
Carrier Frequency ( $f_c$ )	1.3 GHz
Tx Antenna	LPDA
Rx Antenna	3 × 1 LPDA (2 used)
Power Supply	EcoFlow River EF4 Battery
Host Computer (Tx)	Raspberry Pi 4B
Host Computer (Rx)	PC Laptop
Environment/Measurement Parameters	
Measurement Environment	Outdoor, LoS with minimal reflections
Measurement Time	≈ 12 min
Tx–Rx Distance	Variable (snake-like path)
GNSS Receiver	u-blox ZED-F9P (Tx and Rx)
GNSS Correction Method	RTK (Real-Time Kinematic)
Antenna Array	Modified 3 × 1 LPDA with GNSS antenna
Software/Control Parameters	
Software Framework	MATLAB, GNU Radio, u-center, RTKLIB
Real-time Processing	Frame Sync
Post-Processing	Channel Estimation (FFT), Path compensation
GNSS Data Processing	RTKLIB, MATLAB
Data Logging	MATLAB, CSV, Python scripts

These parameter tables serve as a reference for replicating the measurement

setups and for interpreting the results presented in later chapters. More detailed information about the specific configurations and settings used in the experiments can be found in the appendix.

### 3.7 Summary

This chapter has presented a methodology for calibrating a MIMO antenna array in both controlled (anechoic chamber) and real-world (outdoor) environments. The approach integrates SDR-based transceivers, custom antenna arrays, high-precision GNSS positioning, and a modular software framework for signal generation, acquisition, and processing. Detailed procedures for transmitted signal design, receiver processing, measurement setups, calibration, and data analysis have been described. The methodology emphasizes reproducibility, accuracy, and practical considerations, ensuring that phase and amplitude offsets between antenna elements are estimated. Key system parameters and configurations have been summarized to support repeatability and facilitate future work.

---

CHAPTER  
**FOUR**

---

**RESULTS**

## 4.1 Introduction

This chapter presents the results from the calibration experiments, comparing measurements in both controlled (anechoic chamber) and real-world (outdoor) environments. The findings focus on phase and amplitude offsets after distance correction, with key observations summarized for each scenario.

## 4.2 Anechoic Chamber Results

The anechoic chamber provides a reflection-free environment, allowing for precise validation of the calibration method. Measurements were performed at three frequencies: 1.3 GHz, 3 GHz, and 6 GHz. All results are corrected for the path distance between the Tx and Rx antenna array. The mesuerments were conducted over a 30 seconds periode.

### 4.2.1 Anechoic Chamber Measurements at 1.3 GHz

The antenna pattern results for  $LPDA_1$  and  $LPDA_2$  at 1.3 GHz are shown in Figure 4.2.1. A phase drift due to frequency offset (CFO) is visible.

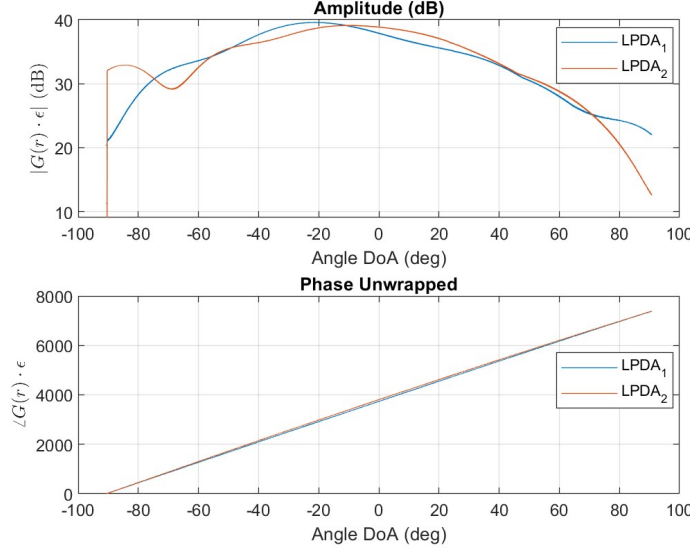


**Figure 4.2.1:** Phase and amplitude of the LoS tap at 1.3 GHz, distance-corrected. This figure shows the measured response for the direct path between the Tx and Rx antennas in the anechoic chamber.

The constant phase and amplitude offset between the two receiver elements is illustrated in Figure 4.2.2. This offset is computed as the ratio of the measured responses:

$$\Delta\epsilon_k = \frac{G(r)_k \epsilon_k}{G(r)_1 \epsilon_1}$$

A clear phase offset is observed, while the amplitude offset remains close to zero.

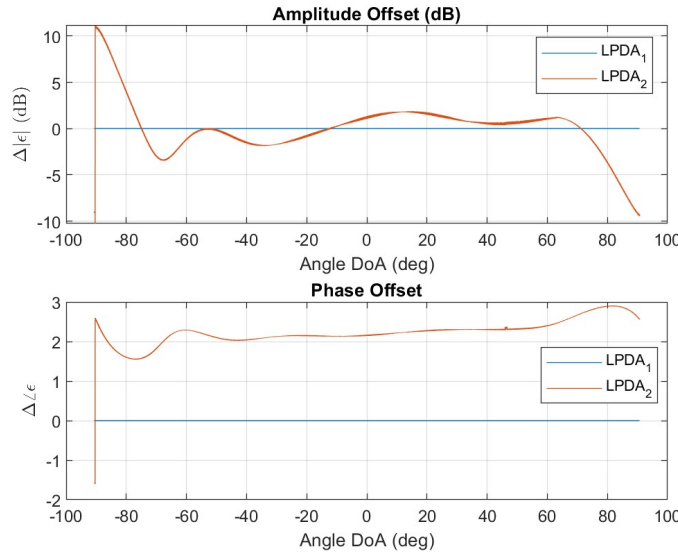


**Figure 4.2.2:** Phase and amplitude offset (ratio) between the two Rx antennas at 1.3 GHz, after distance correction. This figure illustrates the relative calibration offset extracted from the measurement.

### 4.2.2 Anechoic Chamber Measurements at 3 GHz

The antenna pattern results for  $LPDA_1$  and  $LPDA_2$  at 3 GHz are shown in Figure 4.2.3. Similar to the 1.3 GHz measurements, a phase drift due to CFO is visible.

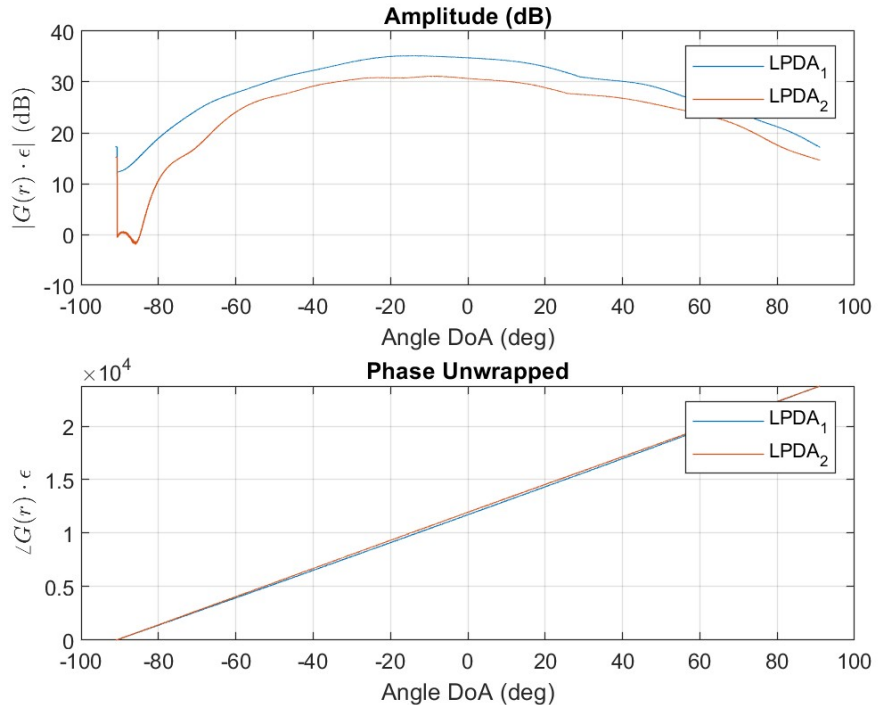


**Figure 4.2.3:** Phase and amplitude of the LoS tap at 3 GHz, distance-corrected. This figure shows the measured response for the direct path between the Tx and Rx antennas in the anechoic chamber.

A consistent phase offset is observed, while the amplitude offset exhibits some variation compared to the 1.3 GHz case.

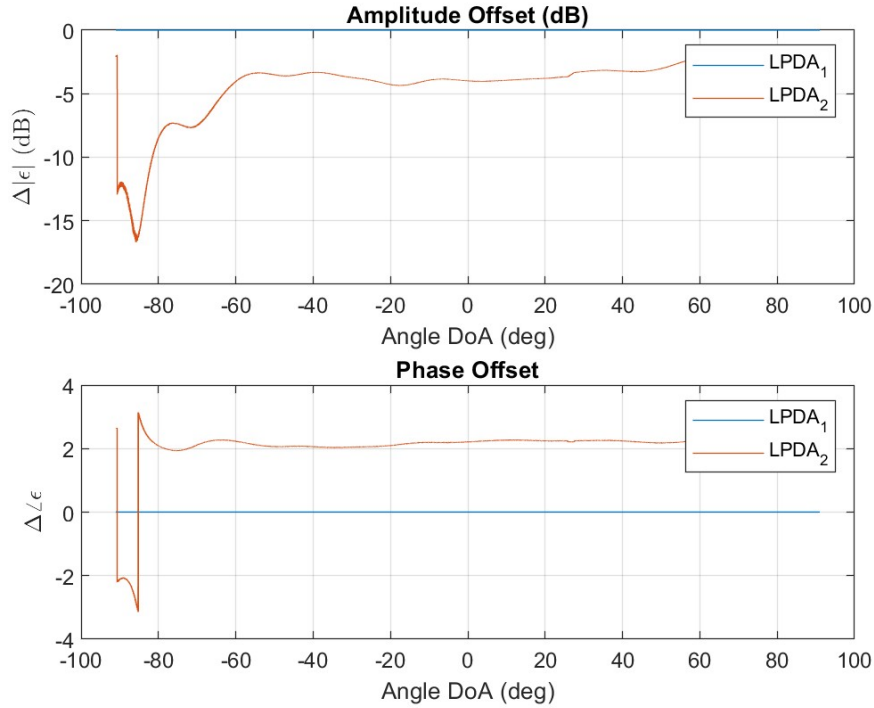


**Figure 4.2.4:** Phase and amplitude offset (ratio) between the two Rx antennas at 3 GHz, after distance correction. This figure illustrates the relative calibration offset extracted from the measurement.

### 4.2.3 Anechoic Chamber Measurements at 6 GHz

The antenna pattern results for  $LPDA_1$  and  $LPDA_2$  at 6 GHz are shown in Figure 4.2.5. The phase drift due to CFO is again visible, similar to the previous frequencies.

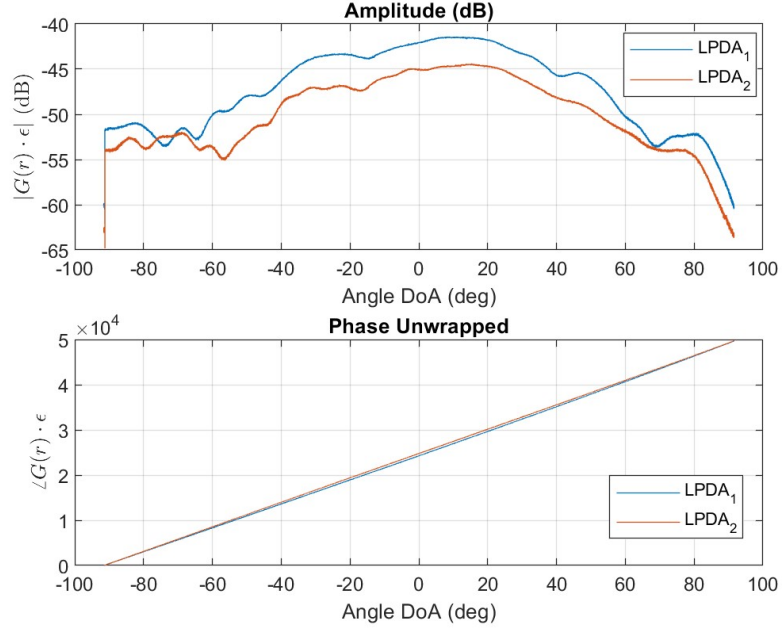


**Figure 4.2.5:** Phase and amplitude of the LoS tap at 6 GHz, distance-corrected. This figure shows the measured response for the direct path between the Tx and Rx antennas in the anechoic chamber.

A clear and stable offset could not be extracted at 6 GHz. The results closely resemble the uncompensated measurements (see Figure B.6), suggesting that the position-based correction was insufficient at this frequency.

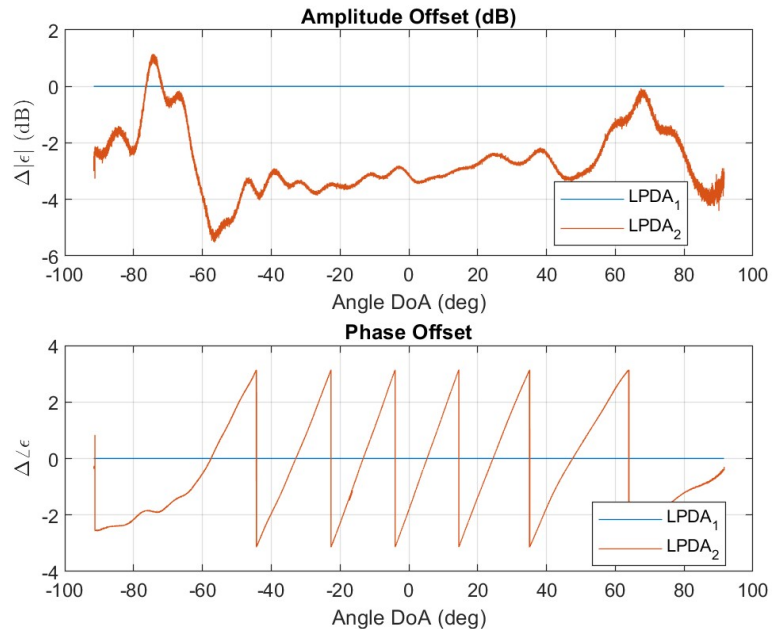


**Figure 4.2.6:** Phase and amplitude offset (ratio) between the two Rx antennas at 6 GHz, after distance correction. This figure illustrates the relative calibration offset extracted from the measurement.

#### 4.2.4 Summary of Anechoic Chamber Results

The measurements show that stable and repeatable phase and amplitude offsets between the receiver antennas are observed at 1.3 GHz and 3 GHz. At 6 GHz, a clear and stable offset could not be extracted, indicating that the position-based correction was insufficient at this frequency. The controlled environment enables accurate distance correction and confirms the calibration approach at lower frequencies. Unfortunately it seems the precision was unsuficient at 6 GHz. A frequency offset between transmitter and receiver is visible as a phase drift, since no frequency synchronization was applied.

### 4.3 Outdoor Results

Outdoor experiments were conducted to assess the performance of the calibration methodology under realistic propagation conditions, including the presence of multipath and GNSS positioning errors. The analysis presented here focuses on measurements at 1.3 GHz, with all data subjected to distance correction using GNSS and RTK techniques.

#### 4.3.1 Calibration Results at 1.3 GHz

Figure 4.3.1 presents the phase and amplitude of the LoS tap for outdoor measurements at 1.3 GHz, after distance correction. The data, collected over a 12-minute interval, exhibit a noticeable phase drift. As the measurements are ordered temporally rather than by DoA, the plot does not reveal additional spatial trends.

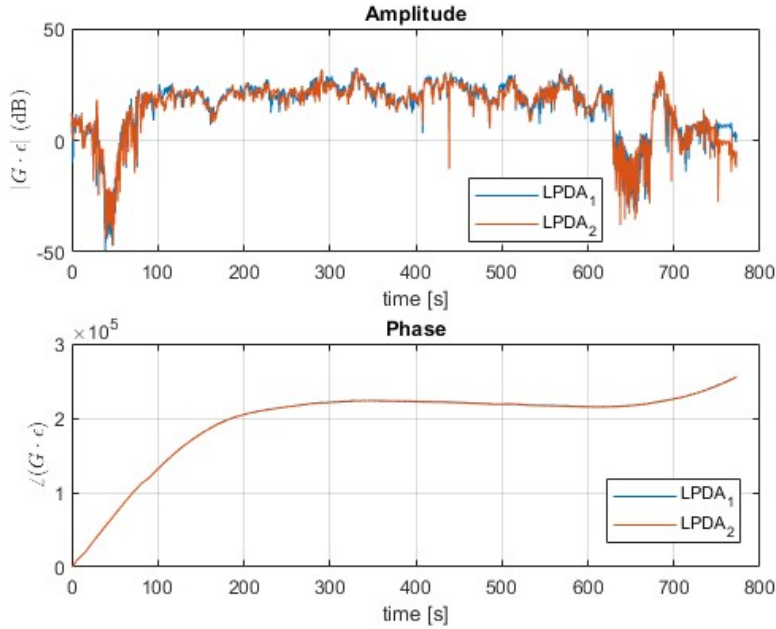


**Figure 4.3.1:** Phase and amplitude of the LoS tap for outdoor measurements at 1.3 GHz, distance-corrected.

Figure 4.3.2 shows the phase and amplitude offset between the two Rx antennas for the same dataset. The phase offset does not exhibit a clear constant value, nor

does it appear entirely random. Instead, the observed pattern is consistent with the expected result from the zig-zag movement of the transmitter, as illustrated in Figure 3.4.5. This suggests that the applied position correction is insufficient to fully compensate for the spatial variation in the measurements.

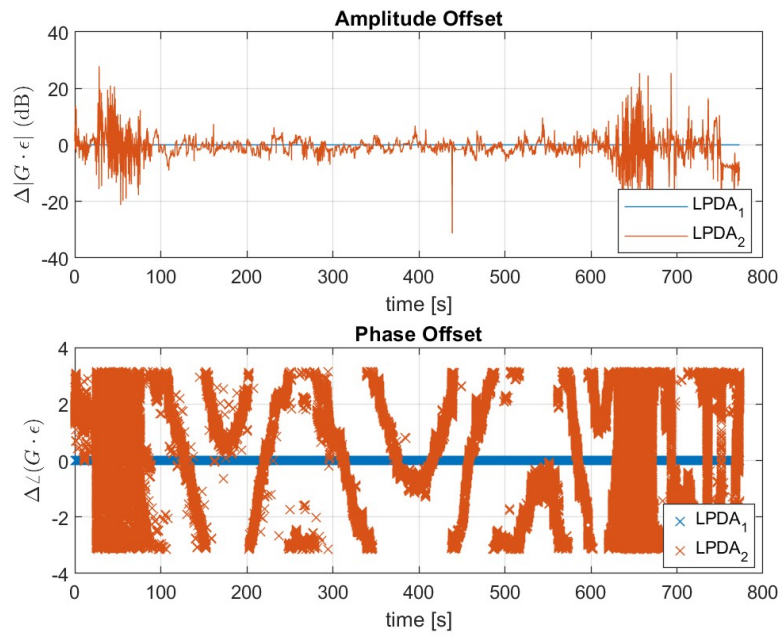


**Figure 4.3.2:** Phase and amplitude offset between the two Rx antennas for outdoor measurements at 1.3 GHz, distance-corrected.

### 4.3.2 GNSS Data and RTK Correction Results

Accurate GNSS data are essential for effective distance compensation in outdoor calibration. Figure 4.3.3 and Figure 4.3.4 compare the raw and RTK-corrected GNSS data, respectively. The application of RTK corrections significantly reduces positional noise, as evidenced by the improved clustering of position estimates.

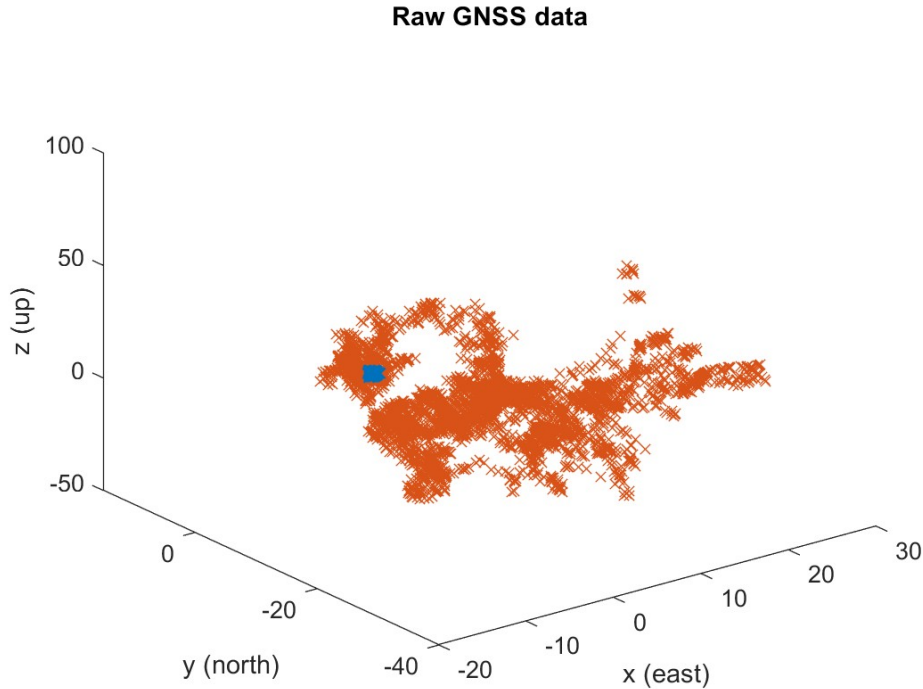


**Figure 4.3.3:** Raw GNSS data from the outdoor measurements (not RTK corrected).

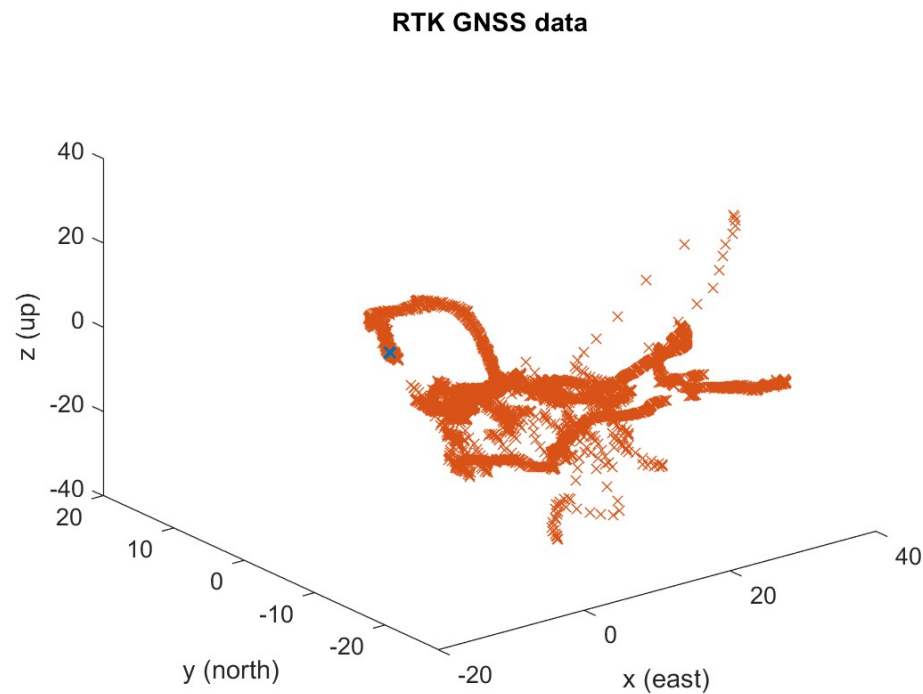


**Figure 4.3.4:** RTK-corrected GNSS data from the outdoor measurements.

A substantial portion of the GNSS data was degraded due to limited satellite visibility, as shown in Figure 4.3.7. When only the highest-quality GNSS data were

selected for distance compensation, as illustrated in Figure 4.3.5. However, even with this selection, the resulting offset (Figure 4.3.6) do not exhibit a consistent or interpretable pattern, indicating that residual errors in position estimation remain a limiting factor.

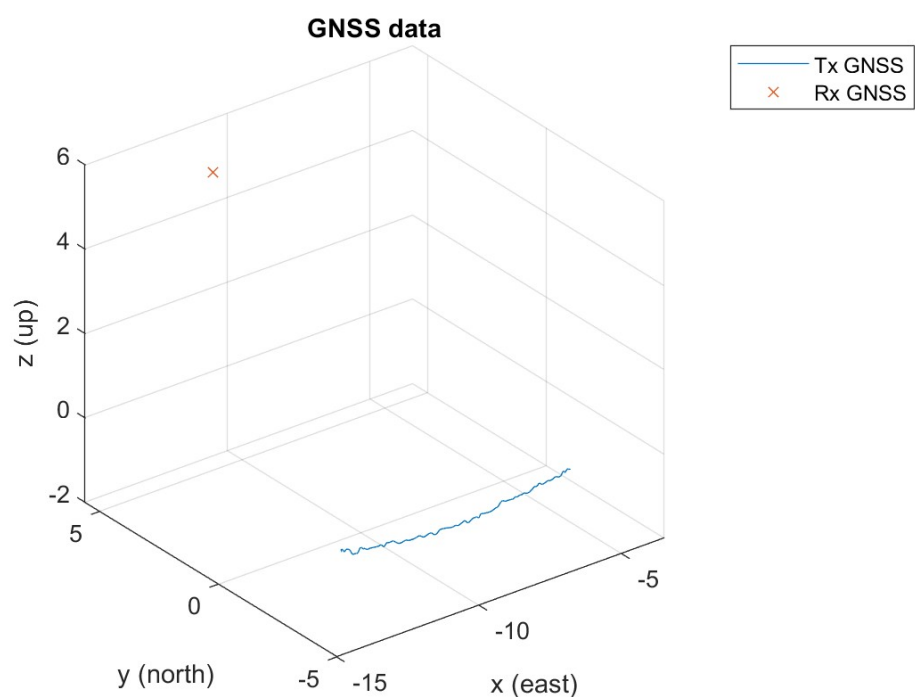


**Figure 4.3.5:** Best RTK-corrected GNSS data from the outdoor measurements.

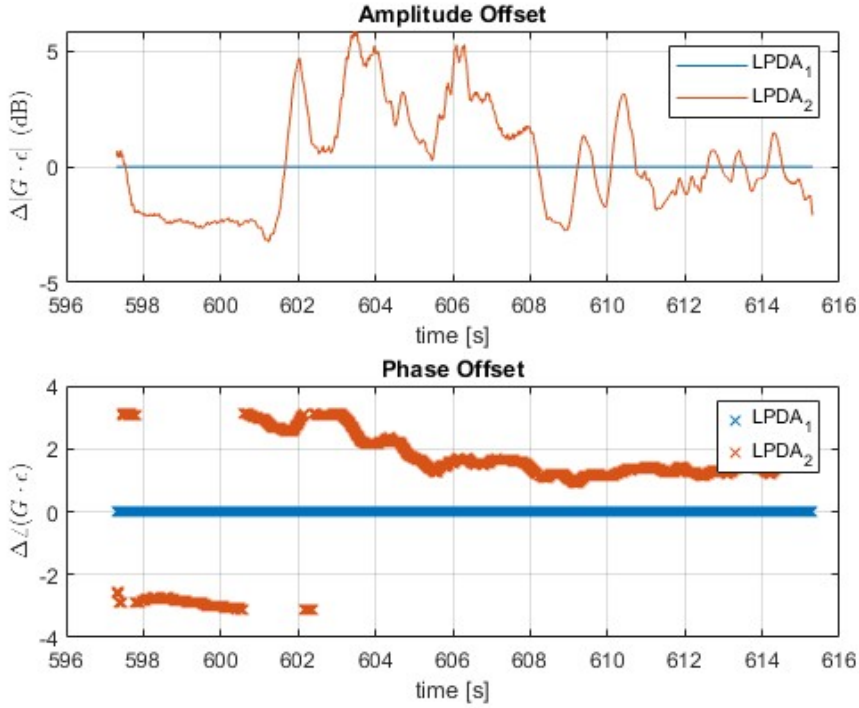


**Figure 4.3.6:** Phase and amplitude offset for outdoor measurements at 1.3 GHz with the best GNSS data.

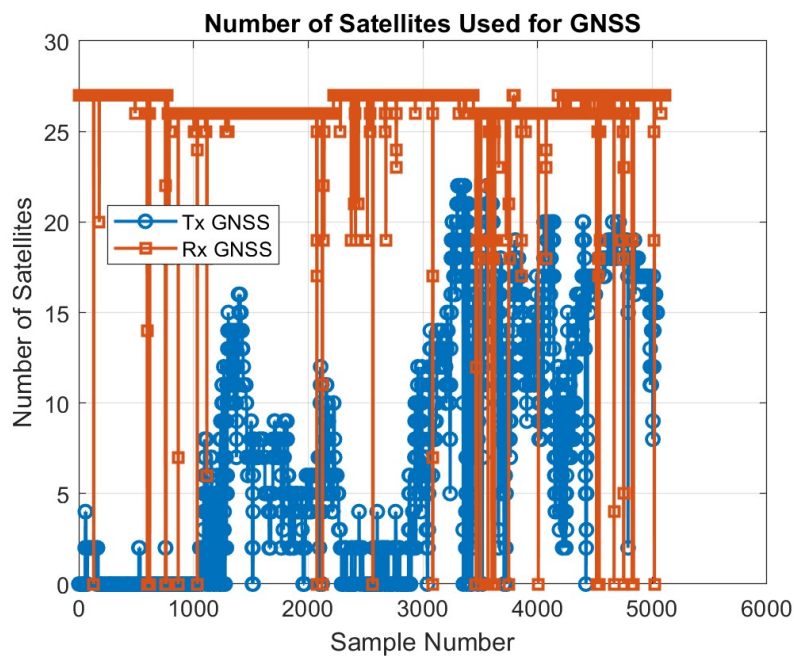


**Figure 4.3.7:** Number of satellites used for GNSS positioning during the outdoor measurements. This figure illustrates the variability in satellite availability at the transmitter, which directly impacts positional accuracy. The receiver was able to use a almost constant number of 25+ satellites, while the transmitter had a variable number of satellites available.

### 4.3.3 Summary of Outdoor Results

The outdoor experiments reveal that the accuracy of the calibration method is highly dependent on the quality of GNSS positioning. Although the methodology remains applicable in outdoor environments, the results exhibit increased uncertainty and variability relative to those obtained in the controlled anechoic chamber. These findings highlight the critical importance of high-quality GNSS data and robust RTK corrections for reliable distance compensation. Furthermore, the channel estimation approach employed appears sufficiently robust, indicating that the measurement setup effectively suppresses significant multipath reflections within the system's resolution limits.

## 4.4 Comparison and Key Findings

- **Anechoic chamber measurements** confirm the method's accuracy and reproducibility under ideal conditions.
- **Outdoor measurements** highlight challenges due to GNSS errors and multipath, but show that calibration is still feasible with RTK corrections.
- **Distance correction and synchronization** are critical for reliable phase and amplitude offset extraction in both environments.

## 4.5 Additional Results

Supplementary figures and raw data, including uncompensated measurements and further parameter sweeps, are provided in Appendix B1 for reference.

## 4.6 Summary

This chapter summarized the results from both anechoic chamber and outdoor experiments. In the controlled environment, stable phase and amplitude offsets were extracted at lower frequencies, confirming the calibration method's effectiveness. At higher frequencies and in outdoor scenarios, increased uncertainty was observed, mainly due to GNSS positioning errors and multipath effects. The results highlight the importance of accurate distance correction and synchronization for reliable calibration, and demonstrate that the method remains applicable with high-quality GNSS data and RTK corrections.



---

CHAPTER  
**FIVE**

---

DISCUSSION

## 5.1 Introduction

This chapter provides a critical and comprehensive analysis of the experimental results, contextualizing their significance, limitations, and broader implications for the calibration of MAMIMO systems. The proposed calibration methodology demonstrated reproducible and accurate estimation of phase and amplitude offsets in controlled environments, while systematic deviations at higher frequencies (notably 6 GHz) underscore the increased sensitivity to wavelength-dependent uncertainties and positioning errors.

The discussion is organized as follows:

- Comparative evaluation of calibration performance across the investigated frequency bands (1.3–6 GHz),
- Assessment of limitations arising from hardware synchronization, initialization artifacts, and environmental uncertainties,
- Analysis of the impact of data processing strategies (real-time versus post-processing) on calibration accuracy and operational efficiency,
- Recommendations for methodological improvements and future research directions.

The chapter integrates both theoretical and practical perspectives relevant to *in-situ* antenna calibration, with a focus on the interplay between system design constraints and achievable calibration fidelity.

## 5.2 Interpretation of Key Results

The experimental findings demonstrate that the proposed calibration approach achieves accuracy and reproducibility in anechoic chamber settings, with stable and consistent phase and amplitude offsets observed between antenna elements. At higher frequencies, particularly 6 GHz, the calibration becomes increasingly sensitive to positioning errors, resulting in systematic phase deviations that are consistent with theoretical predictions regarding wavelength dependence. In outdoor

environments, calibration accuracy is predominantly constrained by the precision and reliability of GNSS-based positioning and the presence of multipath propagation, leading to increased variability and reduced stability in the estimated offsets. These results underscore the critical importance of precise positioning, environmental control, and robust data processing for reliable MIMO calibration, while also demonstrating the method's resilience to certain hardware imperfections, such as common-mode CFO.

### 5.2.1 Anechoic Chamber Results

The results from the anechoic chamber measurements, as presented in section 4.2, demonstrate the effectiveness of the proposed calibration method for accurately estimating the phase and amplitude of the line-of-sight tap in the channel.

Analysis of the amplitude reveals a consistent difference between the two antennas in the Rx array, except at the extreme angles where the direction of arrival approaches  $-90^\circ$  and  $90^\circ$ . These anomalies are primarily attributed to two factors: (1) partial line-of-sight when the turntable is rotated to  $\pm 90^\circ$ , where nearby elements may block the signal path between Tx and Rx, and (2) occasional initialization artifacts from the software-defined radio (SDR), particularly when measurements begin at the  $-90^\circ$  position. Phase measurements also show deviations at these edge angles, reinforcing the influence of both edge effects and SDR initialization.

Across most of the angular range, the phase results show a stable offset between the two Rx antennas, with the exception of measurements at 6 GHz (see Figure 4.2.6). At this higher frequency, the shorter wavelength (5 cm at 6 GHz) increases sensitivity to errors in path distance estimation. The relative positions between the Rx and Tx antennas are not known with sub-centimeter precision, which is sufficient at lower frequencies but leads to significant phase errors at 6 GHz. The observed errors are systematic, indicating that the dominant limitation is the accuracy of the path distance correction algorithm. This interpretation is supported by comparative analysis of results with and without path distance compensation, as shown in appendix B1.

A constant phase drift is also observed in the measurements (Figure 4.2.1, Figure 4.2.3, and Figure 4.2.5), which is attributed to a CFO due to imperfect synchronization between the Tx and Rx USRP oscillators. This drift is expected, as CFO estimation was intentionally disabled during the measurements to reduce processing time. Importantly, this drift is common to both Rx antennas, as they share the same local oscillator, and thus does not affect the relative phase offset between them. As a result, the calibration method remains robust to such synchronization imperfections when estimating relative offsets.

Another notable observation concerns the reconstructed antenna radiation pattern. When the corrected LoS tap is mapped to the DoA of each array element, the resulting pattern appears plausible and consistent with the expected broadside response of the LPDA antennas (see Figure 2.3.3 and Figure 2.3.7). Although no published radiation pattern is available for the specific LPDA antennas used, the measured results align with general LPDA characteristics, supporting the validity of the calibration approach.

Another relevant aspect to discuss is the method used for calculating the offset

ratio  $\Delta\epsilon_k$ . The comparison of LoS taps assumes that the DoA is identical for all array elements, which is an approximation. This assumption introduces errors. However, the severity of these errors depends on the antenna radiation pattern. In this case, the results suggest that it is sufficiently accurate to assume a common DoA for all elements at each comparison point.

The last aspect to consider is the reproducibility of the results. The measurements were repeated multiple times, and the results consistently showed similar phase and amplitude offsets between the two Rx antennas. This reproducibility is crucial for validating the calibration method's reliability and effectiveness in controlled environments.

In summary, the anechoic chamber results confirm the method's accuracy and reproducibility under controlled conditions. The measurements are consistent with theoretical predictions outlined in chapter 2, and the observed limitations are well-understood, primarily relating to edge effects, initialization artifacts, and path distance estimation at higher frequencies.

### 5.2.2 Outdoor Results

The outdoor measurement campaign provided valuable insights into the practical challenges of calibrating MIMO systems in real-world environments. In contrast to the controlled conditions of the anechoic chamber, the outdoor results exhibited greater variability and reduced accuracy in estimating phase and amplitude offsets between antenna elements.

The dominant limitation in the outdoor measurements was the accuracy and reliability of the GNSS-based positioning system. Although RTK corrections were employed, the GNSS data quality was inconsistent, primarily due to limited satellite visibility for the transmitter, as shown in Figure 4.3.7. Environmental obstructions, such as terrain and nearby structures, contributed to this limitation. As a result, errors in distance compensation directly affected the reliability of the extracted calibration offsets. The phase offset between the two Rx antennas often exhibited a periodic or wavelike pattern, rather than the stable offset observed in indoor measurements.

This periodicity is consistent with the transmitter's movement pattern (see Figure 3.4.5) and indicates that the distance correction lacked sufficient precision. This is further evidenced in the uncompensated phase offset plot (Figure B.8), where the compensated phase offset appears as a shifted version of the uncompensated data. Accurate distance correction would have resulted in a more stable phase offset over time. The observed periodicity suggests that while the channel estimation was robust enough to extract the LoS tap, the overall calibration accuracy was primarily limited by positioning errors.

Environmental factors, particularly multipath propagation from ground and surrounding objects, introduced additional components into the channel impulse response. This complicated the isolation of the true LoS tap, especially given the limited time resolution (75 m), which is at the threshold of what the environment permits. Deep fades and constructive interference, especially during system transport and setup (noted at the beginning and end of the dataset), further complicated the extraction of consistent calibration parameters.

Implementation of the APES algorithm for channel estimation proved imprac-

tical for the full dataset. APES provided better isolation of the LoS tap compared to the FFT method. However, the computational cost was prohibitive, with estimated processing times exceeding 100 hours for APES versus approximately 4 hours for FFT. This highlights the need for more efficient algorithms or hardware acceleration for large-scale outdoor datasets. In addition, the algorithm need tuning to achieve optimal performance.

On a positive note, the Rx GNSS positioning system maintained high satellite visibility (over 25 satellites, see Figure 4.3.7) and achieved a calculated positional variance of  $2 \cdot 10^{-4}$  cm after RTK corrections. However, uncertainties remain regarding the precise determination of the Rx array elements positions relative to the GNSS antenna, due to reliance on a magnetic compass for orientation and the unknown location of the precise phase centers of both the GNSS and LPDA antennas.

CFO was also observed in the outdoor measurements, though it appeared less linear than in the indoor case. This may be attributed to temperature-induced drift in the USRP oscillators, particularly during initial warm-up periods, but the drift stabilized after several minutes of operation. While CFO can be estimated and compensated for in post-processing, this was not performed in the outdoor measurements to maintain consistency with the anechoic chamber results.

Despite these challenges, the outdoor experiments demonstrated that the calibration methodology is feasible, provided that high-quality GNSS data is available and the measurement environment is carefully selected to minimize multipath effects. The use of RTK corrections improved positioning accuracy, but further enhancements, such as integrating inertial measurement units (IMUs), employing survey-grade equipment, or using alternative positioning technologies, are recommended for robust performance in more demanding scenarios.

In summary, the outdoor results underscore the critical importance of precise positioning, careful site selection, and robust data processing for successful in-situ calibration. While the method is applicable in outdoor environments, its accuracy and repeatability are strongly dependent on environmental conditions and the quality of supporting sensor data.

### 5.3 Comparison with Theory and Previous Work

The experimental results presented in this thesis are largely consistent with the theoretical framework described in Chapter 2, and they extend the understanding of practical calibration challenges in MIMO systems.

In the anechoic chamber, the measured phase and amplitude offsets between antenna elements were stable and reproducible, as predicted by the theoretical model of a linear time-invariant LTI channel dominated by a LoS component. Systematic errors observed at higher frequencies, particularly at 6 GHz, corroborate theoretical predictions that calibration accuracy becomes increasingly sensitive to positioning errors as the wavelength decreases. This finding is in line with previous studies, such as [1], which emphasize the importance of precise positioning for high-frequency calibration.

Hardware imperfections, including CFO and initialization artifacts, were evident in the measurements. The calibration method demonstrated robustness to

common-mode CFO, owing to the shared local oscillator in the receiver, which supports the theoretical assumption that relative phase offsets can be reliably estimated even in the presence of such imperfections. However, in scenarios involving multiple independent oscillators, CFO and related effects must be explicitly addressed to ensure calibration accuracy.

The outdoor measurements underscore the practical limitations imposed by GNSS-based positioning. Despite the use of RTK corrections, the results reveal that satellite visibility, multipath propagation, and environmental obstructions remain significant sources of error, directly impacting the reliability of distance compensation and, consequently, calibration accuracy. These observations are consistent with the challenges reported in [11, 12], and highlight the need for more robust and integrated positioning solutions in real-world deployments.

Overall, the experimental findings validate the theoretical models under controlled conditions and provide critical insights into the limitations encountered in practical, in-situ calibration scenarios. The results highlight the necessity of precise positioning, robust synchronization, and advanced data processing to achieve reliable MIMO calibration in diverse environments.

## 5.4 Analysis by Scenario

The results from the calibration experiments are analyzed separately for the anechoic chamber and outdoor environments to highlight both the strengths and challenges of the proposed methodology.

In the anechoic chamber, the controlled environment enabled highly reproducible and accurate estimation of phase and amplitude offsets between antenna elements. The absence of multipath and external interference allowed for precise distance compensation and validation of the theoretical calibration model. Systematic errors were mainly observed at higher frequencies, where the shorter wavelength increased sensitivity to small positioning inaccuracies.

In contrast, the outdoor scenario introduced significant variability due to environmental factors such as multipath propagation, variable satellite visibility, and temperature fluctuations. GNSS-based positioning, even with RTK corrections, was less reliable for the transmitter, leading to errors in distance compensation and less stable calibration offsets. Multipath effects and ground reflections further complicated the extraction of the true LoS component.

The main differences between the two scenarios can be attributed to environmental complexity, measurement uncertainties, and hardware limitations. While the anechoic chamber results serve as a benchmark for optimal performance, the outdoor results underscore the importance of robust positioning and environmental awareness in practical deployments.

## 5.5 Limitations and Sources of Error

Several limitations and sources of error were identified throughout the study:

- **GNSS Positioning Accuracy:** The primary limitation in outdoor measurements was the accuracy of the GNSS-based positioning system, particularly for the transmitter. Limited satellite visibility and multipath effects led

to inconsistent position estimates, directly impacting distance compensation and calibration accuracy.

- **Hardware Synchronization:** Carrier frequency offset from the SDRs introduced phase drifts and is especially significant in scenarios without shared oscillators. While the method was robust to common-mode CFO in the receiver, independent oscillators or temperature-induced drifts could degrade performance.
- **Environmental Factors:** Multipath propagation, ground reflections, and environmental obstructions in the outdoor scenario complicated the isolation of the LoS component and introduced additional uncertainty in the measurements.
- **Measurement Uncertainties:** The precise positions of the Rx array elements relative to the GNSS antenna were not known with high accuracy, and the use of a compass for orientation introduced further uncertainty.
- **Computational Constraints:** The APES algorithm, while providing higher resolution, was computationally intensive and impractical for large datasets, limiting its use in real-time or high-throughput scenarios.

These limitations highlight the need for careful system design, robust data processing, and, where possible, the integration of additional sensors or correction mechanisms.

## 5.6 Recommendations and Future Work

Based on the identified limitations and observed results, the following prioritized recommendations and directions for future work are proposed. Each recommendation is discussed with explicit reference to how it addresses and reduces the key tradeoffs outlined in the theory chapter, such as accuracy vs. flexibility, real-time vs. post-processing, and environmental robustness vs. system complexity.

### 5.6.1 1. Positioning Accuracy and Validation

- **Enhanced Positioning Systems:** Integrate additional sensors such as inertial measurement units (IMUs), LIDAR, or total station surveying to improve positioning accuracy and robustness, particularly in environments with limited satellite visibility or significant multipath effects. By fusing GNSS with other sensors, the system can maintain centimeter-level accuracy even in challenging conditions, directly reducing the tradeoff between flexibility (field deployment) and accuracy (phase calibration). Real-time validation mechanisms will further ensure that only high-quality position data is used, minimizing the risk of calibration errors due to positioning uncertainty.

### 5.6.2 2. Drone Payload and System Miniaturization

- **Drone-Based Calibration Frameworks:** Develop a UAV-compatible, lightweight, and power-efficient payload specifically designed for antenna array calibration. This includes miniaturizing the calibration hardware, optimizing the integration of SDRs, GNSS receivers, and supporting electronics, and ensuring electromagnetic compatibility to minimize interference with measurement signals. Emphasis should be placed on reducing payload weight and power consumption to maximize flight time and operational range, thereby enabling flexible and repeatable calibration in a wider variety of environments. Such advancements will directly address the tradeoff between operational flexibility (e.g., UAV or portable use) and the accuracy and complexity of the calibration system, making high-precision calibration feasible in more diverse and dynamic scenarios. A drone-based framework would also allow for integration of the drone's internal positioning system, which could provide additional accuracy and robustness to the overall calibration process.
- **Optimized Power Supply Solutions:** Given that battery weight was a significant limitation during outdoor measurements, future work should focus on developing a lightweight, high-efficiency power supply tailored for UAV applications. This includes designing custom DC power electronics to directly power the USRP and ancillary devices, minimizing conversion losses and overall system weight.

### 5.6.3 3. Real-Time Processing, Speed and Automation

- **Real-Time Processing Improvements:** Port signal processing algorithms to compiled languages (e.g., C/C++) or leverage FPGA-based acceleration to enable higher bandwidths and reduce processing times for real-time applications. This will reduce the need to compromise between bandwidth (and thus resolution) and processing speed, as discussed in the theory chapter. Efficient real-time processing allows for immediate feedback and rapid adjustments during field measurements, narrowing the gap between real-time and post-processing tradeoffs, facilitating faster iterations and more responsive calibration workflows. Additionally, processing data in real time significantly reduces memory requirements, as large raw datasets do not need to be stored for later analysis.
- **Automation and System Integration:** Automate manual processes such as data synchronization, equipment control, and calibration routines to improve repeatability, reduce human error, and enable fully autonomous measurement campaigns. Automation reduces system complexity for the user and increases the reliability of results, addressing the tradeoff between system complexity and operational robustness.

### 5.6.4 4. Antenna Characterization

- **Accurate Antenna Measurements:** Perform comprehensive characterization of the antenna elements, including detailed radiation pattern mea-

surements and precise determination of phase centers. Accurate knowledge of the phase center is essential for precise distance compensation, while verified antenna patterns are necessary to validate the measured responses and ensure correct interpretation of calibration results. These measurements should be performed prior to calibration to minimize uncertainty and improve overall accuracy, especially when the direction of arrival varies across the array. Improved antenna models will reduce the uncertainty in calibration, thus minimizing the tradeoff between calibration accuracy and the practical constraints of field measurements.

### 5.6.5 5. Advanced Data Processing and Validation

- **Interpolation Techniques:** Future work should also investigate advanced interpolation methods to maximize the extraction of useful information from the measurements. Improved interpolation can enhance the resolution and accuracy of the calibration results, particularly when measurement points are sparse or irregularly spaced, such as in the case of SDR and GNSS data, or when comparing antenna patterns as a function of DoA. Techniques such as spline interpolation, kriging, or machine learning-based approaches could be explored to better reconstruct the underlying calibration parameters from limited data.
- **Expanded Validation and Generalization:** Conduct additional experiments with different antenna types, array configurations, and in a wider range of environments to validate the methodology's robustness and generalizability. Comparative studies with alternative calibration techniques will help identify the optimal balance between accuracy, flexibility, and complexity.

These recommendations provide a clear roadmap for future work, with each proposed solution specifically targeting the reduction of the fundamental tradeoffs discussed in the theory. By addressing these tradeoffs, the methodology can be advanced toward more reliable, efficient, and scalable calibration solutions for next-generation wireless systems.

## 5.7 Summary

This chapter has provided a critical analysis of the experimental results, highlighting the differences between controlled and real-world measurement scenarios, identifying key limitations and sources of error, and discussing the practical implications for MAMIMO calibration. The findings confirm the feasibility of the proposed methodology in controlled environments and outline the challenges that must be addressed for robust outdoor deployment. Recommendations for future work focus on improving positioning accuracy, processing efficiency, and system automation, supporting the continued advancement of flexible and high-precision calibration strategies for next-generation wireless communication systems.

---

CHAPTER  
**SIX**

---

## CONCLUSIONS

This thesis has demonstrated the feasibility of a flexible, in-situ calibration methodology for MAMIMO antenna arrays, validated through both controlled anechoic chamber experiments and real-world outdoor measurements. The approach integrates SDR-based transmitter and receiver, high-precision GNSS positioning with RTK corrections, and advanced signal processing algorithms to estimate and compensate for phase and amplitude offsets between antenna elements.

In the anechoic chamber, the methodology achieved high accuracy and reproducibility, with stable phase and amplitude offsets extracted across multiple frequencies. The controlled environment enabled precise synchronization and reliable distance compensation, confirming the validity of the theoretical models and calibration workflow. These results establish a robust baseline for calibration performance under ideal conditions.

Outdoor experiments highlighted the challenges associated with GNSS-based positioning, multipath propagation, and environmental variability. While the calibration method remained applicable, increased uncertainty and variability were observed, primarily due to limitations in GNSS accuracy and satellite visibility. The application of RTK corrections improved positioning precision, but residual errors in distance estimation limited the achievable calibration accuracy in some scenarios. Nevertheless, the results confirm that the methodology can be extended to field environments, provided that high-quality GNSS data and careful site selection are ensured.

The study also compared real-time and post-processing approaches, revealing a trade-off between measurement duration, bandwidth, and computational complexity. Real-time processing supports longer measurement campaigns with reduced memory requirements, while post-processing enables higher resolution and more advanced algorithms at the cost of increased computational resources.

Overall, this work provides a robust and adaptable framework for the calibration of MAMIMO systems, bridging the gap between theoretical models and practical deployment. The findings lay the groundwork for further advancements in automated, high-precision calibration techniques, supporting the reliable operation of next-generation wireless communication systems in both laboratory and real-world settings.



## REFERENCES

- [1] Georg L. Berg. *Drone based calibration of MAMIMO antenna array, Spesialization Project, NTNU*. [https://github.com/GeorgNtnu/Spesialization\\_Project.git](https://github.com/GeorgNtnu/Spesialization_Project.git). 2024.
- [2] Bernard Sklar and Fred Harris. *Digital Communications, Fundamentals and Applications*. Pearson, 2021.
- [3] Jeffery S. Beasley, Jonathan D. Hymer, and Gary M. Miller. *Electronic Communications, a system approach*. Pearson, 2014.
- [4] David M. Pozar. *Microwave Engineering, Theory and Techniques*. Wiley, 2012.
- [5] Golsa Ghiaasi et al. “Measured Channel Hardening in an Indoor Multiband Scenario”. In: *2018 IEEE 29th Annual International Symposium on Personal, Indoor and Mobile Radio Communications (PIMRC)*. 2018, pp. 1–6. DOI: [10.1109/PIMRC.2018.8581026](https://doi.org/10.1109/PIMRC.2018.8581026).
- [6] Egil Eide. “Design of LPDA antenna, Technical note, NTNU”. (unpublished) 2016.
- [7] Abdelhakim Khlifi and Ridha Bouallegue. “Performance Analysis of LS and LMMSE Channel Estimation Techniques for LTE Downlink Systems”. In: *International Journal of Wireless & Mobile Networks (IJWMN)* 3.5 (2011). Accessed: 2025-01-07, pp. 141–148. DOI: [10.5121/ijwmn.2011.3511](https://doi.org/10.5121/ijwmn.2011.3511). URL: <https://arxiv.org/pdf/1111.1666.pdf>.
- [8] P. Stoica and R.L. Moses. *Spectral Analysis of Signals*. Pearson Prentice Hall, 2005. ISBN: 9780131139565. URL: <https://books.google.no/books?id=h78ZAQAAIAAJ>.
- [9] George-Othon Glentis. “A Fast Algorithm for APES and Capon Spectral Estimation”. In: *IEEE Transactions on Signal Processing* 56.9 (2008), pp. 4207–4220. DOI: [10.1109/TSP.2008.925940](https://doi.org/10.1109/TSP.2008.925940).
- [10] T. Ekman. *Forward-and-Backward APES Algorithm: MATLAB implementation*. Unpublished MATLAB code. 1999.
- [11] Børje Forssell, Norvald Kjerstad, and Lars Mæhlum. *GNSS*. Store norske leksikon. 2024. URL: <https://snl.no/GNSS>.
- [12] Lars Mæhlum. *RTK*. Store norske leksikon. 2024. URL: <https://snl.no/RTK>.

- [13] Travis F. Collins et al. *Software-Defined Radio for Engineers*. Artech House, 2018. ISBN: 978-1-63081-457-0. URL: <https://www.analog.com/en/resources/technical-books/software-defined-radio-for-engineers.html>.
- [14] Ettus Research. *Ettus Research - The leader in Software Defined Radio (SDR)*. Accessed: 2025-01-20. 2025. URL: <https://www.ettus.com/>.
- [15] Ettus Research. *USRP B200/B210 Specification Sheet*. Accessed: 16-May-2025. 2019. URL: [https://www.ettus.com/wp-content/uploads/2019/01/b200-b210\\_spec\\_sheet.pdf](https://www.ettus.com/wp-content/uploads/2019/01/b200-b210_spec_sheet.pdf).
- [16] P.H. Moose. “A technique for orthogonal frequency division multiplexing frequency offset correction”. In: *IEEE Transactions on Communications* 42.10 (1994), pp. 2908–2914. DOI: [10.1109/26.328961](https://doi.org/10.1109/26.328961).
- [17] Jeffrey G. Andrews. “A Primer on Zadoff Chu Sequences”. In: *arXiv cs.IT.2211.05702v2* (June 2023). Available at: [<https://arxiv.org/pdf/2211.05702.pdf>] (<https://arxiv.org/pdf/2211.05702.pdf>).
- [18] Cosme Culotta-López et al. “On the Uncertainty Sources of Drone-Based Outdoor Far-Field Antenna Measurements”. In: *2021 Antenna Measurement Techniques Association Symposium (AMTA)*. 2021, pp. 1–6. DOI: [10.23919/AMTA52830.2021.9620638](https://doi.org/10.23919/AMTA52830.2021.9620638).
- [19] Kentaro Saito and Sora Kojima. “4.8 GHz Band Radio Channel Measurement by Unmanned Aerial Vehicle-Based Virtual Array Channel Sounding System”. In: *2025 19th European Conference on Antennas and Propagation (EuCAP)*. 2025, pp. 1–5. DOI: [10.23919/EuCAP63536.2025.10999350](https://doi.org/10.23919/EuCAP63536.2025.10999350).
- [20] MathWorks. *latlon2local - Convert geographic coordinates to local Cartesian coordinates*. 2025. URL: <https://se.mathworks.com/help/driving/ref/latlon2local.html>.
- [21] Georg L. Berg. *Master Thesis Repository*. Contains files and scripts related to the author’s master thesis. 2025. URL: <https://github.com/GeorgNtnu/Master-Thesis/tree/main>.
- [22] rtklibexplorer. *RTKLIB: demo5 b34k*. Accessed: 26-April-2025. 2024. URL: <https://github.com/rtklibexplorer/RTKLIB/releases>.

## APPENDICES

### A GitHub repository

This section provides links to the GitHub repositories containing the source code and software used throughout the project. The repositories include all developed code for both indoor and outdoor measurements, as well as the RTKLIB software for GNSS data processing.

- **Project source code (indoor and outdoor measurements):** <https://github.com/GeorgNtnu/MasterProject>
- **RTKLIB software for GNSS data processing:** <https://github.com/rtklibexplorer/RTKLIB/releases>

### B Extra results

This section presents additional figures and tables that supplement the main results discussed in the thesis. These extra results provide further insight into the measurement campaigns, signal processing steps, and system performance. Figures include uncompensated measurement data, offset analyses, and supplementary plots for both anechoic chamber and outdoor scenarios. Additional tables or data summaries may also be included here for completeness.

#### B1 Anechoic chamber extra results

The raw uncompensated measurement results from the anechoic chamber measurements are shown in Figure B.1, Figure B.3 and Figure B.5. The results are not corrected for path distance between the Tx and the Rx antenna array. The phase and amplitude offset between the two antennas in the Rx array for the anechoic chamber measurements are shown in Figure B.2, Figure B.4 and Figure B.6.

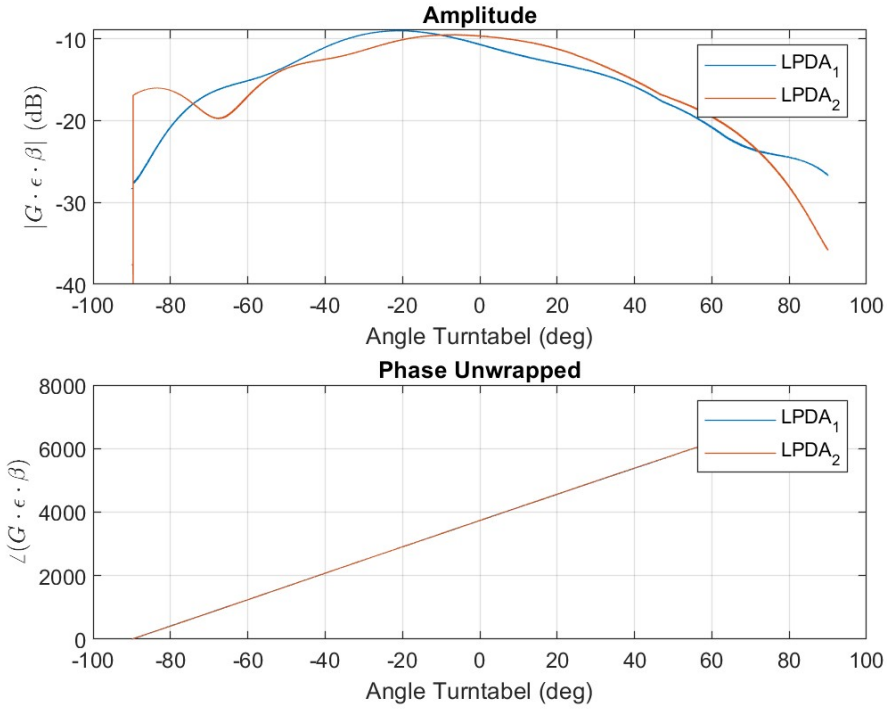


**Figure B.1:** The phase and amplitude of the LoS tap for the anechoic chamber measurements at 1.3GHz. The measurements are not corrected for path distance between the Tx and the Rx antenna array.

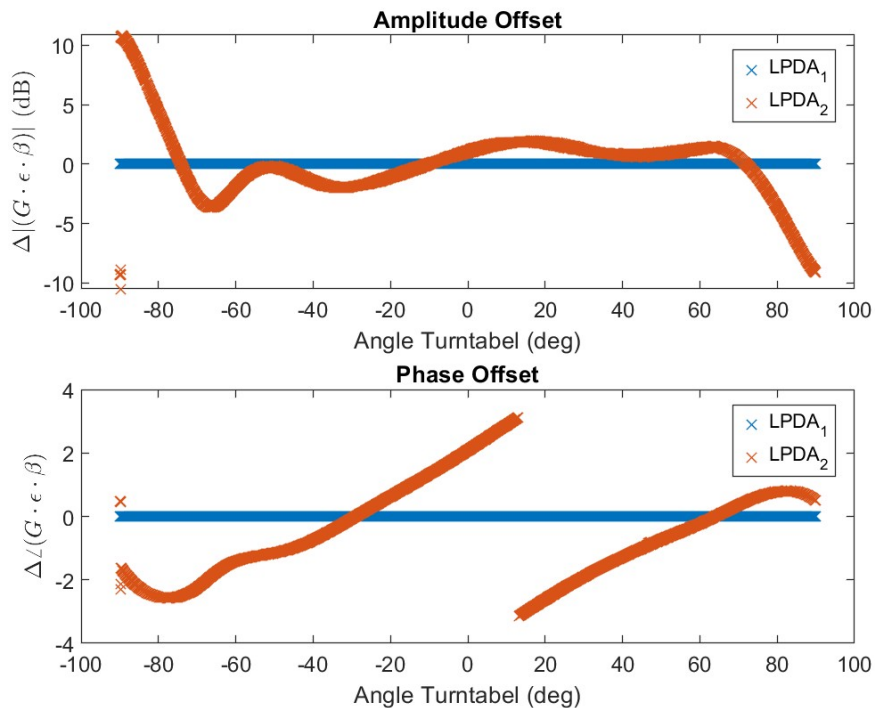


**Figure B.2:** The phase and amplitude offset between the two antennas in the Rx array for the anechoic chamber measurements at 1.3GHz.

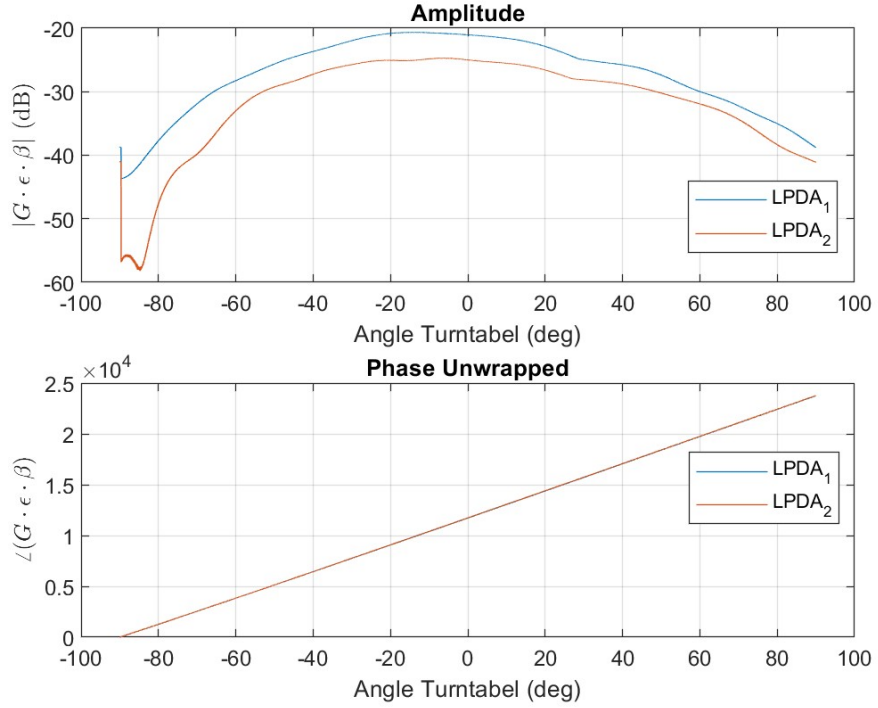


**Figure B.3:** The phase and amplitude of the LoS tap for the anechoic chamber measurements at 3GHz. The measurements are not corrected for path distance between the Tx and the Rx antenna array.

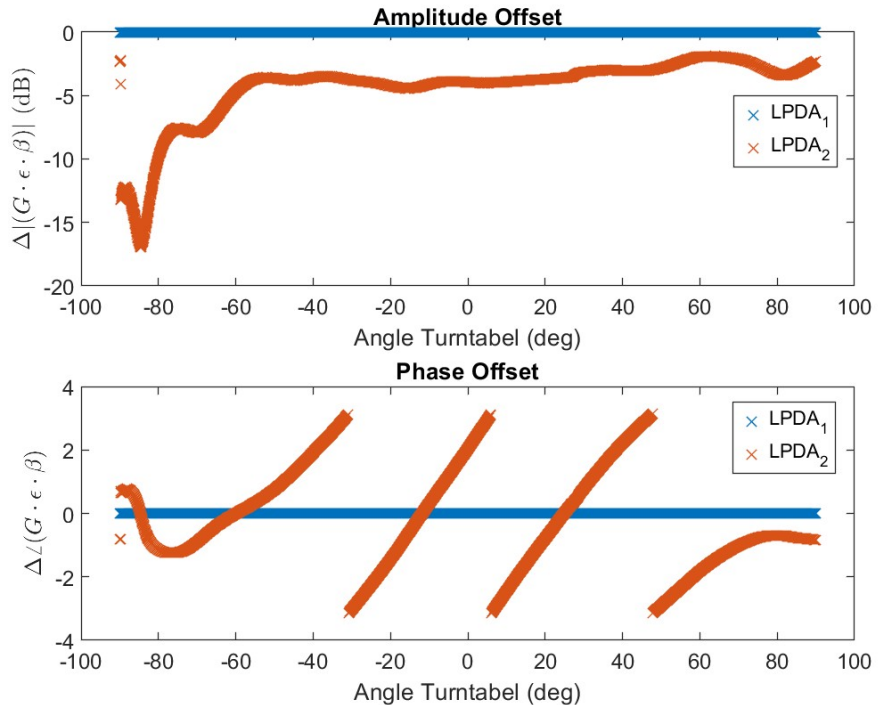


**Figure B.4:** The phase and amplitude offset between the two antennas in the Rx array for the anechoic chamber measurements at 3GHz.

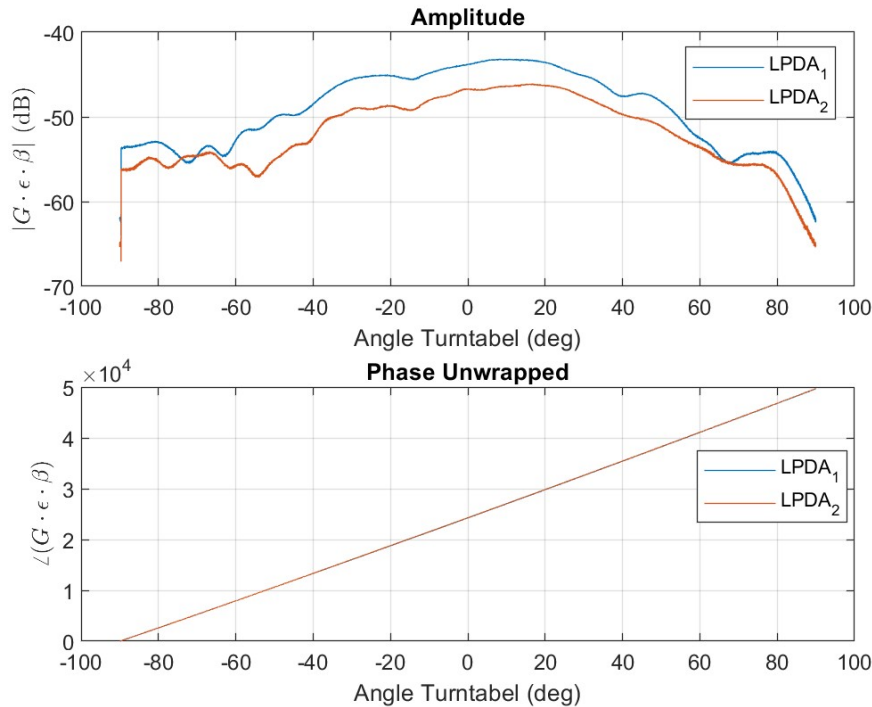


**Figure B.5:** The phase and amplitude of the LoS tap for the anechoic chamber measurements at 6GHz. The measurements are not corrected for path distance between the Tx and the Rx antenna array.

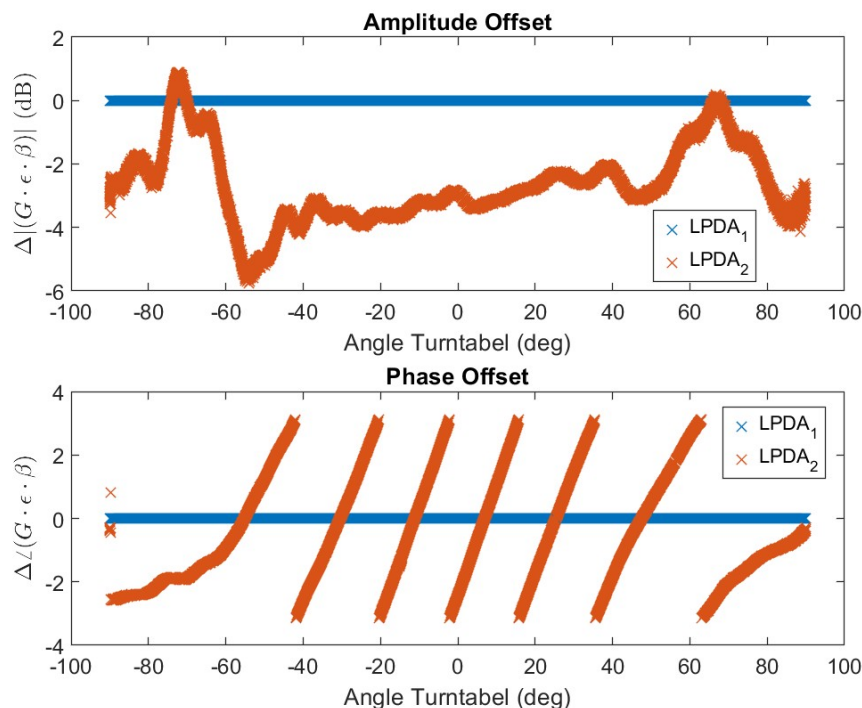


**Figure B.6:** The phase and amplitude offset between the two antennas in the Rx array for the anechoic chamber measurements at 6GHz.

## B2 Outdoor extra results

The raw uncompensated measurements of the outdoor measurements are shown in

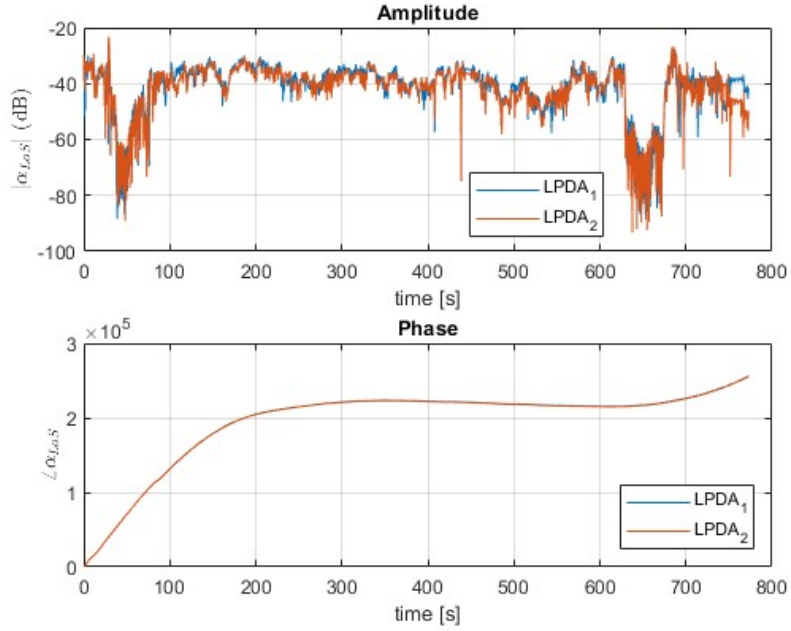


**Figure B.7:** The phase and amplitude of the LoS tap for the outdoor measurements at 1.3 GHz. The measurements are not corrected for path distance between the Tx and the Rx antenna array.

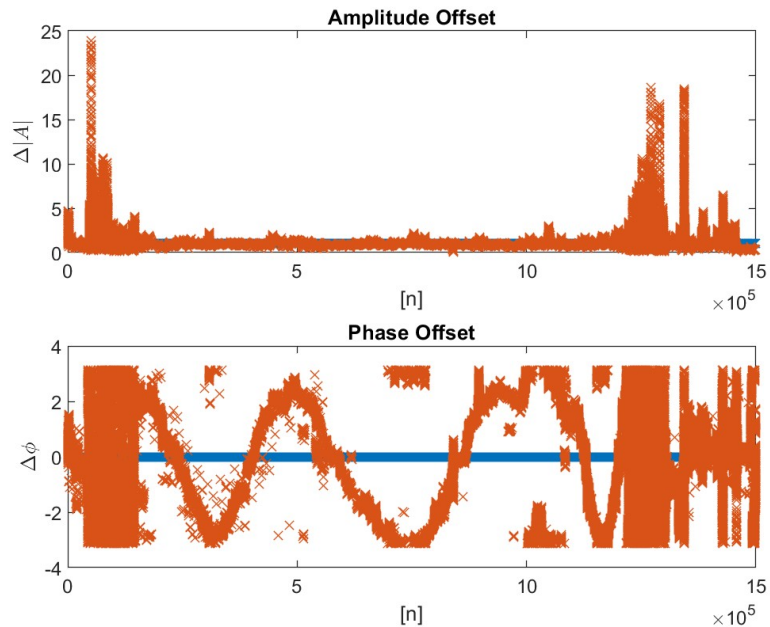


**Figure B.8:** The phase and amplitude offset between the two antennas in the Rx array for the outdoor measurements shown in Figure B.7.

## C SDR configuration

In matlab the SDRs are configured using the `comm.SDRuReceiver` and `comm.SDRuTransmitter` objects. The exact settings depend on the desired goal. By this is meant whether the data is processed in realtime or not allowing greater bandwidth, but using more memory. On the Tx side this is not a problem as it is not a bottleneck.

### C1 Indoor SDR configuration

The SDR configuration for the indoor measurements performed using two MATLAB scripts. For the Tx, it's named `TxQPSK.m` and for the Rx, it's named `RxQPSK.m`.

Parameter	Value
Platform	B210
Serial Number	30998E2
Center Frequency ( $f_c$ )	6 GHz
Baseband Sample Rate ( $f_s$ )	1 MHz
Master Clock Rate	30 MHz
Gain	40
Channel Mapping	1
Interpolation Factor	30
Modulation	QPSK (Gray-coded)
Preamble	Zadoff-Chu (length 50, repeated)
Output Data Type	double

**Table C.1:** SDR Transmitter (Tx) Configuration

The receiver uses a virtual buffer to prevent packet loss. This buffer temporarily holds the last samples from the current frame and the first samples from the next frame. By combining these samples, the receiver can process them together as a single packet, ensuring that no data is lost between frames.

Parameter	Value
Platform	B210
Serial Number	30998D7
Center Frequency ( $f_c$ )	6 GHz
Baseband Sample Rate ( $f_s$ )	1 MHz
Master Clock Rate	30 MHz
Gain	[40, 40]
Channel Mapping	[1, 2]
Decimation Factor	30
Output Data Type	double
Samples Per Frame	$2 \times (1000 + 50) = 2100$
Preamble	Zadoff-Chu (length 50, repeated)

**Table C.2:** SDR Receiver (Rx) Configuration

## C2 Outdoor SDR configuration

The SDR configuration for the outdoor measurements is performed using the GNU Radio Companion (GRC) software for the Tx and MATLAB for the Rx. The Tx GNU Radio flowgraph is named `GRC_Flowgraph.grc`. The Rx MATLAB script is named `Rx_RealTime.m`.

Parameter	Value
Platform	B210
Serial Number	30998E2
Center Frequency ( $f_c$ )	1.3 GHz
Sampling Rate ( $f_s$ )	4 MHz
Master Clock Rate	20 MHz
Gain	[40, 40]
Channel Mapping	[1, 2]
Decimation Factor	5
Output Data Type	single
Samples Per Frame	$2^{12} = 4096$

**Table C.3:** SDR Configuration Parameters for USRP B210

## D GNSS configuration

The GNSS configuration for both the Rx and Tx devices is performed using the u-blox u-center software. The settings are saved in the text file `GNSS_Configuration.txt`. For the Rx GNSS receiver, the dynamic model is set to "Stationary" as the Rx array is static. For the Tx GNSS receiver, the dynamic model is set to "Airborne < 4g" to accommodate potential drone mounting. The configuration is loaded into the u-blox ZED-F9P via USB.

### D1 Rx Positioning

The Rx GNSS receiver is connected to a PC via USB, which serves as the host computer. Since the Rx is static, its position only needs to be measured once. The GNSS Rx antenna is placed at a fixed position relative to the Rx array, enabling the calculation of each array element's position. Configuration details for the u-blox ZED-F9P are available in [21].

### D2 Tx Positioning

The Tx GNSS receiver is connected to an RPi 4B, which acts as the host computer. The ZED-F9P is preconfigured on a Windows computer using the u-center software and then connected to the RPi via USB. The RPi runs four main scripts to manage data collection and processing: `log_master.sh`, `ublox.sh`, `ublox_copyer.py`, and `ublox_parser.py`.

- `log_master.sh`: Manages the overall logging process, creates a unique directory for each flight, runs `ublox.sh`, and ensures proper shutdown of processes.
- `ublox.sh`: Configures the u-blox device, sets the baud rate, and runs

`ublox_copyer.py` to collect GNSS data. - `ublox_copyer.py`: Reads data from the u-blox device, synchronizes on specific sync bytes, and writes the data, along with timestamps, to a file. - `ublox_parser.py`: Parses the collected binary GNSS data to extract relevant information such as latitude, longitude, height, satellite count, time of week, and quality.

The workflow begins with running `log_master.sh` on the RPi to initiate the logging process. This script creates a flight directory and starts `ublox.sh`, which configures the u-blox device and collects data using `ublox_copyer.py`. After data collection, `ublox_parser.py` processes the binary data to extract GNSS information. All scripts and configuration files are provided by the UAV lab at NTNU and are available in [21].

### D3 RTK correction

RTK correction is performed using the open-source RTKLIB software, which is available on GitHub [22]. The GNSS data collected by the u-blox ZED-F9P receiver (.ubx files) is processed in three main steps to enhance positioning accuracy:

The raw .ubx files are first converted into observation (.obs) and navigation (.nav) files using the RTKCONV tool. These files contain the necessary satellite and receiver data for further processing. Next, the RTKPOST tool processes the observation and navigation files, applying corrections using basestation data to refine the rover's position by leveraging real-time kinematic (RTK) techniques. Finally, the corrected position data is saved in standard formats, enabling integration into matlab for subsequent synchronization with measurements.

This process ensures high-precision GNSS positioning by utilizing RTK corrections, making it suitable for applications requiring centimeter-level accuracy.

## E Turntable configuration

The turntable in the anechoic chamber is controlled using a custom-built MATLAB script that communicates with the Newport XPS-D motion controller over a local area network (LAN). The turntable's IP address is configured as 192.168.42.2, with a subnet mask of 255.255.255.0. The MATLAB script utilizes the XPSD.NET class, which provides methods for initializing, configuring, and controlling the turntable.

Before running the script, the computer is connected to the LAN where the XPS-D controller is accessible.

The script begins by establishing a connection to the XPS-D controller and homing the turntable to ensure it starts from a known reference position. This is achieved using the `GroupInitHome` method. The turntable's speed and movement are then configured to perform precise rotations.

**Listing 1:** Turntable Initialization and Control

```
% Initialize connection to the XPS-D controller
xps = XPSD_NET('192.168.42.2'); % Connect to the controller
Group = 'Group1'; % Define the axis group
xps.GroupInitHome(Group); % Home the turntable to a reference position

% Configure and move the turntable
StartPos = -90; % Starting position in degrees
StopPos = 90; % Stopping position in degrees
Speed = 80; % Speed in degrees per second

xps.SetSpeed(Group, Speed); % Set the rotation speed
xps.MoveAbsolute(Group, StartPos); % Move to the starting position
pause(1); % Wait for the turntable to stabilize
xps.MoveAbsolute(Group, StopPos); % Move to the stopping position
```

To use the MATLAB script, ensure that the XPSD.NET class and the `Newport.XPS.CommandInterface.dll` file are located in the same directory as the script. For a detailed example and additional functionality, refer to the `MainMatlabScriptForTestingTurnTable.m` script in [21].

## F SDR System Design

The following sections describe the implementation of the important components of the SDR system on the Tx and Rx side.

### F1 SDR Tx

The SDR Tx system is built for the USRP B210, which is a dual-channel SDR platform.

#### F1.1 Tx matlab

In MATLAB, the SDR is programmed to transmit a pseudo-random QPSK signal with a preamble. The preamble is generated using the `zadoffChuSeq(25,139)` function, which generates a Zadoff-Chu sequence with a length of 139 and a root index of 25. This sequence is repeated twice resulting in a preamble of length 278. This was done originally for carrier frequency offset estimation and correction

(CFO), but was not used in the end as the CFO was too small to significantly affect the performance and increase performance.

The QPSK signal is generated using the `pskmod(Symb, 4, pi/4, "gray", InputType="integer")`; function, which modulates the symbols using QPSK modulation with a  $\pi/4$  phase offset. The `InputType="integer"` option specifies that the input symbols are integers (integers from 0 to 3). 1000 symbols are generated, and is appended to preamble. Resulting in a total of 1278 symbols. The waveform is then saved to a file for use by the Rx system (`WaveForm.mat`). The Tx transmitter runs a while loop that transmits the waveform on repeat continuously. At a rate similar to the Rx sampling rate. The Tx matlab system is built for the PC as host computer.

## F1.2 Tx GNU Radio

In GNU Radio, the Tx system is built using a flowgraph that imports the waveform from the file `WaveForm.bin` which is the `WaveForm.mat` file converted to a binary file by the matlab script `mat_to_bin.mat`. The flowgraph is built using the `File Source` block to read the binary file, followed by a `USRP Sink` block to transmit the signal with rate matching the Rx sampling rate. The Tx GNU Radio system is built for the RPi as host computer.

## F2 SDR Rx

The Rx system is built in matlab. The system uses many of the same lines of code even though the system may do post or real-time processing. The following sections describe the main components of the Rx system, including frame synchronization, carrier frequency offset estimation, channel estimation, and the forward-and-backward APES algorithm. These components are essential for processing the received signal and extracting useful information.

### F2.1 Frame Synchronization

After sampling the data, frame synchronization is performed using the custom function `FrameSync(inputSignal, preamble, packetLength)`. This function identifies the starting indices of packets in the input signal (`inputSignal`) based on a known preamble (`preamble`).

The function computes the cross-correlation between the input signal and the preamble to identify potential packet start points. Significant peaks in the correlation result are detected, representing the likely start of packets. A dynamic threshold, set to 15 times the average correlation value, is applied to filter out noise and retain only meaningful peaks. To ensure accuracy, the detected indices are validated to confirm they are spaced consistently with the expected packet length (`packetLength`). The function returns the indices of valid packet starting points, ensuring robust frame synchronization.

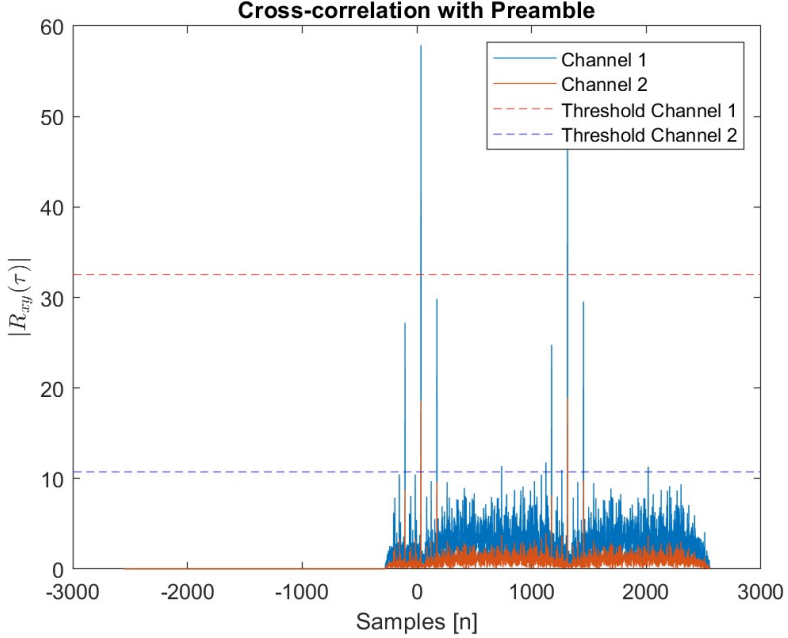


**Figure F.1:** Cross-correlation between the input signal and the preamble from measurements in the anechoic chamber. The figure shows the correlation results for the two antennas, each with its dynamically calculated threshold. The correlation amplitudes differ significantly between the antennas, resulting in distinct thresholds. The detected packet indices exhibit side peaks, which are expected due to the repeated preamble.

**Listing 2:** Frame Synchronization function

```
% Frame Synchronization function
function idx = FrameSync(inputSignal, trainingSequence, N)
    [c, lags] = xcorr(inputSignal, trainingSequence);
    C = abs(c(N:end));
    Delays = lags(N:end);
    Peaks = islocalmax(C, 'MinSeparation', N, 'MinProminence', 0.8*max(C));
    Threshold = mean(C)*15;
    hit = Peaks &(C > Threshold);
    HIT = Delays(hit);
    idx = HIT(HIT > 0);
end
```

## F2.2 CFO Estimation

The MATLAB function `estimateFrequencyOffset` (as shown in Listing 3) estimates the carrier frequency offset present in a received communication signal. This estimation is crucial for optimal synchronization. The algorithm implemented is commonly known as Moose's algorithm, which is a data-aided technique requiring a known training sequence [16].

The function takes two inputs: `trainingSequence`, a complex vector representing the samples of the received known sequence, and `symbolLength`, an integer scalar defining the length of one of the two identical portions that compose the training sequence. The total length of `trainingSequence` is therefore  $2 \times \text{symbolLength}$ . The output, `frequencyOffset`, is the estimated normalized frequency offset.

The core principle of the algorithm is to exploit the repetitive nature of the training sequence. Let the received training sequence be  $R = [r_1, r_2, \dots, r_{2L}]$ , where  $L = \text{symbolLength}$ .

1. **Sequence Division and Conjugation:** The received `trainingSequence` is first divided into two equal halves. The first half, consisting of symbols  $r_1, \dots, r_L$ , is complex conjugated. This forms the `firstPart`:  $P_1 = [r_1^*, r_2^*, \dots, r_L^*]$ . The second half,  $r_{L+1}, \dots, r_{2L}$ , forms the `secondPart`:  $P_2 = [r_{L+1}, r_{L+2}, \dots, r_{2L}]$ . If the transmitted sequence was  $S = [s_1, \dots, s_L]$  repeated twice, and experienced a frequency offset  $\Delta\omega = 2\pi\Delta fT_s$  (where  $T_s$  is the symbol period, often normalized to 1), then  $r_k \approx s_k e^{j(\Delta\omega k + \phi_0)}$  and  $r_{L+k} \approx s_k e^{j(\Delta\omega(L+k) + \phi_0)}$ .
2. **Element-wise Product:** An element-wise product between `firstPart` ( $P_1$ ) and `secondPart` ( $P_2$ ) is computed to create the vector product. Each  $k$ -th element of this vector is:

$$\text{product}_k = P_{1,k} \cdot P_{2,k} = r_k^* \cdot r_{L+k}$$

Substituting the expressions for  $r_k$  and  $r_{L+k}$ :

$$\text{product}_k \approx (s_k^* e^{-j(\Delta\omega k + \phi_0)}) \cdot (s_k e^{j(\Delta\omega(L+k) + \phi_0)}) = |s_k|^2 e^{j\Delta\omega L}$$

This step is crucial as it cancels out the original data symbols (if  $|s_k|^2$  is constant, e.g., for PSK modulation) and the progressive phase term  $\Delta\omega k$ , leaving a phase term  $\Delta\omega L$  that is directly proportional to the frequency offset  $\Delta\omega$  and the known length  $L$ .

3. **Frequency Offset Estimation:** The frequency offset is then estimated from the phase of the sum of the elements in the `product` vector. The sum  $\sum_{k=1}^L \text{product}_k$  averages out noise and reinforces the desired phase term  $\Delta\omega L$ . The phase of this sum is computed using  $\text{atan}(\sum \text{Im}(\text{product}_k) / \sum \text{Re}(\text{product}_k))$ , which effectively calculates  $\arg(\sum \text{product}_k)$ . The final estimated normalized frequency offset  $\widehat{\Delta f T_s}$  is given by:

$$\text{frequencyOffset} = \frac{1}{2\pi L} \text{atan} \left( \frac{\sum_{k=1}^L \text{Im}(\text{product}_k)}{\sum_{k=1}^L \text{Re}(\text{product}_k)} \right)$$

The division by  $L$  normalizes the phase by the duration over which it was observed, and the division by  $2\pi$  converts the phase in radians per  $L$  samples into cycles per sample (normalized frequency).

This method provides a robust estimate of the frequency offset by leveraging the known structure of the training sequence and averaging over its length to mitigate the effects of noise.

### Listing 3: CFO Estimation

```
function frequencyOffset = estimateFrequencyOffset(trainingSequence, symbolLength)
    % Estimate frequency offset using Moose's algorithm
    % Inputs:
    %   trainingSequence - The received training sequence
    %   symbolLength - The length of half the training sequence
    % Output:
```

```

% frequencyOffset - The estimated frequency offset

% Split the training sequence into two parts
firstPart = conj(trainingSequence(1:symbolLength));
secondPart = trainingSequence(symbolLength+1:end);

% Calculate the product of the two parts
product = firstPart .* secondPart;

% Estimate the frequency offset
frequencyOffset = 1 / (2 * pi* symbolLength) * atan(sum(imag(product))/ sum(real(product)));
end

```

### F2.3 Channel Estimation

Channel estimation is performed using two distinct methods: an FFT-based approach and an APES-based approach. Both methods aim to estimate the Line-of-Sight (LoS) component of the channel.

The FFT-based method utilizes the Fast Fourier Transform to estimate the channel response. The received signal segment  $y$  is transformed into the frequency domain using the FFT, and the channel response  $H$  is computed by dividing the received signal spectrum  $Y$  by the reference signal spectrum  $X$ . The time-domain channel response  $h$  is then obtained using the inverse FFT, and the LoS component is extracted as the maximum value of the response.

**Listing 4:** FFT-based Channel Estimation

```

function LoS = SignalProcessingFFT(y, X)
    % FFT-based channel estimation
    % Inputs:
    %   y - Received signal segment
    %   X - Reference signal spectrum
    % Output:
    %   LoS - Estimated Line-of-Sight component

    Y = fft(y);                      % Transform received signal to frequency domain
    H = Y ./ X;                      % Estimate channel response in frequency domain
    h = ifft(H, 1278 * 10);          % Transform back to time domain
    LoS = max(h);                    % Extract the LoS component
end

```

The APES-based method employs the Amplitude and Phase Estimation of Signal (APES) algorithm for high-resolution spectral estimation. The received signal  $y$  is processed using the APES algorithm to compute its spectrum  $Y$ . The channel response  $H$  is then estimated by dividing the spectrum of the received signal by the reference signal spectrum  $X$ . The APES algorithm is applied again to the channel response to obtain the time-domain channel response, and the LoS component is extracted as the maximum value.

**Listing 5:** APES-based Channel Estimation

```

function LoS = SignalProcessingAPES(y, X)
    % APES-based channel estimation
    % Inputs:
    %   y - Received signal segment
    %   X - Reference signal spectrum
    % Output:
    %   LoS - Estimated Line-of-Sight component

    Y = fft(y);                      % High-resolution spectrum of received signal
    H = Y ./ X;                      % Estimate channel response in frequency domain
    h = apes(H, 200, 1278 * 10);     % High-resolution time-domain channel response
    LoS = max(h);                    % Extract the LoS component
end

```

The FFT-based method is computationally efficient and suitable for real-time applications, while the APES-based method provides higher resolution at the cost of increased computational complexity. The choice of method depends on the specific requirements of the application, such as processing speed or accuracy.

#### F2.4 Forward-and-Backward APES Algorithm

The forward-and-backward Amplitude and Phase Estimation of Signal (APES) algorithm is implemented in the function `apes(x, L, Nmax)`. This algorithm computes the complex spectrum of a signal  $x$  using a high-resolution spectral estimation technique. The parameter  $L$  specifies the number of taps for the FIR filter, while  $Nmax$  determines the number of frequency domain samples for the spectrum.

The algorithm begins by constructing forward and backward covariance matrices using Hankel matrices derived from the input signal. These matrices are then decomposed using the Cholesky factorization to ensure numerical stability. Iteratively, the algorithm computes spectral components by combining forward and backward covariance estimates, leveraging their complementary information. The final spectrum is normalized to provide a robust and high-resolution spectral estimate.

This method is particularly effective in scenarios requiring precise spectral estimation, especially in the presence of noise or closely spaced frequency components, where traditional Fourier-based methods may fall short, but are computationally expensive.

**Listing 6:** Forward-and-Backward APES Algorithm

```
% Function to compute the complex spectrum of x using the
% forward-and-backward APES algorithm.
function ape = apes(x, L, Nmax)
% Function to compute the complex spectrum of x using the
% forward-and-backward APES algorithm.
%
% ape = apes(x, L, Nmax);
%
% x Observed 1D complex (demodulated) data;
% L the number of taps of the FIR
% filter exploited by APES;
% Nmax Number of samples of the
% complex spectrum evaluated in the frequency
% domain.
%
%
% ape Complex spectrum of x.
%
% Based on the fast implementation due to Liu.
%
% T. Ekman 16/8 1999
%
% L = 1 renders the fourier transform
% L = a quarter of the length of x is usually sensible
%
x=x(:);
N=length(x);
M=N-L+1;
Y = hankel(x(1:L),x(L:N));
%Z = conj( hankel(x(N:-1:M),x(M:-1:1)) );
Z=rot90(Y,2);
R = Y*Y'+Z*Z';           % Unnormalized fb covariance estimate
R=(R+R')/2;
A=chol(R);                % C in art.
Rint12=inv(A);
```

```

Rinty=sparse(Rint12')*Y;                                % D in art.
Rintz=sparse(Rint12')*Z;                                % E in art.
V11=zeros(1,Nmax);
V12=zeros(1,Nmax);
V13=zeros(1,Nmax);
V22=zeros(1,Nmax);
V23=zeros(1,Nmax);
V33=zeros(1,Nmax);

for k=1:L
    x = Rint12(:, k)'; % The B_k matrix.
    Fr=fft(x, Nmax);      % The k:th part of the b matrix.
    V11=V11+real(Fr).^2+imag(Fr).^2;      % Building || b ||^2
%
    x=Rinty(k, :);    % D_k matrix
    Fy=fft(x, Nmax);      % The k:th part of the d matrix.
    V12=V12 + Fr.*Fy;          % Building b^T d
    V22=V22 + real(Fy).^2+imag(Fy).^2;    % Building || d ||^2
%
    x=Rintz(k, :);    % E_k matrix
    Fz=fft(x, Nmax);      % The k:th part of the e matrix.
    V13=V13+Fr.*Fz;          % Building b^T e
    V23=V23+conj(Fy).*Fz;        % Building | d^H e |^2
    V33=V33+real(Fz).^2+imag(Fz).^2;    % Building || e ||^2
end
%
V33=M-V33;
aQg = V12 + ( V13.*conj(V23) ) ./ V33;
gQg = V22 + conj(V23) .* V23 ./ V33;
aQa = V11 + conj(V13) .* V13 ./ V33;
ape = aQg ./ ( (M-gQg).*aQa + conj(aQg).*aQg );
ape=ape(:);
end

```

## G Rx Array Design

The Rx array is designed in the Fusion CAD software. Technical drawing of the array can be found in the GitHub repository (see appendix A).